Novel Ultrasonic Transducers and Array Designs Using Self-Similar Fractal Geometries

Haoyu Fang

Department of Electronic and Electrical Engineering

University of Strathclyde

A thesis submitted for the degree of

Doctor of Philosophy

December 2018

Copyright

Signed:

Date:

Acknowledgements

When I started to write this thesis six month ago, I thought this section should be very easy. However, I was completely wrong as I realised that in the past few years of my PhD and my life in Glasgow, I received help and support from countless people, families, friends, supervisors, colleagues and many strangers. Here I want to say thanks to you all for the generous help.

First thing first, I want to thank my parents and my family for supporting me mentally and financially. Without their support, I will not be able to get this far on my own. Thanks, my dear mom and dad.

Secondly, special thanks to my first supervisor, Prof. Anthony Gachagan, for his guidance and encouragement from my undergraduate to PhD and offering me this valuable experience doing PhD in Centre for Ultrasonic Engineering (CUE). Also, Thanks my second supervisors, Prof. Anthony Mulholland and Dr Richard O'Leary, for their guidance and inspiration throughout the project. I also want to say thanks to all my colleagues in CUE, especially Dr Zhen Qiu, thanks for her help and I am really glad to work with her.

Lastly, a huge thanks to my girlfriend, Juju, for her love and support and all my friends for their accompany in this foreign country.

Abstract

Wider operational bandwidth is an important requirement of an ultrasound transducer across many applications. Naturally occurring resonating systems utilise structures containing a range of length scales to produce a broad operating bandwidth. In this work, a novel concept of designing a piezoelectric composite using a fractal geometry is proposed in order to explore the potential of enhancing the operational performance, particularly in terms of transducer bandwidth and sensitivity.

Piezoelectric composite configurations were designed using four well-known fractal geometries: Sierpinski Gasket, Sierpinski Carpet, Cantor Set and Cantor Tartan. The fractal composite devices were realised as either 1-3 connectivity or 2-2 connectivity configurations and compared with their corresponding equivalent conventional composite counterpart. Finite element modelling was utilised to design and explore the behaviour of these four fractal composite designs. A single element ultrasound transducer with SG fractal geometry and an ultrasound array with CS fractal geometry were fabricated and importantly, their experimental performance correlated well with the FE predictions.

In this study, fractal composites, with a nominal central operating frequency of 1MHz, have been designed and fabricated with improved bandwidth (and in some case, sensitivity also) when compared to equivalent conventional composite devices. Moreover, the

enhanced bandwidth is shown to provide higher resolution imaging performance. Overall, the careful selection of different resonant frequencies within a composite structure has been shown to improve operational performance and it is anticipated that this transducer concept will become more prevalent as 3D piezoelectric fabrication processes mature.

Contents

List of Figures

List of Tables

Abbreviations

AR	Pillar Aspect Ratio
BVD	Butterworth–Van–Dyke Circuit Model
CS	Cantor Set Fractal Geometry
CT	Cantor Tartan Fractal Geometry
FE	Finite Element
FMC	Full Matrix Capture
FFT	Fast Fourier Transform
KW	Kerf Width
LDV	Laser Doppler Vibrometer
MPAR	Maximum Pillar Aspect Ratio
NDT&E	Non-destructive Testing and Evaluation
OCV	Open Circuit Voltage Response
PCB	Printed Circuit Board
PMN-PT	Lead Magnesium Niobate – Lead Titanate Piezocrystal Material
PVDF	Polyvinylidene Fluoride
PW	Pitch Width
PZT	Lead Zirconate Titanate

SBP	Sensitivity-Bandwidth-Product
SC	Sierpinski Carpet Fractal Geometry
SG	Sierpinski Gasket Fractal Geometry
TFM	Total Focusing Method
TVR	Transmitting Voltage Response
VF	Ceramic Volume Fraction

Symbols

D	Electric Displacement	C/m^2
T	Mechanical Stress	N/m^2
S	Mechanical Strain	-
E	Electric Field	$N/C\ or\ V/m$
d	Piezoelectric charge constant	$m/N\ or\ C/N$
e	Piezoelectric stress constant	C/m^2
g	Piezoelectric voltage constant	Vm/N
h	Piezoelectric stiffness constant	V/m
s	Elastic Compliance	m^2/N
c	Elastic Stiffness	N/m^2
ε	Permittivity	F/m
k	Electromechanical Coupling Coefficient	-
ρ	Material Density	kg/m^3
v	Velocity	m/s
f	Frequency	Hz
Z	Acoustic Impedance	$MRayl$
$\mathcal{Z}$	Electrical Impedance	Ω
T_c	Curie Temperature	℃
tk	Material Thickness	m
C	Capacitor	F
L	Inductor	H
R	Resistor	Ω

w_1	Half Pitch Width of 1-3 Composite	m
w_2	Half Ceramic Pillar Width of 1-3 Composite	m
λ	Wavelength	m
FD	Fractal Dimension	-
τ	Scaling Factor of Fractal Geometry	-
Q_{dil}	Surface Dilation Quality Factor	-
V	Voltage	V
Ey	Young's Modulus	N/m^2
B	Bulk Modulus	N/m^2
G	Shear Modulus	N/m^2
P	Polarization Direction	-
N	Fractal Generation Level	-
a_0	Zero-order Asymmetrical Lamb Mode	-
s_0	Zero-order Symmetrical Lamb Mode	-
s_1	First-order Symmetrical Lamb Mode	-
W_t	Applied Stress Energy	W
W_S	Converted Electrical Energy	W

CHAPTER I

INTRODUCTION

1.1. Project Description

1.1.1. Background

In naturally occurring auditory systems, it is common to observe hearing organs comprised of a number of different length scales. Such hearing organs exhibit extended operating bandwidth, examples include insects such as the bushcricket [1], [2], [3]. In common with all resonating systems, the resonance frequency of a piezoceramic resonator depends on its length scale. Therefore, having a high level of geometric complexity with a range of length results in a range of resonance frequencies, and therefore a broadening of the overall operational frequency range. The concept of engineered transducers comprised of multiple length scales has been developed mathematically [4], [5], [6] and these analytical models indicate that by having elements with varying length scales in the piezoelectric transducer design, the device may possess a wider operational bandwidth or a higher sensitivity compared to a conventional device.

In this PhD project, fractal geometries which have the property of self-repeating at different length scales infinitely will be adopted as the structure of a piezoelectric

composite design, such that the piezoelectric phase of the composite comprises elements of varying size scales.

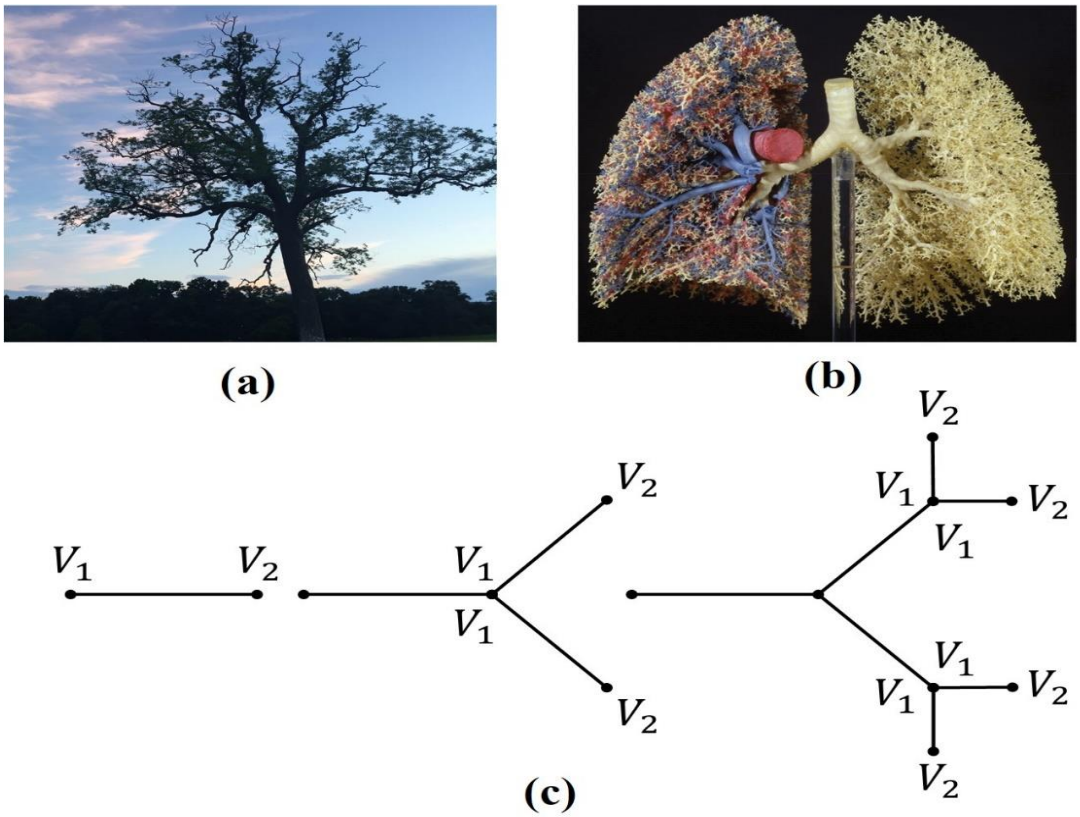

Figure 1-1: Natural fractal example of (a) tree's branching pattern and (b) lung vasculature of human body [7]*; (c) Generation of tree-like fractal geometry using vector-based recursion method*

Fractals can be observed in many naturally occurring structures, the most commonly seen fractal-like shape is a tree's branch pattern, which is structurally optimized to have wider outer surface and hence maximize the amount of sunlight received [8]. Another nice example of a fractal-like pattern in the natural world is the lung vasculature of the human body, which also has the branching fractal-like pattern to provide large surface arear for maximizing the exchange between oxygen, O_2, and carbon dioxide, CO_2 [9]. Figure 1-1

(a) and (b) illustrates these two examples of the fractal-like shapes discovered in the natural world and Figure 1-1 (c) describes the process of generating a tree-like fractal geometry using a vector-based recursion method.

One reason that the self-similar fractal geometry would be a valuable choice compared with a random distributed geometry is that the fractal geometry can be generated by following a simple algebraic rule, which facilitates analyses of the transducer performance within the design space.

In this thesis, the finite element (FE) method will be employed to model and predict the performance of the piezoelectric composite transducer design with different fractal geometries. In the FE modelling process, the studying object is partitioned into a number of elements with finite scale and each element is comprised of a single material. Formulas describing the behaviour of each element are combined into a single system-wide matrix equation, where the behaviour of the whole targeting object can be achieved by solving this matrix equation [10]. The history of the FE modelling for a piezoelectric media can be dated back to 1970s [11] and has been well developed and proven in the past few decades [12].

1.1.2. Motivation

Ultrasound transducers with a wide operational bandwidth would be considered as an advantage in terms of improving system performance, which is preferred in many applications, such as underwater sonar, non-destructive testing (NDT) and biomedical imaging [13] [14] [15] [16].

A broadband transducer can offer better spatial resolution and therefore better imaging performance. In order to demonstrate the relationship between the bandwidth of the transmitting signal and image resolution, the FE modelling approach was employed to simulate the imaging process of two side drilled holes (SDHs) within a stainless steel block using a linear ultrasonic array transducer. The diameter of these two SDHs are both one wavelength and separated by the distance of one wavelength. The schematic of this FE model of a simple NDT configuration is shown in Figure 1-2.

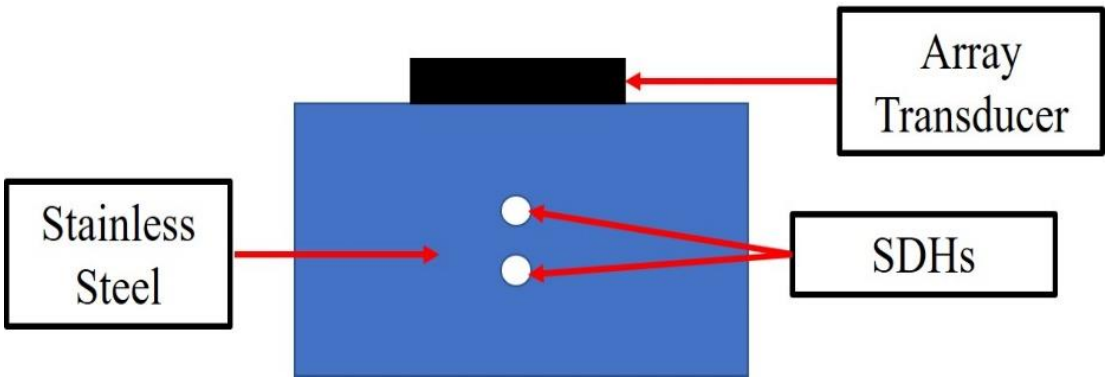

Figure 1-2: Schematic of FE imaging model used to demonstrate system performance with respect to operational bandwidth

In this FE model, a 64-element linear array with central frequency of 2.25 MHz was simulated, in which each element has the ability of transmitting an ultrasound pulse with a different bandwidth characteristic into the steel load medium. In order to keep the total energy contained within the excitation pulse consistent for each bandwidth option, the peak-to-peak voltage, V_{p-p}, is varied. The time domain waveform and frequency spectrum for three examples cases - 17 %, 55 % and 110 % bandwidth signal - are shown in Figure 1-3 (a), (b) and (c), respectively.

The resultant images for these three excitation signal scenarios have been produced using the total focusing method (TFM) and full matrix capture (FMC) array processing and data acquisition approaches [17]. Full details of the FMC and TFM techniques will be introduced in Chapter II of this thesis. The TFM images for the 17%, 55% and 110% bandwidth cases are presented in Figure 1-4. It can be clearly observed that by using the ultrasound pulse with a larger bandwidth, less ringing around the target imaging area can be achieved and clearer definition of the target, i.e. higher resolution, is also obtained.

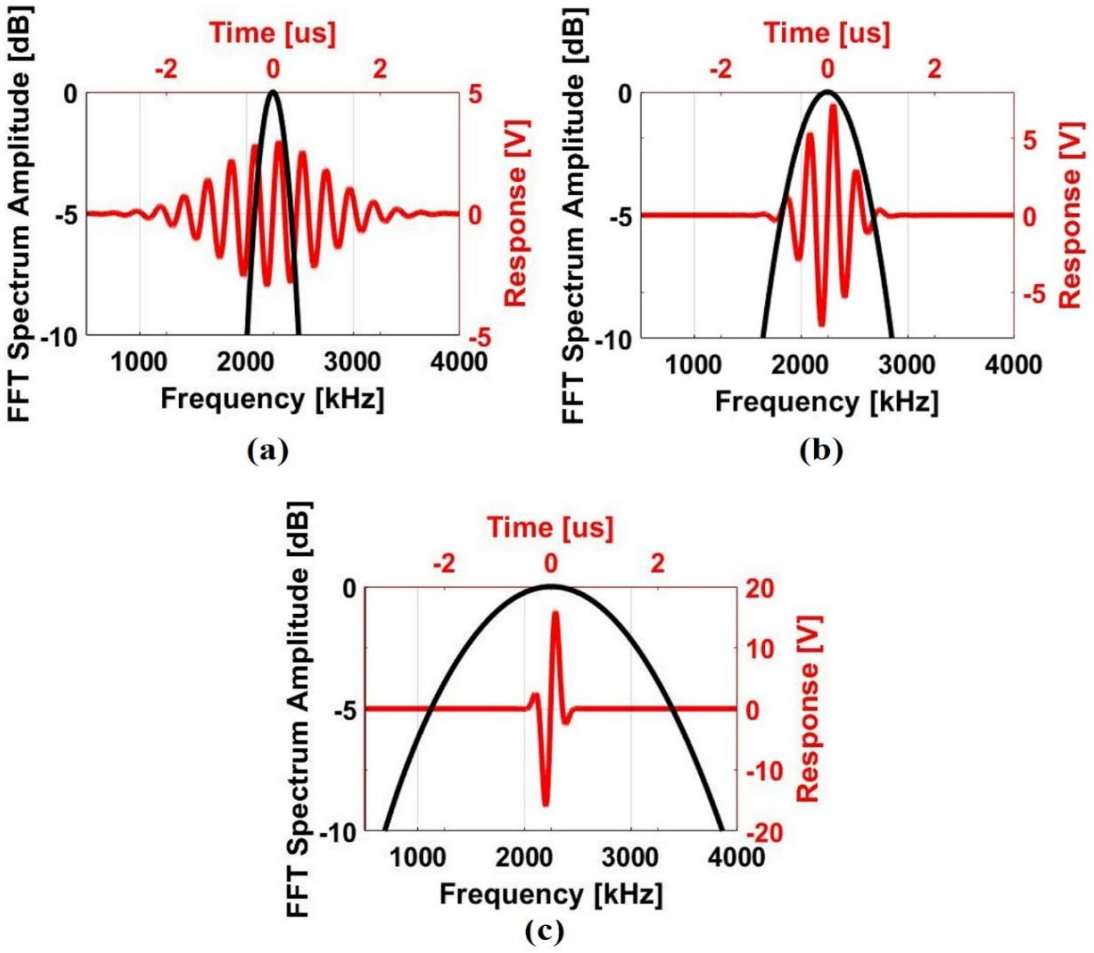

Figure 1-3: Transmitted ultrasound pulse with bandwidth of: (a) 17 %; (b) 55 % and (c) 110 %

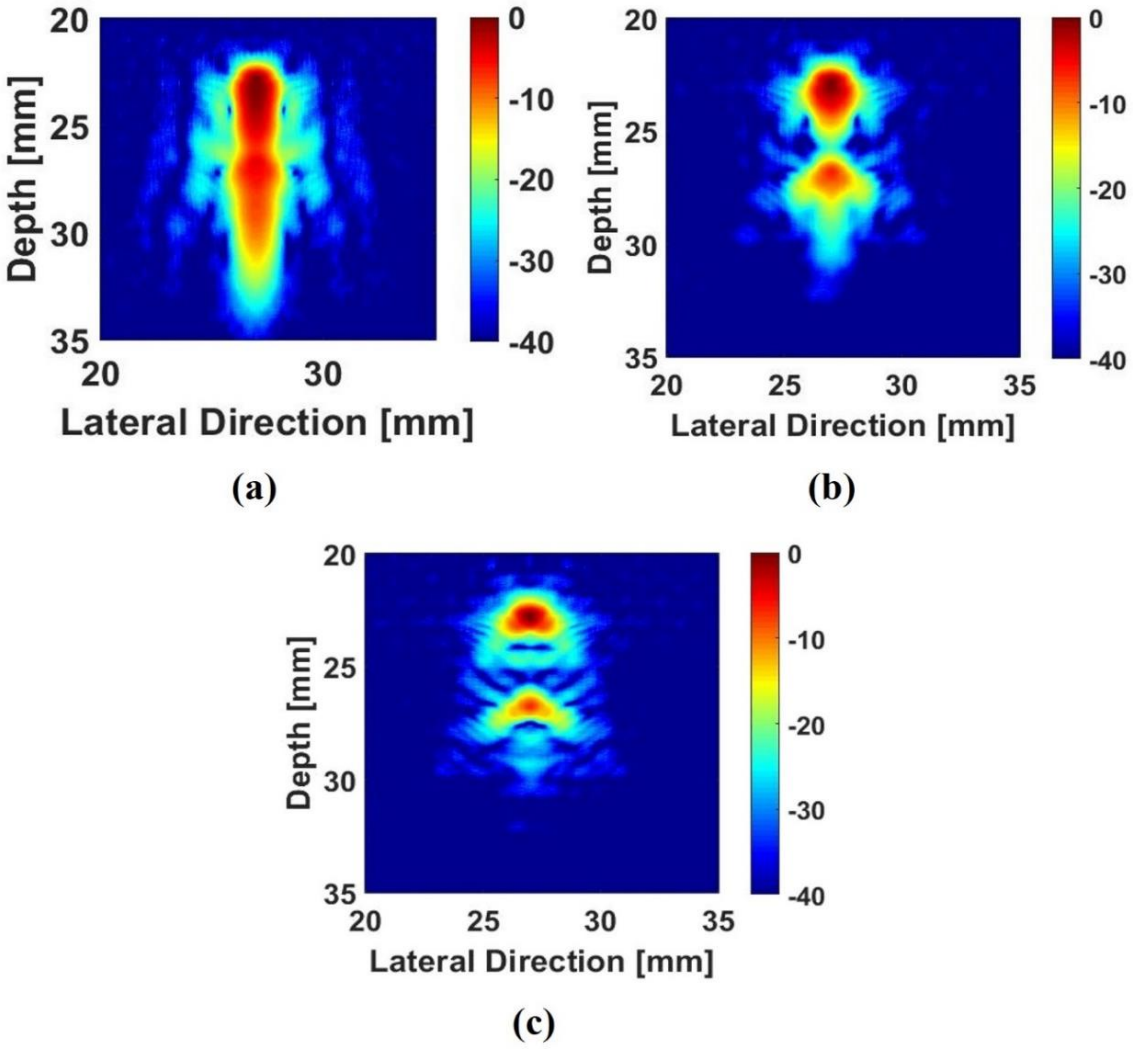

Figure 1-4: TFM image generated from ultrasound excitation pulse with bandwidth of: (a) 17 %; (b) 55 % and (c) 110 %

In addition to improving imaging resolution, wider transducer operational bandwidth can offer advantages in the signal processing chain of contemporary imaging systems. Frequency diverse signal processing techniques such as split spectrum processing [18] benefit from wider transducer bandwidth when applied to speckle reduction [19] and contrast enhancement [14].

Consequently, the potential of enhancing the performance of an ultrasonic transducer, either a single element or an array ultrasound transducer, will be investigated in this thesis by using different fractal geometries.

1.1.3. Objectives

First of all, the problem space of the work described in this thesis is to explore new methods of developing ultrasound devices, including both single element and array ultrasound transducers, with improved performance, particularly in terms of bandwidth enhancement, using fractal geometries. Secondly, the performance of these fractal ultrasound transducers needs to be characterized theoretically and experimentally. In order to achieve these two main targets, the following tasks will be addressed in this thesis.

- Understand the fundamental principle of using resonators with varying length scales to produce a range of resonating frequencies, where the operating bandwidth extension of the entire system can be achieved.
- Design and build FE models of fractal ultrasound transducers using a commercial FE software package. The operational behaviour of these fractal ultrasound transducers will be analysed theoretically using these FE models.
- Explore fabrication methods for manufacturing the ultrasound transducers, which are designed with different fractal geometries.
- Evaluate the performance of fabricated fractal ultrasound devices experimentally and compare with equivalent transducers, either commercial devices or designed through this work.

1.2. Knowledge Contribution

This PhD project provides a new configuration for piezoelectric composite ultrasound transducers, which incorporates a self-similar fractal geometry to introduce varied element length scales in the composite microstructure. Four different well known fractal geometries, Sierpinski Gasket (SG), Sierpinski Carpet (SC), Cantor Set (CS) and Cantor Tartan (CT), were studied and utilised in the design of different configurations of piezoelectric composite. The behaviour of these piezoelectric fractal composites was investigated by employing a FE modelling approach. The initial prototypes of a SG fractal single element ultrasound transducer and a CS fractal ultrasound array transducer were fabricated using two different fabrication techniques. The performance of both fabricated fractal ultrasound transducers was fully characterised experimentally to validate the FE simulation results and clearly demonstrates improved operational performance, including bandwidth enhancement, sensitivity increase and excellent beam forming ability. Consequently, the list detailed below describes the main contribution to knowledge disseminated in this thesis.

- Demonstrated feasibility of applying fractal geometry as the microstructure of a piezoelectric composite transducer, resulting in both sensitivity and bandwidth improvements. This key output from the thesis is a validation of the phenomenon of coupling multiple resonances (length scales) within the microstructure of the device, as introduced by the fractal geometry itself.

- Conducted design optimisation for both single element and array transducer configurations incorporating a fractal geometric microstructure, with specific cognizance to limitations in current piezoelectric transducer fabrication techniques.
- Fabricated world-first fractal composite transducer, using the Level IV Serpinski Gasket configuration, which importantly demonstrated improved operational performance over both an equivalent conventional 1-3 piezoelectric composite and a commercial single-element device.
- Realised a Level II Cantor Set fractal geometry within a fabricated linear array device and again, demonstrated improved operational performance over an equivalent conventional 2-2 piezoelectric composite array structure.
- Utilised simulation to design an advanced fractal linear array implementing a Cantor Tartan microstructure, with a predicted 9% enhancement in operational bandwidth over the Cantor Set array transducer due to an increase in the length scales within the array element by a factor of 4.

1.3. Thesis Structure

The complete thesis is comprised of a further 6 Chapters.

Chapter II reviews the key methodologies and fundamental techniques associated with piezoelectric transducer development. In particular, the piezoelectric effect, 1-3 piezoelectric composite transducer design criteria and ultrasonic phased array techniques are introduced in detail. The state of art for enhancing the ultrasound transducer

performance is also reviewed in this Chapter. Finally, the concept of the fractal geometry is introduced with reference to the piezoelectric composite structure.

Chapter III describes the integration of the SG fractal geometry into the design of a single element ultrasound transducer. The performance of this SG fractal transducer is fully characterised and compared with a conventional 1-3 composite using the FE modelling method. A SG fractal single element transducer is then fabricated using the 'place-and-fill' technique and characterised experimentally. Good correlation is demonstrated between the FE simulated results and the experimentally acquired data. It is found that by using the SG fractal geometry to design a piezoelectric composite, multiple resonant modes can be possessed by the SG fractal design due to its varying pillar length scale. Interestingly, both bandwidth and sensitivity enhancement were achieved by the fractal composite, when compared to a conventional parallelepiped 1-3 composite design.

With the confidence, provided in Chapter III, of using the FE modelling approach to study the transducer performance, Chapter IV describes a purely simulation study for the design of a SC fractal composite. The concept of enhancing transducer bandwidth by employing a fractal geometry is again demonstrated in this Chapter.

Chapter V introduces the third fractal geometry, CS fractal geometry, for the purpose of designing a linear array transducer. When compared with the SG and SC fractal composite reported in Chapter III and IV, respectively, a 2-2 composite with CS fractal geometry can be fabricated easily using traditional the 'dice-and-fill' technique and is an excellent candidate for use in an array structure. Again, FE simulation is used to design a CS fractal

composite and an equivalent conventional 2-2 composite and the optimised designs were used to fabricate 24-element linear arrays. The fabricated devices were characterised and evaluated using a number of standard techniques. Interestingly, as the CS fractal array has a non-uniform periodicity across its aperture, a reduction in mechanical cross-talk can be achieved. More importantly, the experimental results demonstrate a better bandwidth and sensitivity performance for the CS fractal array, which is reinforced a practical NDT evaluation to illustrate its improved imaging ability.

Chapter VI investigates an advancement on the CS fractal design, in which a CT fractal geometry with a more complex microstructure is simulated to evaluate further enhancement of the bandwidth performance of a linear array.

Chapter VII draws a number of conclusions based on the results obtained in Chapter III, IV, V and VI. While the work presented in the thesis demonstrates the benefit of incorporating the fractal architecture into piezoelectric composite based transducers. There are opportunities that have yet to be explored and a number of themes for future work for piezoelectric fractal composite transducers are introduced. In particular, advanced fabrication techniques are proposed, where ultrasonic transducers incorporating more complicated fractal geometries could be manufactured more efficiently.

1.4. Publication from this Work

Peer-Reviewed:

H. Fang, Z. Qiu, R. L. O'Leary, A. J. Mulholland and A. Gachagan, "Broadband 1-3 piezoelectric composite transducer design using Sierpinski Gasket fractal geometry," IEEE Transactions on Ultrasonics, Ferroelectrics, and Frequency Control, vol. 65, no. 12, pp. 2429-2439, 2018. DOI: 10.1109/TUFFC.2018.2874384

Conference Publications:

H. Fang, Z. Qiu, R. L. O'Leary, A. Gachagan, and A. J. Mulholland, "Improving the operational bandwidth of a 1-3 piezoelectric composite transducer using Sierpinski Gasket fractal geometry," *IEEE Int. Ultrason. Symp. IUS*, 2016.
DOI: 10.1109/ULTSYM.2016.7728694

H. Fang, Z. Qiu, R. L. O'Leary, A. Gachagan, and A. J. Mulholland, "Linear ultrasonic array incorporating a Cantor Set fractal element configuration," *IEEE Int. Ultrason. Symp. IUS,* 2017. DOI: 10.1109/ULTSYM.2017.8092280

H. Fang, Z. Qiu, R. L. O'Leary, A. Gachagan, and A. J. Mulholland, "Linear ultrasonic array development incorporating Cantor Set fractal geometry," *IEEE Int. Ultrason. Symp. IUS*, 2018. DOI: 10.1109/ULTSYM.2018.8580016

Z. Qiu, **H. Fang**, R. L. O'Leary and A. Gachagan, "Broadband piezocrystal transducer array for Non-Destructive Evaluation imaging applications," *IEEE Int. Ultrason. Symp. IUS,* 2018. DOI: 10.1109/ULTSYM.2018.8579855

Conference Contributions:

H. Fang, Z. Qiu, R. L. O'Leary, A. Gachagan, and A. J. Mulholland, "Fractal geometry 1-3 piezoelectric composite with improved bandwidth," Presented at *International Workshop on Acoustic Transduction Materials and Devices (IWATMD),* 2016.

H. Fang, Z. Qiu, R. L. O'Leary, A. Gachagan, and A. J. Mulholland, "Linear ultrasonic array design using Cantor Set fractal geometry," Presented at *International Workshop on Acoustic Transduction Materials and Devices (IWATMD),* 2018.

CHAPTER II

REVIEW OF ULTRASONIC TRANSDUCER DEVELOPMENT

Ultrasound is a mechanical sound wave with frequency beyond 20 kHz, which is the upper audible limit of human hearing system [20]. The physical properties associated with ultrasonic waves follow the same principles for all types of mechanical wave.

An ultrasonic transducer refers to a device which is employed to convert the energy of the electrical signal to mechanical vibrations or vice versa [21]. In 1915, the French physicist P. Langevin invented the first ultrasonic echo-sounding device by gluing a mosaic of thin quartz crystals between two steel plates [22]. Hence, ultrasonic transducer technology has been explored for over one hundred years and been widely used in many different fields, for example sonar[23], [24]; non-destructive testing [25], [26]; medical diagnostic imaging [27], [28] and chemical reaction control [29], [30].

In this Chapter, a literature review regarding the background knowledge for this thesis will be given, which can be mainly divided into four main sections:

- Nature of the piezoelectric effects and properties of piezoelectric materials.
- Introduction to ultrasonic transducer design, with particular focus on:
    a) Design criteria for a high performance ultrasound transducer, with particular reference to the family of piezoelectric composite ultrasound transducers.
    b) Ultrasonic phased array techniques
- Relevant technical approaches for enhancing the performance of the piezoelectric composite.
- Fundamental background on fractal geometries and related applications.

2.1. Piezoelectric Effect and Piezoelectric Material

2.1.1. Piezoelectric Effect

The piezoelectric effect was first discovered in quartz by Pierre and Jacques Curie in 1880 [31]. The piezoelectric phenomenon consists of two related effects: 'Direct effect' and 'Converse effect'. The Direct effect can be explained as application of a mechanical force to generate an electrical polarization within the piezoelectric material, with the Converse effect being the opposite condition, where the piezoelectric material can generate mechanical stress through the introduction of an external electrical field [32]. The Direct and Converse effects can be described by Equations (2-1) and (2-2), respectively [33]:

$$D_i = d_{iJ}T_J + \varepsilon_{ij}^T E_j \tag{2-1}$$

$$S_I = s_{IJ}^E T_J + d_{jI}E_j \tag{2-2}$$

where D is electric displacement, T is mechanical stress, S is mechanical strain, E is electric field. In addition, d, s and ε, are the piezoelectric constants for charge, compliance and permittivity, respectively. The definitions for these parameters are [34]:

D (C/m^2): Electric displacement is the total amount of charge per unit area which could be displaced across a conductor layer in the electric field.

T (N/m^2): Mechanical stress is the elastic force per unit area.

S (unit less): Mechanical strain is the response of the object to an applied stress.

E (N/C or V/m): Electric field is a vector field which can be defined as the electric force per unit charge.

d (m/V or C/N): Piezoelectric charge constant describes the electric polarization formed in the piezoelectric material per unit mechanical stress applied.

s (m^2/N): Elastic compliance refers to the elastic strain generated per unit stress. The inverse of the elastic compliance constant is called elastic stiffness constant, c.

ε (F/m): Permittivity defines the dielectric displacement per unit electric field applied.

As the piezoelectric effect only happens in an anisotropic material [34], the piezoelectric equations are always described in matrix form, therefore these piezoelectric constants are defined using subscript notation. Based on the IEEE standard on Piezoelectricity [35], the first number of the subscript indicates the direction of dependent variable and the second number refers to the direction of the independent variable, where the coordinate definition is shown in Figure 2-1. The Cartesian directions *x*, *y*, and *z* are represented by the coordinate denoted by the subscripts of 1, 2 and 3, respectively; shear about these axes is denoted by the subscripts of 4, 5 and 6, respectively. The positive polarization direction, *P*, is commonly selected as the positive direction of 3-axis (or *z*) as shown in Figure 2-1. For example, d_{13} means the electric polarization generated in the 1-axis per unit stress applied in direction of the 3-axis. As for the superscripts T and E, they refer to constant stress and constant electric field conditions, respectively. For example, ε_{ij}^{T} indicates the

permittivity measured under the condition of constant stress and s_{IJ}^{E} is the elastic compliance constant measured in a constant electric field.

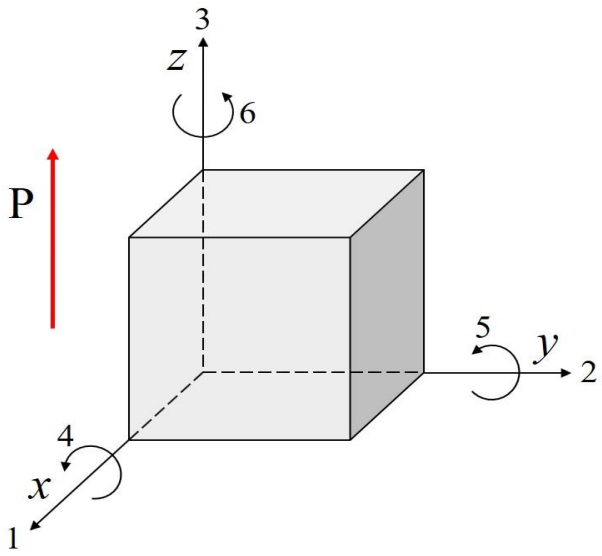

Figure 2-1: The Coordinate Definition from the IEEE standard on Piezoelectricity [35]

The electromechanical coupling coefficient, k, is very important when discussing the piezoelectric effect or piezoelectric material. This coefficient quantifies the effectiveness of the conversion between the electrical energy and mechanical vibration in the piezoelectric material and is given in Equation (2-3) [34].

$$k^2 = \frac{W_s}{W_t} \qquad (2\text{-}3)$$

where W_s is the electrical energy converted with applied stress, W_t.

Similar to the other piezoelectric constants, the electromechanical coupling coefficient is also commonly cited with subscripts, k_{ij}, where the first number of the subscript indicates

the axis of electrical load connected and the second number refers to the axis of the stress excitation applied. Although there are many different electromechanical coupling coefficients depending on various combination of i and j, two coupling coefficients k_{33} and k_t are particularly of the interest in terms of ultrasound transducer design. The bar-mode coupling coefficient, k_{33}, refers to the coupling within a tall and thin bar when a finite 1D stress is applied across the thickness, z, axis as shown in Figure 2-1. The thickness coupling coefficient k_t, describes the coupling under the condition of zero strain in the x- y plane.

There are five other essential parameters when designing an ultrasound transducer using a piezoelectric material: material density, ρ (kg/m^3); longitudinal and shear sound velocities, v_l and v_s (m/s); characteristic acoustic impedance, Z ($MRayl$) and Curie temperature, T_c (℃). The acoustic impedance is calculated as the product of density and longitudinal velocity, as described in Equation (2-4). It is worth noting that T_c refers to the upper operational temperature limit for the piezoelectric material, after which the aligned polarization within the piezoelectric metrical starts to reduce and impact on the performance of the material [36].

$$Z = \rho \cdot v \tag{2-4}$$

2.1.2. Piezoelectric Material

The piezoelectric materials can be mainly divided into four different groups: piezoceramics, piezopolymers, piezocrystals and piezoelectric composites.

1) Piezoceramics

The piezoceramics are the most commonly used piezoelectric materials for ultrasound transducer design. One of the well-known piezoceramics is Lead Zirconate Titanate (PZT). The PZT has two main classifications, piezoelectrically hard and soft types [37]. PZT-4 and PZT-5H are two typical hard and soft piezoceramic, respectively. The piezoelectric coefficients, such as k_t and d_{33}, and permittivity is higher for the PZT-5H when compared to the PZT-4, which makes PZT-5H a better choice for pulse-echo application. However, PZT-4 has a higher curie temperature, T_c, which is more suitable for high power output ultrasound applications.

2) Piezopolymers

Polyvinylidene fluoride (PVDF) is the most representative piezopolymer material. This material has a low acoustic impedance, which can provide a good coupling with the ultrasonic medium in underwater sonar and biomedical imaging applications. However, the permittivity and piezoelectric coefficient of PVDF are low, which makes PVDF a poor choice for an ultrasound transmitter.

3) Piezocrystals

Before the discovery of piezoelectricity in ceramics was published in 1946, single crystals, such as quartz, had been used as the main piezoelectric materials [38]. However, the single crystals were rapidly replaced by a family of ceramics, PZT, in industrial applications after the 1950s, as the piezoelectric response possessed by ceramics was far better than any known single crystals at that time. Four decades later in 1990, Shrout *et al*. studied

the dielectric behaviour of a new family of single-crystal piezoelectric materials, $Pb(Mg_{1/3}Nb_{2/3})O_3 - PbTiO_3$ (PMN-PT) [39]. Subsequently, the utilization of PMN-PT as the active phase in an ultrasound transducer was then studied for the first time by Toshiba [40]. In 2000, this new type of the piezocrystal material has been widely recognized for its outstanding piezoelectric performance over traditional piezoceramic materials, which was considered as a revolution for ultrasound transducers development [38]. The bar-mode coupling coefficient and piezoelectric strain constant of PMN-PT is very high, $k_{33} \approx 0.9$ and $d_{33} \approx 1400\ pm/V$. However, the drawback of the PMN-PT is that it has a low Curie temperature (~90 ^{o}C) and the fabrication cost is also much higher when compared to conventional ceramics [41].

A summary of the material properties of PZT-4, PZT-5H, PVDF and PMN-PT are listed in Table 2-1.

4) Piezoelectric Composites

The typical requirement for a piezoelectric material for implementation of a high performing ultrasonic transducer can be summarized as [42]:

a) Possessing high electromechanical coupling factor in order to have high sensitivity.
b) Ideal acoustic impedance matching between transducer and load to provide wide operating bandwidth and enhance system sensitivity.
c) Providing high permittivity for lower input electrical impedance, thus allowing enhanced electrical matching to the electrical sub-system.

d) A pure undistorted thickness mode vibration, where the details of this mode will be explained in Section 2.2.2.2.

Table 2-1: Properties of selected piezoelectric material

	Piezoceramic	**Piezoceramic**	**Piezopolymer**	**Piezocrystal**
	Hard	Soft		
	PZT-4	PZT-5H	PVDF	PMN-PT
$\boldsymbol{\rho}$ **(kg/m^3)**	7700	7450	1780	8100
$\boldsymbol{v_l}$ **(m/s)**	4670	4200	2560	4000
$\boldsymbol{Z}$ **(MRayl)**	36	31	4.5	32
$\boldsymbol{T_c}$ **(ºC)**	330	235	~205	65-95
$\boldsymbol{d_{33}}$ **(pm/V)**	290	574	30	1540
$\boldsymbol{\epsilon_{r33}^S}$	700	1220	10-12	910
$\boldsymbol{\epsilon_{r33}^T}$	1320	2870	6.28	5400
$\boldsymbol{k_t}$	0.47	0.52	0.19	0.60
$\boldsymbol{k_{33}}$	0.68	0.75	0.13	0.91

** Material properties in this table are obtained from various academic and commercial source. Ceramic: Manufacture's online database (Meggitt Ferroperm, Kvistgard, Denmark); PVDF* [43]*; PMN-PT* [44]*. All data are only for guidance.*

To meet these transducer design requirements, the concept of a ‘piezoelectric composite’ material was proposed, which refers to a material comprising an active piezoelectric phase, typically piezoelectric ceramics or piezocrystal, and a passive phase, typically an epoxy polymer material [45]. This active transducer material will be referred to as a composite in the remainder of this thesis.

The theory behind this ‘composite design’ can be simply explained as tailoring the active material properties by taking advantage of key properties in the piezoelectric and polymer phases. For PZT ceramic, it can provide high permittivity which corresponds to the electrical impedance of the ultrasound transducer and is very critical in terms of the transmission efficiency. Moreover, the PZT ceramic has a high electromechanical coupling factor, which determines the peak signal level and bandwidth in both transmission and reception mode of the transducer [12]. As for the epoxy polymer, it can decouple the piezoelectric material laterally, which leads to efficient vibrational performance for the piezoelectric to maximise electromechanical conversion. Another benefit of using composite design with epoxy polymer material is that the acoustic impedance of the composites can be tailored to match operation into low impedance loads and, hence, increase the energy transfer efficiency. Such piezoelectric composite configurations, when designed correctly, can attain high sensitivity whilst being well matched to a low acoustic impedance load [46], [47].

As composite is a multiphase material, some properties of the composite can be controlled by manipulating a design factor, called ‘connectivity’ [48]. There are ten possible connectivity patterns for the composite ultrasound transducer, which are represented as:

0-0, 1-0, 2-0, 3-0, 1-1, 2-1, 3-1, 2-2, 3-2 and 3-3. The first number represents the connectivity in terms of the number of dimensions, see Figure 2-1, that the active material phase is connected, with the second number representing the same connectivity concept for the passive material phase [49]. The Figure 2-2 indicates three most commonly used connectivity patterns for the composite, where dark grey represents the active material phase and light grey represents the passive material phase. In this Chapter, the characteristic of the composite with 1-3 connectivity will be introduced in detail, with both the 1-3 and 2-2 connectivity configurations utilised in the transducer designs generated in this thesis.

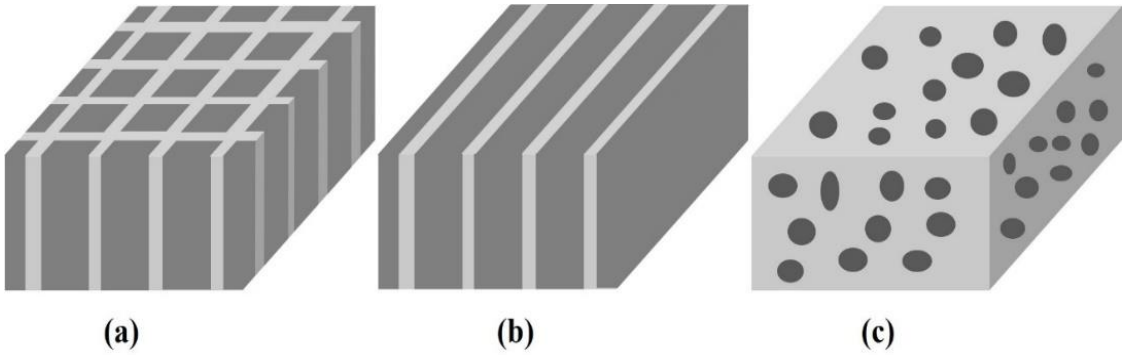

Figure 2-2: Composite connectivity examples: (a) 1-3 connectivity; (b) 2-2 connectivity and (c) 3-0 connectivity.

2.2. Piezoelectric Ultrasound Transducer

Having explored the nature of the piezoelectric effect and different types of piezoelectric material, in this section, the fundamental knowledge of an ultrasound transducer incorporating a piezoelectric material will be explored and several basic design rules for designing a highly performing ultrasound transducer will be discussed.

2.2.1. Single Element Piezoelectric Ultrasound Transducer

Typically, a piezoelectric ultrasound transducer comprises three main components: piezoelectric active layer, matching layer and mechanical damping material. Some other ancillary components are also utilised, such as transducer casing, electronic circuitry and electrical connection. A basic single-element ultrasound transducer can be described by Figure 2-3.

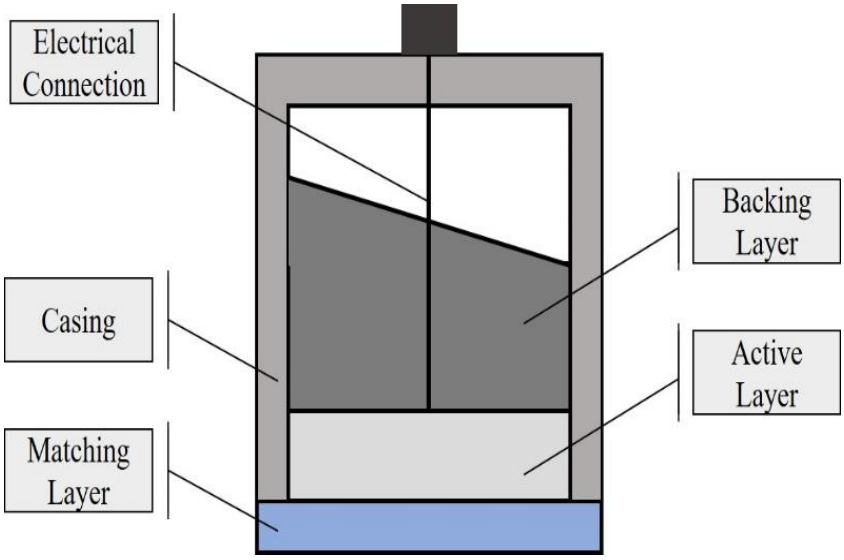

Figure 2-3: Schematic of a single-element ultrasound transducer

1) Piezoelectric Active Layer

The piezoelectric active layer is the heart of an ultrasound transducer, where the energy conversion between the electrical signal and the mechanical vibration happens. The behaviour of an ultrasound transducer is largely determined by the properties of the chosen piezoelectric materials. For example, the resonance frequency of a piezoelectric active

layer is depended on its thickness and longitudinal sound velocity, which can be calculated theoretically using Equation (2-5).

$$f_{mech} = \frac{v_l}{2 \times tk} \tag{2-5}$$

where f_{mech}, v_l and tk are the mechanical resonance frequency, sound velocity and thickness of the piezoelectric active layer. Importantly, Section 2.2.2 will detail the design rules for 1-3 composite materials.

2) Matching Layer

The function of the matching layer is to reduce the mechanical impedance mismatch between the piezoelectric active material and acoustic impedance of the load medium. Typically, the load medium will have a lower acoustic impedance, for example gaseous and liquid media. Basically, there are two key design rules for the matching layer:

- The thickness of the matching layer should be quarter wavelength of interest [50].
- The characteristic acoustic impedance of the matching layer Z_m should follow the relationship described in Equation (2-6),

$$Z_m = \sqrt{Z_T Z_L} \tag{2-6}$$

where Z_T is the acoustic impedance of the composite transducer and Z_L is the acoustic impedance of the load.

Sometimes, when the load medium has a very low impedance property (e.g. air), multiple layers of matching are necessary to maximise coupling efficiency from the transducer to the load medium [51], and vice versa.

However, the utilization of the matching layer also has some drawbacks. One of the most significant negative influences is introducing extra resonance modes to the transducer impedance profile. This phenomenon can be simply explained as the matching layer itself will introduce an extra boundary into the overall system [10].

3) Mechanical Damping Material

As the piezoelectric materials are inherently resonant, the impulse response of such a material will result in reverberation within the transducer, which manifests itself as ringing in the time domain signal. For the unbacked, also called air backed, composite ultrasound transducers, the large acoustic impedance mismatch will lead to the loss of sound energy to be minimum at the air back boundary. In which case, the sensitivity of the transducer can be maximised, but the bandwidth of transducer will decrease due to reverberation from the back of the transducer [52].

In order to reduce the extent of the reverberation within the transducer, reducing the temporal ringing and increasing the operational bandwidth, a backing block material is added to the rear face of the transducer, but this is at the expense of the overall device sensitivity as some energy is lost into the backing block [53]. Consequently, a compromise should be made between higher bandwidth and transducer system sensitivity, or an acceptable signal to noise ratio (SNR). In 1994, Hall made a simple rule for determining

the acoustic impedance of the backing material, which is taking half of the acoustic impedance of the active material as the value of the backing material [54].

To summarise, by carefully designing a backing block and matching layer for a composite transducer, the performance of the whole transducer system can be improved, especially in terms of the bandwidth extension and sensitivity promotion.

4) Ancillary Components

The most commonly seen ancillary components in an ultrasound transducer are electrical connection, transducer casing and electronic circuitry.

The electrical connection is used to connect the piezoelectric material to electrical instrumentation. Commonly used cable includes coaxial and twisted pair, which have the ability to provide good electrical shielding.

The function of the transducer casing is to obviously provide physical protection to the transducer. In addition, the transducer casing is metallic and connected to the electrical ground, in order to provide additional electrical shielding.

In some cases, an electronic circuit is required for the purpose of providing electrical impedance matching between the transducer and the electrical signal generator, thus promoting efficient power transfer. An equivalent circuit of a piezoelectric resonator can be represented by a Butterworth–Van–Dyke (BVD) circuit model, which is shown in Figure 2-4 [55]. Four electronic components C_0, C_s, L_s and R_s are employed to represent the complex electrical impedance of a free-standing piezoelectric resonator around its resonance frequency, where C_0 is the equivalent capacitance, C_s and L_s model the

resonance behaviour of the piezoelectric resonator and R_s is the represent the mechanical loss.

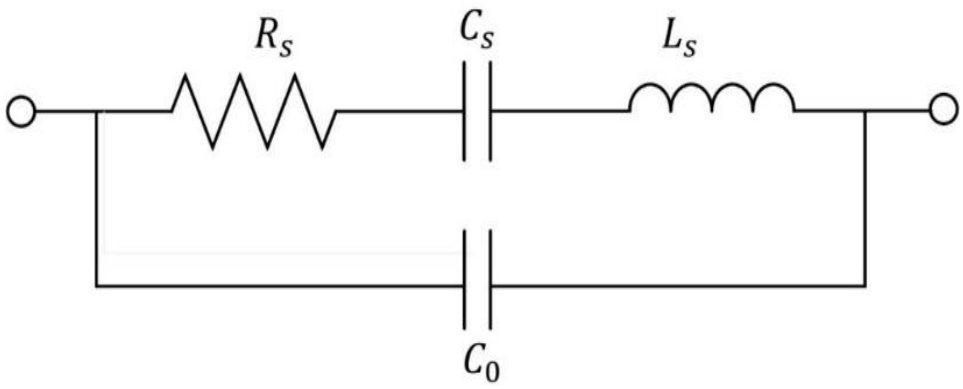

Figure 2-4: Ultrasonic transducer BVD circuit model

According to the BVD model, the ultrasonic transducer can be treated as capacitive naturally, which would lead to the impedance of the transducer being a complex value. The imaginary part of the impedance results in reactive power, which is a waste of energy and would be a stress for the electrical energy source. In order to cancel the imaginary part of the complex electrical impedance, a simple LC network highlighted with red dash box in Figure 2-5 can be easily designed [56]. By doing so, a simple electrical impedance match between the transducer, $\mathbb{Z}$ and the electrical source V_s with an internal resistor, R_s, can be provided.

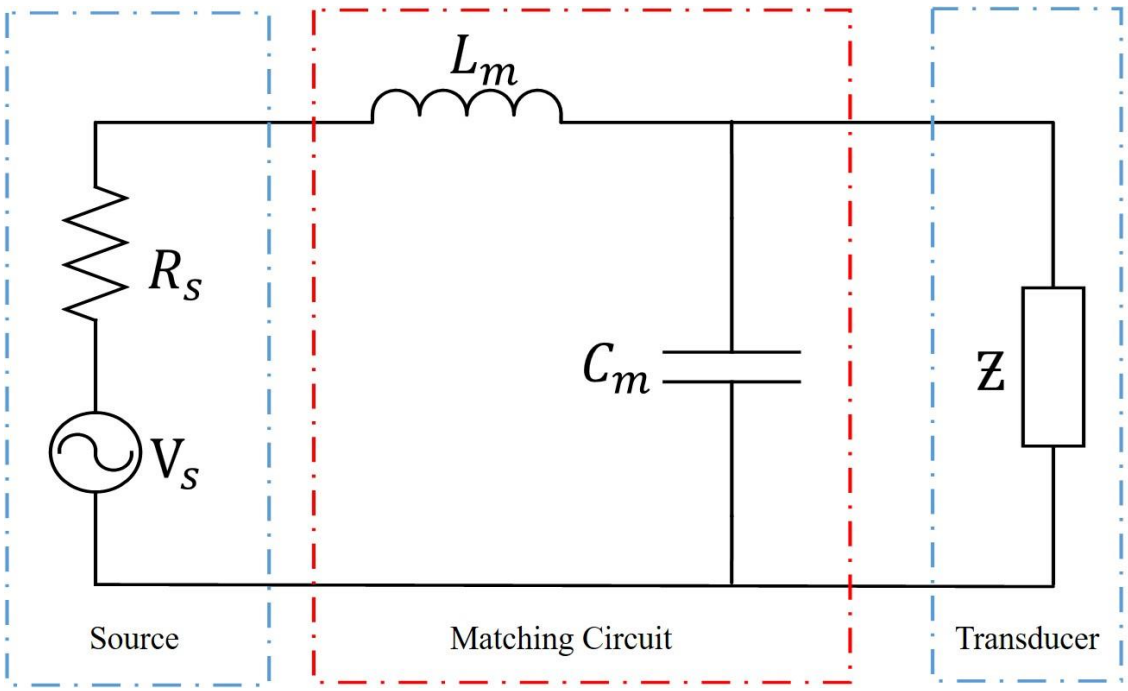

Figure 2-5: Example of LC matching circuit

2.2.2. 1-3 Piezoelectric Composite

1-3 composite with parallelepiped pillars is one of the most commonly used structures for ultrasound transducer design. The Figure 2-6 shows a schematic representation of a quarter symmetry section of a unit cell from a 1-3 composite material with parallelepiped pillar. The internal pillar configuration of a 1-3 composite can be determined by 3 parameters [10].

- Half Ceramic Pillar Width (w_2)
- Half Cell Pitch (w_1)
- Thickness (tk)

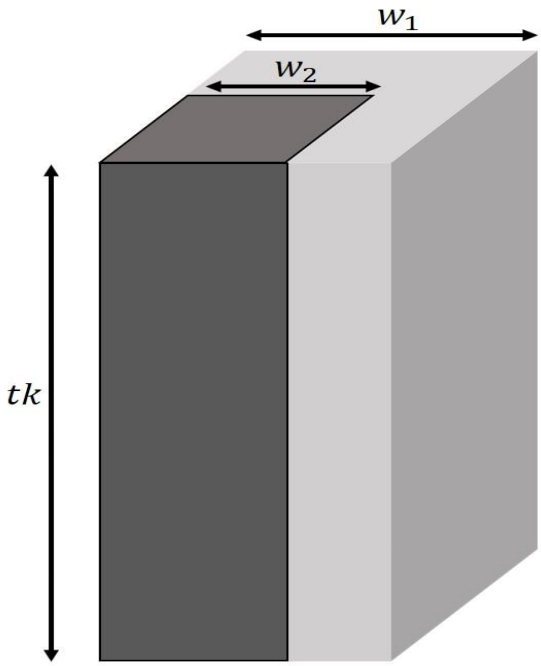

Figure 2-6: 3D schematic representation of a quarter symmetric section of a unite cell from 1-3 composite with square pillar, where dark grey is the active piezoelectric material and light grey is the passive polymer material.

Based on these three fundamental parameters, the other important parameters of a 1-3 composite can be determined as follows:

Ceramic Volume Fraction (VF): The percentage of the piezoelectric ceramic in the entire composite.

$$VF = (w_2/w_1)^2 \tag{2-7}$$

Pillar Aspect Ratio (AR): The ratio of the lateral width of the composite plate to its thickness.

$$AR = 2w_2/tk \tag{2-8}$$

Kerf Width (KW): The gap between two piezoelectric ceramic pillars.

$$KW = 2(w_1 - w_2) \tag{2-9}$$

Pitch Width (PW): The distance between the centres of two adjacent pillars.

$$PW = 2w_1 \tag{2-10}$$

The performance of a 1-3 composite is largely depended on these parameters and will be analysed in detail in the following section.

2.2.2.1. Fundamental Design Rules

1) Ceramic Volume Fraction

In 1991, Smith and Auld developed an isostrain model to simulate the influence of the VF on the performance of a 1-3 composite [57]. This model was then verified experimentally by Hayward [58]. The Smith-Auld model can be readily employed to determine the following equivalent transducer parameters as a function of ceramic volume fraction: the thickness-mode coupling coefficient, k_t; acoustic impedance, Z; relative permittivity, ε_{r33}^{S} and longitudinal sound velocity, v_l. By way of example, these data for a 1-3 composite comprising for PZT-5H (Meggitt A/S, Kvistgard, Denmark) as the active phase and CY1301/HY1300 hardset polymer (Robnor Resin Ltd, UK), which will be

referred as ‘hardset polymer’ in the rest of this thesis, as the passive phase are shown in Figure 2-7.

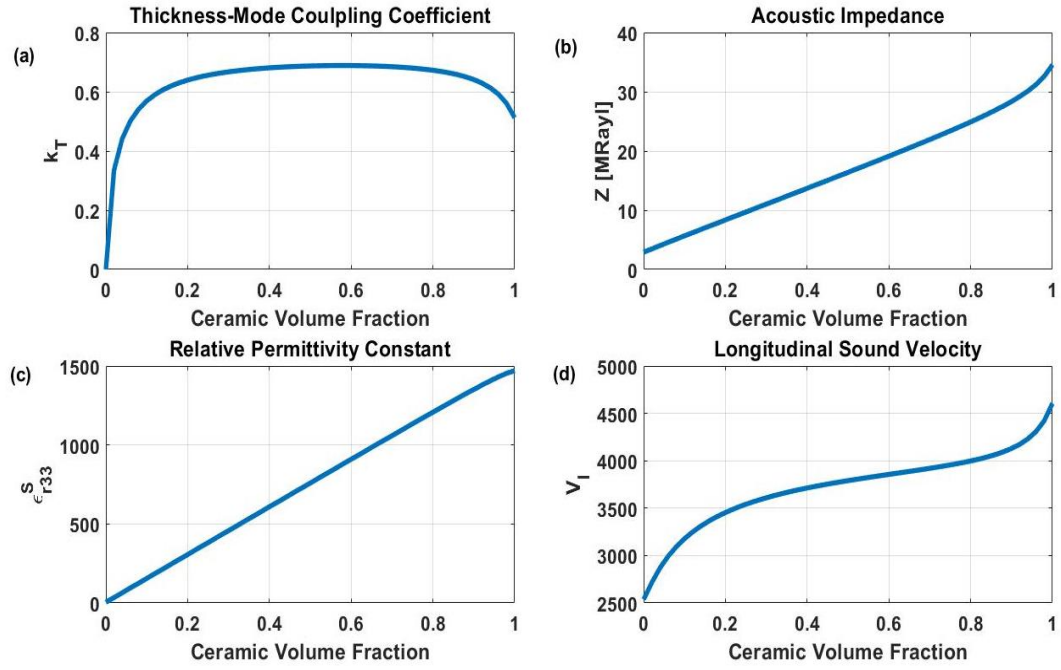

Figure 2-7: Coefficients and parameters of 1-3 composite comprising PZT-5H and CY1301/HY1300: (a) thickness-mode coupling coefficient; (b) acoustic impedance; (c) relative permittivity at constant strain; (d) longitudinal velocity

It can be seen from the Figure 2-7, k_t is effectively equal across the VF range 0.2-0.8 and importantly, is ~0.65 which compares very favourably to the 0.5 value for the raw PZT-5H material. The coupling efficiency drops below 0.2 VF due to lateral clamping and above 0.8 VF as less lateral energy can be absorbed by the polymer phase. The v_l within the composite material shows an approximately linear relationship with the VF ranging from 0.2 to 0.8. However, at very high (> 0.8) and very low (< 0.15) VF value, the v_l increases or decrease dramatically due to the same physical reasons for the reduction in k_t. As for Z and ϵ^S_{r33}, a linear relationship is maintained with respect to VF.

2) Pillar Aspect Ratio

With regard to AR, it has been verified by Hossack that AR does not have great influence on v_l within the composite material, except in the condition of very low VF (< 0.2) [12]. When VF is smaller than 0.2, v_l decreases significantly when the AR goes higher. Similarly, the AR will not affect k_t largely unless VF is smaller than 0.2. When VF is smaller than 0.2, k_t will decrease significantly with the increased value of AR and reaches minimum at AR equals to 0.6 [12]. There is an important threshold value called, Maximum Pillar Aspect Ratio (MPAR), proposed by Bennett [10]. This threshold value defines the maximum value of AR as a function of VF for sample 1-3 composite configurations. MPAR provides a practical fabrication limit for a 1-3 composite design and ensures a strong uniform thickness mode vibration, by effectively de-coupling any parasitic lateral modes from the operational frequency band. This work introduced the concept of transducer surface dilation quality factor, Q_{dil}, defined in Equation (2-11), to quantify the vibrational characteristic of a piezoelectric material, where ω_i is the radial frequency of the *i*th resonance mode and D_{ave} and D_{max} are the surface average and maximum displacement, respectively. A factor of 1 is a perfectly homogeneous displacement across the entire transducer aperture width.

$$Q_{dil} = \frac{D_{ave}(\omega_i)}{D_{max}(\omega_i)} \tag{2-11}$$

3) Kerf Width & Pitch Width

The KW and PW is limited by the technology used in the composite fabrication process. For this thesis, the smallest KW using equipment in the Centre for Ultrasonic Engineering (CUE) is 50 μm. Both KW and PW are directly related to the value of VF.

To summarise, the basic and simple rule of designing a classic 1-3 composite with minimum lateral parasitic resonance effect is to use $0.3 < VF < 0.8$ and employ as low a value of AR that can be practically manufactured. It should also be noted that the stiffness of the filling polymer material plays a critical role in both the fabrication process and in damping lateral energy within the device, which can influence the working efficiency of the transducer[12]. It has been shown that utilising a soft setting polymer can obtain a better coupling factor for a composite material when compared to a hard setting polymer under the same volume fraction conditions [10]. However, the soft set polymer has a higher Poisson's ratio, which can decrease the power transfer efficiency from the transducer to the load, and also is more challenging to process during fabrication.

2.2.2.2. Vibration Mode within the Composite

In the 1-3 composite plate, there are four different fundamental modes: Width-Dilational Mode, Thickness Mode, Inter-Pillar Mode, Intra-Pillar Mode. These four modes are now explained in detail.

1) Width-Dilational Mode

The width-dilational mode is caused by the finite lateral dimensions of the composite material. This mode can also be termed a plate mode for a rectilinear shaped device or

radial mode for a circular shaped device. This mode activity can be described as the mechanical motion in the lateral dimension with the electric field applied in thickness dimension and is mainly determined by the elastic modulus properties of the ceramic and polymer phases [42]. The frequency location of width-dilational mode is dependent on the width dimension of the piezoceramic material and usually can be observed at a frequency far below the fundamental thickness resonance frequency of the transducer. This means that this resonance mode will not have a significant effect on the operational performance of the composite device. Moreover, the inclusion of the polymer material within the composite structure dampens the width-dilational mode.

2) Thickness Mode

The thickness mode is a direct result of the finite thickness dimension of the piezoelectric composite layer. For the majority of composite ultrasound transducers, the thickness resonance frequency is used as the fundamental operating frequency. The thickness-mode coupling factor, k_t, described in Section 2.1.1 can be obtained via the electrical impedance profile of a composite using Equation (2-12).

$$k_t = \sqrt{\frac{\pi}{2}\frac{f_{ele}}{f_{mech}}\ cot\ (\frac{\pi}{2}\frac{f_{ele}}{f_{mech}})} \tag{2-12}$$

f_{ele}: The frequency at the minimum electrical impedance and is the resonance frequency under the condition when the electrode is shorted circuit. This resonance frequency is suitable for transmission mode operation of the ultrasound transducer because at this frequency, the electrical energy can be transferred to the mechanical energy most

efficiently. Moreover, at this frequency the electrical impedance is at a minima and will be the closest match to the electrical impedance of the instrumentation, which will minimise the impedance mismatch between the electrical signal source and the transducer.

f_{mech}: The frequency at the maximum electrical impedance and is the resonance frequency under the condition when the electrode is open circuit. This resonance frequency is suitable for reception mode of the ultrasound transducer and is the natural resonance of the device governed by Equation (2-5).

3) Inter-Pillar Mode

The main reason that leads to the inter-pillar modes is the generation and propagation of Lamb wave between pillars in a composite plate with regular and periodic geometry [10], [59], [60]. This unwanted mode can couple with the fundamental thickness mode strongly and therefore cause the reduction of operating efficiency for the transducer. For the purpose of designing a more efficient 1-3 composite transducer, several researchers made some basic rules for avoiding the inter-pillar resonance behaviour or separating the inter-pillar mode away from the operating bandwidth.

- In 1985, Smith came up the idea that in order to make the transducer vibrate uniformly as a homogeneous plate, the lateral resonance mode should be pushed up to the frequency range at least twice of the thickness mode frequency [61].
- For the overall dimension of 1-3 composite plate, the distance between the centre points of two adjacent ceramic pillars has to be less than the thickness of the composite plate [62].

- The kerf width of the composite plate should be less than quarter of the shear wavelength [10].

4) Intra-Pillar Mode

The intra-pillar mode is similar to the width-dilational mode introduced previously but is restricted to the finite lateral dimension of the individual ceramic pillar instead of the whole composite material. However, these intra-pillar modes become important for the case that AR is in a range from 0.5 to 2.0 [10].

2.2.2.3. The 1-3 Composite with Different Pillar Shape

Thus far in this thesis, the fundamental knowledge of composite was introduced using the example of 1-3 composite configurations having square ceramic pillars. However, 1-3 composite designs have been reported with a variety of different shapes of ceramic pillar [59], in particular triangular and cylindrical pillar geometries.

1) Cylindrical Pillars

The cylindrical pillar shape introduces additional complexity into the fabrication process [42]. However, based on the finite element analysis reported by Hossack, the relationship between the electromechanical factor and AR in terms of thickness mode and first three lateral modes is similar to the result achieved from equivalent square pillar case [63].

2) Triangular Pillars

The triangular pillar shape could lead to the reduction of lateral or radial modes within the composite structure [63]. This hypothesis has been verified by Brown when he

successfully designed a high frequency composite transducer with triangular pillar geometry [64].

There are two ways for designing the layout of the triangular pillar composite. First method is uses the standard ‘dice-and-fill’ technique [65], which is illustrated in Figure 2-8. However, in this type of configuration, due to the existence of parallel facing edges between two adjacent pillars, inter-pillar resonances can arise.

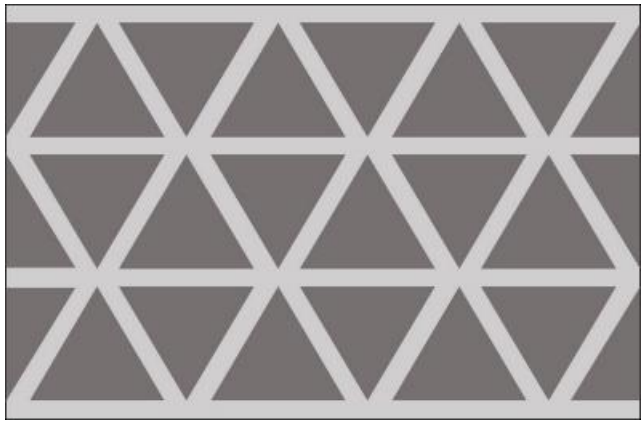

Figure 2-8: Layout of triangular pillar composite employing 'dice-and-fill' technique

In order to reduce these lateral mode resonances, an alternative triangular pillar configuration has been proposed by Hossack [12], as shown in Figure 2-9. Here each triangular pillar has to be positioned individually, which increases the complexity of the manufacturing process. However, by using this configuration, a significant improvement in maintaining a high thickness electromechanical coupling factor with increasing aspect ratio value has been reported. As the result, the MPAR for this type of configuration is higher than other equivalent pillar shapes. In Chapter III of this thesis, a composite design

using the Sierpinski Gasket (SG) fractal geometry is designed using a similar approach, in which the triangular pillar structure does not contain parallel facing edges.

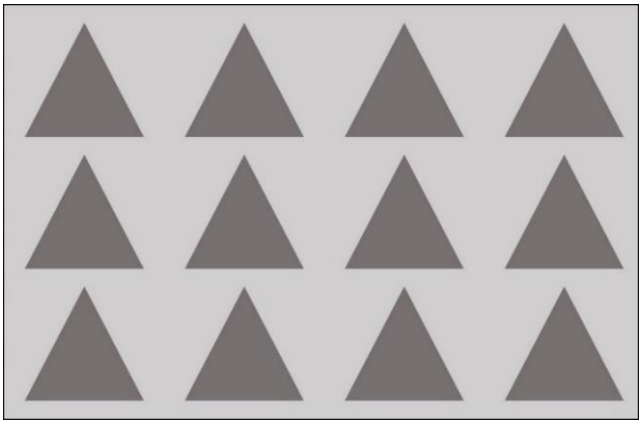

Figure 2-9: Alternative configuration for triangular pillar composite without parallel facing edges

2.2.3. Phased Array Ultrasound Technique

2.2.3.1. Phased Array Principle

The fundamental theory of phased array techniques can be simply explained in Figure 2-10. Each individual element can be excited individually, by application of different time delays, termed as the focal law. Hence beam steering or focusing can be created electronically, improving the flexibility of the imaging process [66].

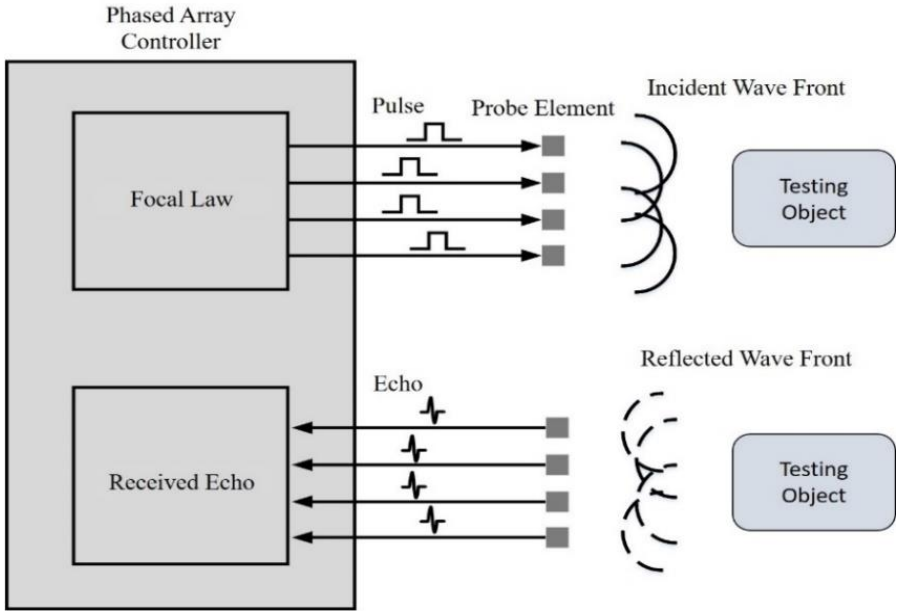

Figure 2-10: Principal of phased array technique

The ultrasound array technique is extensively used to in modern clinical diagnostic and therapeutic applications [67], such as real-time blood flow measurement [68] and non-invasive surgery [69]. In addition to the biomedical field, ultrasonic phased array techniques are also well developed in industrial applications such as non-destructive testing and evaluation (NDT&E) [70]. Important to all these applications is the high sensitivity and operational flexibility associated with array systems [71].

2.2.3.2. Phased Array Geometries

Ultrasonic array transducers can be loosely divided into three groups according to the characteristic of their geometries: one-dimensional (1-D) linear array, two-dimensional (2-D) array and annular array. The fundamental geometries of these array configurations are defined in Figure 2-11 (a), (b) and (c), respectively.

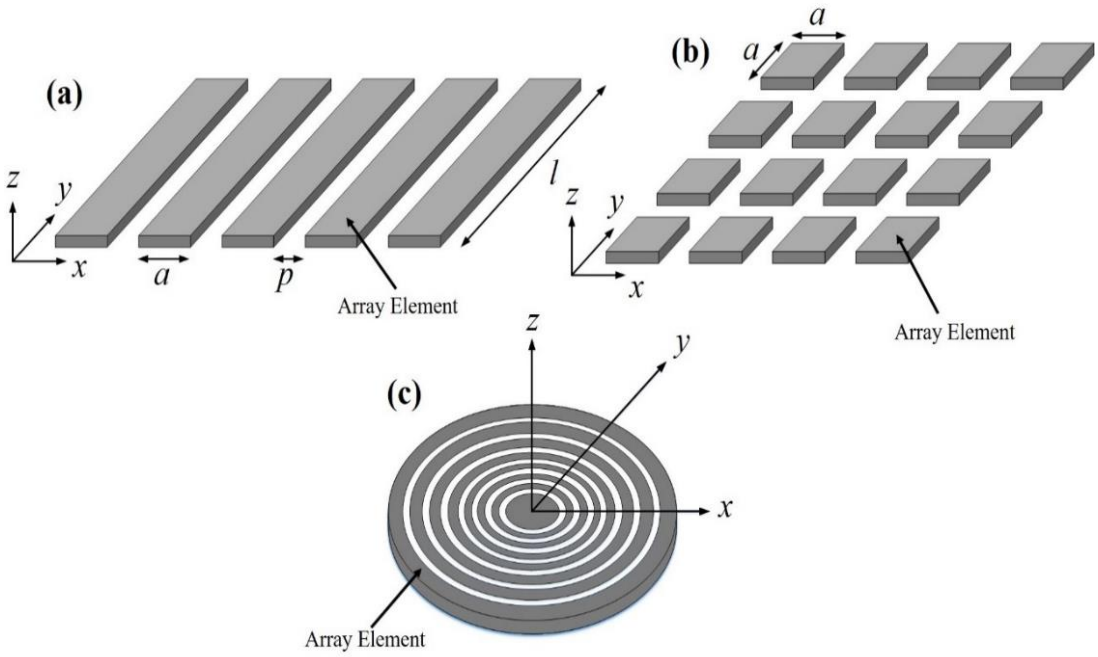

Figure 2-11: Fundamental array structure of: (a) 1-D linear array; (b) 2-D array and (c) annular array

1) 1-D Linear Array

As shown in Figure 2-11 (a), the 1-D linear array elements are only distributed along one dimension. In order to generate the sound beam which is highly directional in the azimuth plane (x-z plane) and broad in the elevation plane (y-z plane), the element length, l, should be at least ten times larger than the element width, a, which represents a geometry in which each element can be treated as a sound source from an infinitely long strip of active material [72]. In addition to that, the centre-to-centre spacing between two elements, p, is usually designed to be less than half wavelength ($p < \lambda/2$) [73] to minimise the generation of grating lobes, which are caused spatial under-sampling of the array configuration. Grating lobes manifest as acoustic energy emitted from the ultrasound

transducer at an angle away from the primary propagation path of the ultrasonic energy and can cause errors in the image due to this unwanted directional energy path [74].

2) 2-D Array

A 2-D array comprises smaller active elements distributed in two dimensions, as shown in Figure 2-11 (b). Such a structure is developed in order to have additional beam focusing and control in the elevation direction and acquire three-dimensional (3-D) volumetric imaging. However, from an aperture perspective, the complexity and number of elements increases in a 2-D design, so the electronics employed to drive individual elements is more complex and hence increases the cost of system, when compared with a 1-D array. Consequently, the concept of 1.5-D is proposed. 1.5-D array contains much less number of parallel rows of elements when compared with a fully populated 2-D array, and hence the cost and complexity of the array design can be decreased but a limited level of beam focusing and control can still be maintained in the elevation direction [75]. Another special example of 2-D array is sparse array, which also has the ability of beam steering in two dimensions. However, the element pitch in sparse array is greater than $\lambda/2$, meaning less elements are contained in the sparse array when compared to the typical dense array with element pitch less than half wavelength.

3) Annular Array

A conventional annular array structure is shown in Figure 2-11 (c). To be different from the 1-D or 2-D array mentioned above, the annular array does not have the ability of beam steering and the main purpose of designing an annular array is to provide variation in axial focal depth only.

2.2.3.3. Phased Array Imaging Modalities

Figure 2-12 demonstrates four different imaging modalities which are commonly implemented in array imaging applications: plane B-scan; focused B-scan; sector B-scan and total focusing method (TFM) [76].

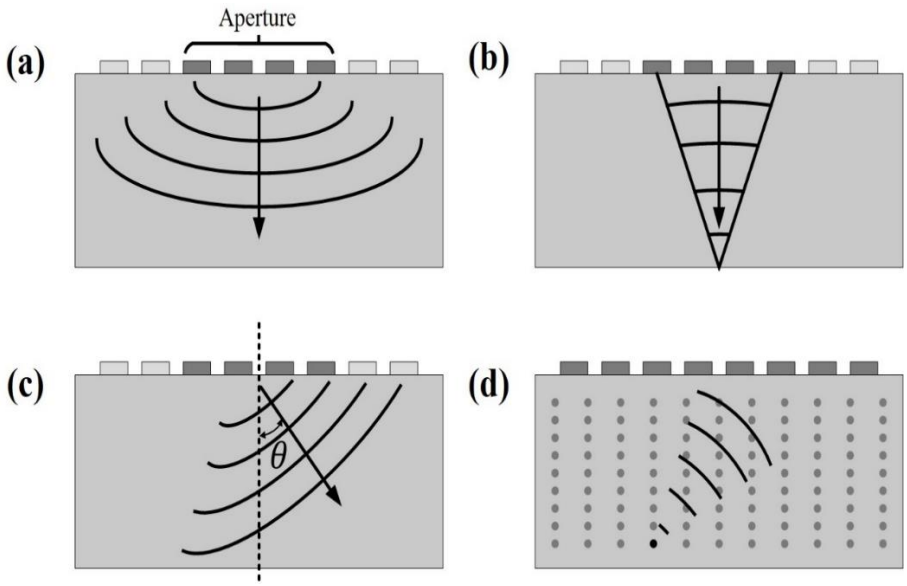

Figure 2-12: Array imaging modalities: (a) plane B-scan; (b) focused B-scan; (c) sector B-scan and (d) total focusing method

As shown in Figure 2-12 (a), a subset of array elements, named an aperture is excited in-phase and moved electronically to produce a plane beam for the plane B-scan or fired with specific time delay, known as focal law, to generate a focused, or steered beam, as shown in Figure 2-12 (b) and (c). These are conventional focal laws and are typically used in NDT&E array applications.

The TFM imaging approach, shown in the Figure 2-12 (d), refers to a more recent array implementation, in which data is acquired for every combination of transmit-receive

element pairs and stored in matrix form; this is termed Full Matrix Capture (FMC). This FMC data is then post-processed, with the ultrasonic beam focused at every single point in the region of interest; this is termed Total Focusing Method (TFM) [77]. Array instrumentation has been the limiting factor in the industrial uptake of this technique, but using current phased array controllers (PAC), TFM can be implemented practically as a imaging technique [17]. The intensity at any point $I(x,z)$ in the TFM image can be calculated using Equation (*2-13*) [17],

$$I(x,z) = \left| \sum_{i=1}^{N} \sum_{j=1}^{N} h_{tx,rx} \left(\frac{\sqrt{\left(x_{tx,i} - x\right)^2 + z^2} + \sqrt{\left(x_{rx,j} - x\right)^2 + z^2}}{v} \right) \right| \quad (2\text{-}13)$$

where $h_{tx,rx}(t)$ is the wave propagation equation, N is the total number of elements of using, tx and rx refers to the transmitter and receiver, respectively, and v is the speed of sound in the medium (this can be longitudinal or shear wave velocity depending on the modality appropriate for the TFM image). Compared with other three traditional imaging methods, TFM can produce images with enhanced resolution and contrast due to the dynamic focusing at each point in both transmission and reception mode [71].

2.3. State of Art of Novel Composite Ultrasound Transducer Design

For many years, a variety different techniques have been reported for improving the performance of a single element or an array ultrasound transducer, based on composite technology. These techniques can be roughly classified into four different methods:

a) Optimize the composite microstructure;
b) Improve the piezoelectric material properties;
c) Modify the matching/backing design;

In this section, techniques to improve composite transducer performance using these three methods are reviewed and particular attention is given to the research focusing on ultrasonic transducer bandwidth extension.

Firstly, many researchers have successfully enhanced the performance of the transducer via optimizing the microstructure of active layer in the design.

Hossack *et al.* [78] suggested a way to suppress the inter-pillar mode, which employed a distributed period or multiple period structure with regards to the pillar dimension or pillar pitch instead of repeating a single geometry periodically throughout the whole structure. By using a double period structure in a 1-3 composite design, the first inter-pillar mode was attenuated and removed from the electrical impedance spectrum successfully, compared to an equivalent conventional design. Similarly, Yuan *et al.* [79] increased the complexity of the composite microstructure further by using a random pillar pitch and

analysed the dynamic characteristics of this type of composite transducer. His simulation result showed that the random structure removed the first lateral mode, when compared to the both 1-3 and 2-2 composites.

Harvey *et al.* [80], [81] designed a composite transducer with piezoelectric fibres used as the active piezoelectric element. The microstructure of this 1-3 composite is completely random and eliminates undesired intra-pillar modes. The manufacturing technique for this configuration used 'place-and-fill' method and produced a 2-D array configuration using these randomised piezoelectric elements.

Yang *et al.* [60], [82] developed a pseudo-random composite transducer by dicing the ceramic plate with two sets of cross cuts at different angles relative to the horizontal. The pulse-echo response bandwidth of this pseudo-random composite was increased when compared to an equivalent standard 1-3 composite design.

Using a random structure for lateral mode suppression and bandwidth improvement is well recognised and widely commercialised for low frequency transducers, but for high frequency transducers, especially with microscopic dimensions, this technique is limited by the difficulties in fabrication process. As the result, Brown *et al*. [64] and Yin *et al.* [83], investigated the performance of high frequency (>20 MHz) 1-3 composite with triangular pillar geometry. This type of high frequency 1-3 composite transducer can be fabricated using the traditional "dice-and-fill" technique and has a better lateral mode reduction and bandwidth performance, when compared with the standard 1-3 composite with square pillars. Furthermore, it was reported by Hamilton *et al.* [84] that by using the

triangular shaped pillar, better surface dilatation quality can be achieved for high pillar aspect ratio composites.

Ramadas *et al.* [53] developed a wideband annular piezoelectric transducer by combining four concentric piezoelectric composite annuli, each exhibiting a different fundamental thickness mode resonance. Using a similar theory, Banks *et al.* [85] proposed two novel piezoelectric composite transducer designs to enhance the operating frequency of a composite device for air-coupled non-destructive evaluation: the dual thickness composite and conical composite design. Both designs successfully achieved a bandwidth enhancement by having a varied thickness dimension to introduce multiple thickness mode resonances into one composite design.

Espinosa *et al.* [86] developed a dual frequency 1-3 composite transducer for the purpose of performing the harmonic imaging in the field of medical ultrasound. This 1-3 composite transducer design was comprised of ceramic pillars in three different shapes. By carefully choosing the thickness and different lateral dimensions of the pillars in the composite plate, two main resonance modes, f and $2f$, can be obtained, which was used as the transmission mode frequency and the reception mode frequency, respectively.

The second approach develops materials with enhanced piezoelectric properties to improve the performance of the ultrasound transducer.

Yamada *et al.* [87] proposed a method of designing a broadband ultrasound transducer by giving the piezoelectric plate a temperature gradient in its thickness direction via a controlled temperature based depoling procedure, resulting in a graded piezoelectric stress

constant (e_{33}). As the stress due to the piezoelectric nature of a material can be calculated as the product of electrical field and piezoelectric stress constant, the graded e_{33} distributed along thickness direction could offer improved bandwidth at the fundamental thickness mode. Yamada *et al.* [88] developed another graded piezoelectric material by partially diced a number triangular grooves (kerfs) into one surface of a piezoelectric ceramic plate which were then filled epoxy polymer. The material comprised a monolithic piezoelectric device combined with a piezoelectric composite, where the graded piezoelectric property in the thickness direction was then obtained. The transducer made from this graded piezoelectric material was also shown to have enhanced bandwidth performance when compared with a conventional piezoceramic transducer. However, due to the brittle nature of the piezoceramic material, the vertices between two triangular kerfs could be easily broken. Guo *et al.* [89], [90] presented a similar partial piezoelectric composite design with graded piezoelectric property using the rectangular kerfs, achieving bandwidth improvement when compared to a conventional 1-3 composite device.

When compared to the standard piezoceramic material, Relaxor-based piezocrystal materials, such as PMN-PT, are well known because it has a high value of k_{33} and d_{33}. As the cost of the piezocrystal material continues to decrease due to the improved manufacturing technology, many novel single element and array ultrasound transducers have been developed for different applications.

Cheng *et al.* [91] and Ritter *et al.* [92] investigated the 1-3 composite ultrasound transducer with different volume fraction ranging from 0.4 to 0.8 of PMN-PT, where a thickness coupling coefficient, k_t greater 0.8 was achieved. This compares very

favourably with the k_t of PZT 1-3 composite designs, an example is plotted in Figure 2-7 (a), with a maximum predicted k_t of 0.66. Hence, the PMN-PT 1-3 composite with a higher value of the k_t can result in a better energy conversion efficiency.

Wong *et al*. [93] designed a high frequency, 20 MHz, phased array ultrasound transducer with a PMN-PT single crystal material for high-resolution imaging. This single crystal array exhibited a wider operational bandwidth, when compared with equivalent piezoceramic designs. Zhen *et al.* [94] developed a faceted array inspired by the geodesic dome architecture. By using this design, the issue related to the crystal orientation of the piezocrystal material preventing machining the bulk single-crystal material into a bowl shape without degrading its performance was solved. This shaped piezocrystal material with high piezoelectric performance was used in a focused ultrasound application. Li *et al.* [95], [96] developed a dual-layer 1-3 PMN-PT composite transducer for harmonic ultrasound imaging application. The transducer comprised two active layers made from 1-3 PMN-PT composite with opposite poling direction. These two active layers were bonded in series mechanically and shared common ground at their interface. By using this configuration, two operating modes can be possessed by a single transducer.

The final category for enhancing the performance of a transducer involves employing either electronic or mechanical matching components.

Hossack and Auld [97] reported a novel transducer design with an active piezoelectric matching layer to perform the pulse shaping and thus generate a broadband output signal. The transducer is comprised of two layers of 50% VF 1-3 composites. This transducer

configuration can offer the flexibility of controlling the transfer function of the transducer. By using the Laplace matrix technique, the excitation signal can be determined to produce the desired broad bandwidth output signal.

As for improving the transducer performance by incorporating an electronic matching circuitry, Dziewierz *et al.*[98] developed an in-probe electronics printed circuit board (PCB) for a 2D phased array in order to provide electrical impedance matching between each array element and the associated drive electronics. The experimental results showed a significant sensitivity and bandwidth enhancement can be realised after using such in-probe electrical matching.

To summarize, the techniques reviewed in this Section support the concept that the performance of an ultrasound transducer can be enhanced using a number of popular approaches.

2.4. Introduction of Fractal Geometry

2.4.1. Fractal Basics and Related Application

In the 1970s, the concept of the 'fractal' was first introduced and studied systematically by B. B. Mandelbrot [99], [100]. Nowadays, fractal theory has been developed as one of the most important and active disciplines in Mathematics. The real world can be described more accurately with fractals rather than conventional Euclidean geometries through several characteristics of fractal geometries, including self-similarity, fine structure, irregularity and recursion. The concept of fractals has been employed in a variety of applications such as brain tumour segmentation and detection [101], [102]; signal analysis [103]; antennas design [104], [105], architectural design for the built environment [106], [107]; digital imaging [108] and image compression [109].

A parameter known as the fractal dimension, FD, is defined in Equation (2-14) to describe the complexity level of a fractal geometry as a ratio of the change in detail to the change in scale, where N is the number of self-similar pieces and τ is the scaling factor [99].

$$FD = \log N / \log \tau \tag{2-14}$$

2.4.2. Transducer Design Using Fractal Geometry

In 1993, Alippi *et al.* [110] first presented experimental results which demonstrated the existence of two localised modes and the corresponding surface displacement characteristic for a 1-3 composite plate incorporating a Sierpinski Carpet (SC) microstructure. Figure 2-13 shows the pattern of the SC geometry, where dark grey squares are ceramic pillars and the light grey area is polymer filler. However, the information associated with the operating performance of this fractal composite, such as bandwidth and sensitivity, was not produced at this stage.

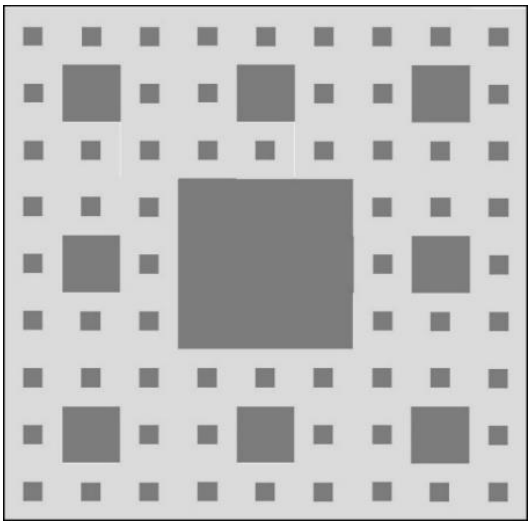

Figure 2-13: Sierpinski Carpet fractal pattern

In 2011, Mulholland *et al.* [6] developed a theoretical model of an ultrasound device with a Sierpinski Gasket (SG). The SG fractal structure is shown in Figure 2-14 (a) and the physical layout of the transducer is shown in Figure 2-14 (b), where $\mathbb{Z}_p$ and $\mathbb{Z}_o$ is the parallel and series electrical load impedance, respectively and V is the excitation source.

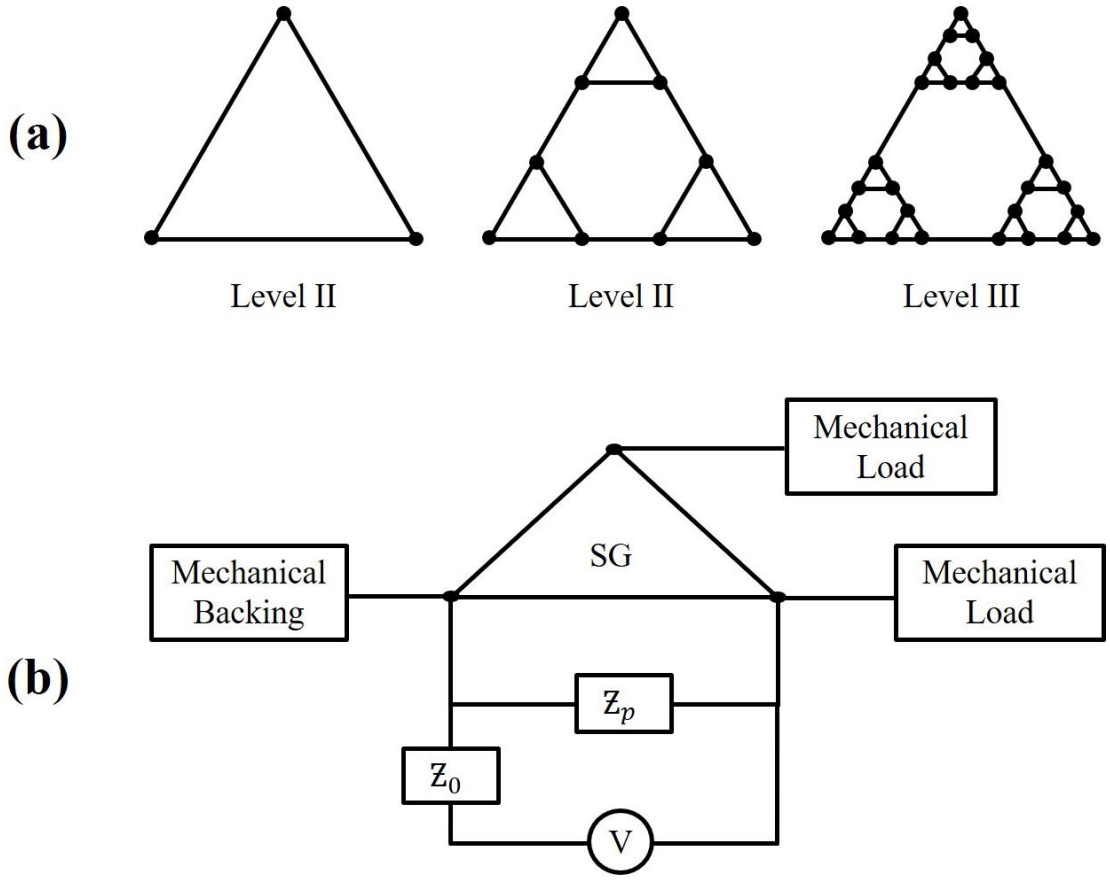

Figure 2-14: (a) SG fractal pattern; (b) Schematic of SG fractal transducer model [6]

Using the renormalization modelling approach, it has been verified that by using the SG pattern, more resonance modes were introduced in the impedance profile due to the complex microstructure pattern and the reception sensitivity was predicted to improve compared to the standard 1-3 composite device. In addition, an FE model also gave the evidence that the poling direction and the material thickness can influence the bandwidth of the SG fractal composite [111].

In 2015, Algehyne *et al.* [112] built a mathematical model of a 1-3 composite with the SG pattern using the renormalization approach, which is shown in Figure 2-15. It was proved

again in his work, that at certain generation levels, the 1-3 SG fractal composite could offer higher sensitivity in both reception and transmission modes.

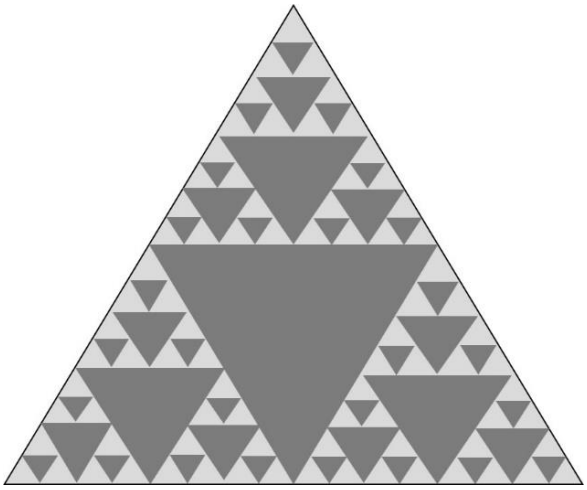

Figure 2-15: 1-3 Composite model with SG fractal pattern, where dark grey triangles are ceramic pillars and light grey triangles are polymer filler, the thickness dimension is vertical (out of the paper)

In 2017, using the similar renormalization modelling approach, Canning *et al.* [113] developed a piezoelectric ultrasound transducer using the SC fractal geometry, shown in Figure 2-13, at fractal generation Level III. By analysing the propagation of ultrasound waves in the structure of this SC fractal piezoelectric ultrasound transducer, it was found out that both transmission and reception bandwidth improvement can be achieved when compared to the standard Euclidean ultrasound transducer design.

Mulholland, Algehyne and Canning's work is constrained to a theoretical analysis, where the renormalization modelling approach provides a fast way of exploring the general insight and global properties of an ultrasound device incorporating a fractal geometry. Another limitation of using the renormalization method is that it can be applied to only

few types of fractal geometry. However, the work described in this thesis is focused on engineering and will investigate FE modelling and fabrication of composite transducers with fractal geometry. The FE modelling approach will enable the flexibility to investigate transducers with an arbitrary fractal geometry and analyse both their global and local propetries, like electrical impedance, transmission response, surface dialation shape and beam profile. Importantly, these characteristics will be validitated experimentally.

In a related transducer field, in order to enhance the sensitivity of an eddy current probe for non-destructive, Chen *et al.* [114] proposed a plannar eddy current probe comprising an excitation coil utilising a Koch curve at fractal generation Level III. The geometry of this Koch curve is described in Figure 2-16. By using this exciting coil pattern, a multi-radius eddy current distribution can be formed on the test object, which can be equivalent to the summation of circular coils with different radii. Therefore, the defect information can be interfered using the eddy current configuration more easily.

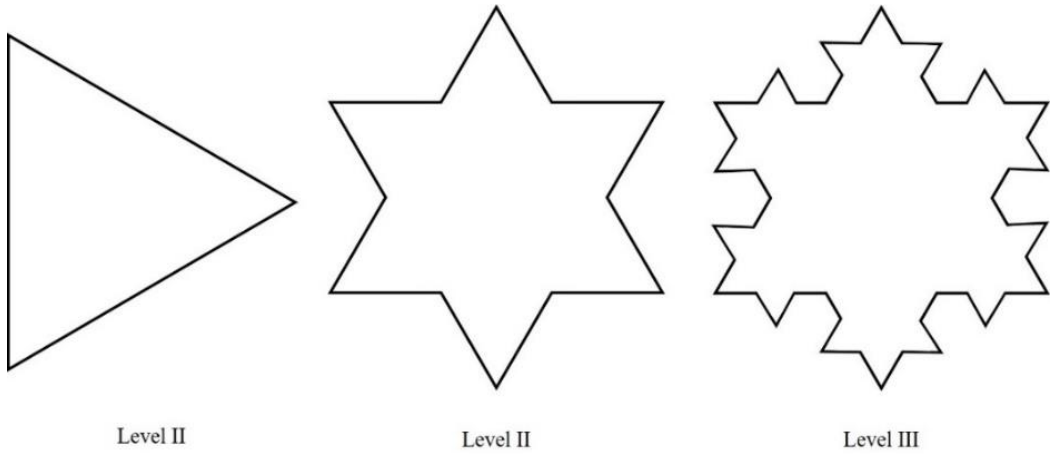

Figure 2-16: Koch curve fractal pattern

To summarise, it is clear that the theory would suggest that by using a fractal geometry, comprising components over multiple length scales, the performance of the transducer can be improved in different aspects. What remains to be done is to investigate whether or not such structures can be designed for manufacture and importantly, if these fabricated structures do outperform current technology. This will form the central theme of this thesis.

CHAPTER III

PIEZOELECTRIC COMPOSITE TRANSDUCER DEVELOPMENT USING SIERPINSKI GASKET FRACTAL GEOMETRY

In this Chapter, a self-similar fractal geometry known as the Sierpinski Gasket (SG), will be adopted as the structure of a composite design in order to explore improvements in the bandwidth of the 1-3 composite configuration transducer. This concept of engineered transducers comprised of multiple length scales has been developed mathematically [4], [5], [6] and these analytical models indicate that by having elements with varying length scales in the piezoelectric transducer design, the device may possess a wider operational bandwidth or a higher sensitivity compared to a conventional device. In addition, it has been shown that devices comprising of triangular pillars, resulting in an absence of parallel faces between elements in a composite design, reduce the inter-pillar resonant activity in the lateral dimension [63]. Therefore, the thickness coupling efficiency can be increased, leading to a potential improvement in the device sensitivity.

Two equivalent 1-3 composites, one with a conventional periodic parallelepiped shaped pillar structure and one with the SG fractal geometry, are designed and compared in this Chapter. The FE analysis package, PZFlex (OnScale Inc, Cupertino, CA), is employed to analyse the behaviour of these two composite designs, in order to provide the proof of concept for this broadband fractal composite design approach. Following the simulation results, a single element transducer, utilizing the proposed SG fractal microstructure, is fabricated using a pillar placement methodology. The performance of the prototyped device is characterized and compared with a conventional 1-3 composite design, as well as with a commercial ultrasound transducer.

To conclude this Chapter, a conventional triangular-cut composite incorporating an electrode pattern of the SG fractal geometry is simulated in order to understand the effect of using a fractal electrode on a piezoelectric composite device, as opposed to the more complicated fabrication associated with the SG fractal microstructure.

The output of this Chapter has been published as a conference paper in the International Ultrasonic Symposium [115] and a journal paper in the IEEE Transactions on Ultrasonics, Ferroelectrics, and Frequency Control [116].

3.1. Sierpinksi Gasket Geometry

As shown in Figure 3-1, the primary shape of the SG fractal geometry is an equilateral triangle, where the fractal configuration at higher generation levels can be achieved by subdividing the entire equilateral triangular pattern recursively into several similar equilateral sub-triangles.

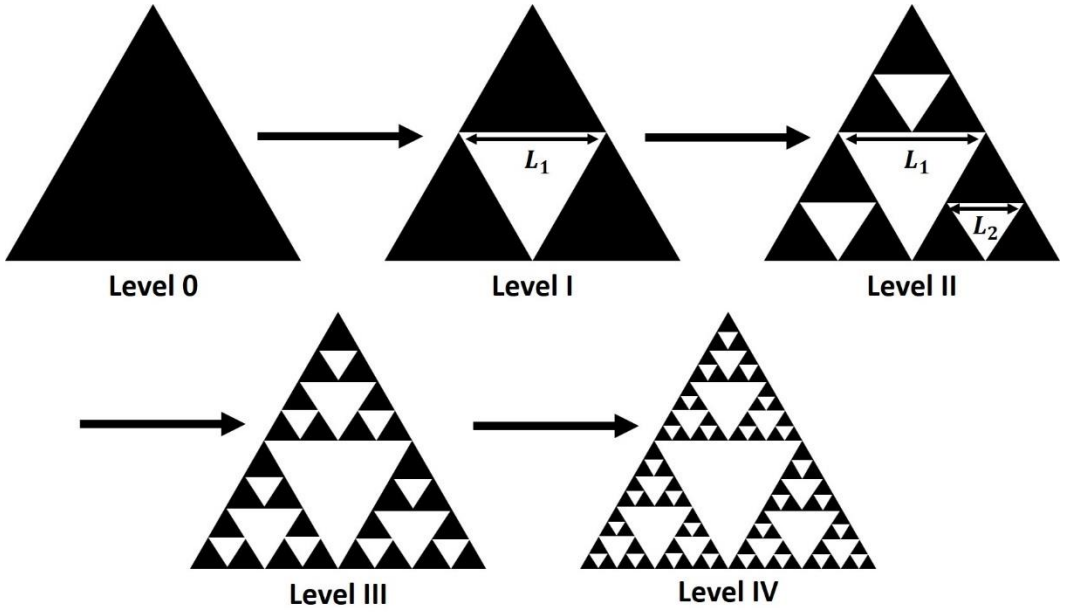

Figure 3-1: The first four fractal generation levels of the SG Fractal Geometry

The lateral width of the sub-triangle at the k_{th} fractal generation level, L_k, can be calculated in terms of the total lateral length of the entire fractal geometry, L, using Equation (3-1).

$$L_k = \frac{L}{2^k} \tag{3-1}$$

3.2. Transducer Finite Element Modelling

3.2.1. Piezoelectric Composite Design Using SG Fractal Geometry

Initially, how the fractal generation level of a SG fractal geometry configuration would influence the transmit performance of the composite device was investigated. In order to explore the problem space, several 3D FE models of the unmatched SG fractal composite microstructure from fractal generation Level III to Level VI and their corresponding equivalent conventional 1-3 composite designs were simulated using PZFlex with a water load. The active and passive phase materials are PZT-5H ceramic (Meggitt A/S, Kvistgard, Denmark) and hardset polymer (Robnor Resin Ltd, UK), respectively. For each SG fractal model, the lateral length of the smallest triangular was kept as 1 mm. In terms of each conventional 1-3 composite plate model, the pillar width was maintained the same at 1 mm, whilst the ceramic volume fraction (VF) was varied in order to keep it the same as the SG fractal composite design at different fractal generation levels, aiming to provide a fair comparison between the two designs in terms of the sensitivity level. The VF of the SG fractal composites from generation Level III to Level VI and their equivalent conventional 1-3 composites are 57.8 %, 68.4 %, 76.3 % and 82.2 %, respectively. To determine the composite thickness for all of these models, the maximum pillar aspect ratio (MPAR) concept reported by Hayward and Bennett [117] for 1-3 configurations was utilized to ensure a high electromechanical coupling efficiency in the thickness resonance mode for VF above 50%. Accordingly, in the 1-3 composite case, the MPAR should be

limited to 0.39, resulting in a 2.6 mm layer thickness and this thickness has been used in each model for a fair comparison between the SG fractal composite and the conventional 1-3 composite.

The transmitting voltage response (TVR) spectra, calculated using Equation (3-2), of these SG composites from fractal generation Level III to Level VI were simulated and compared to the equivalent conventional composite designs – for each case the results are shown in Figure 3-2 and Table 3-1.

$$TVR = 20\,log(Pressure/V_{in}) \tag{3-2}$$

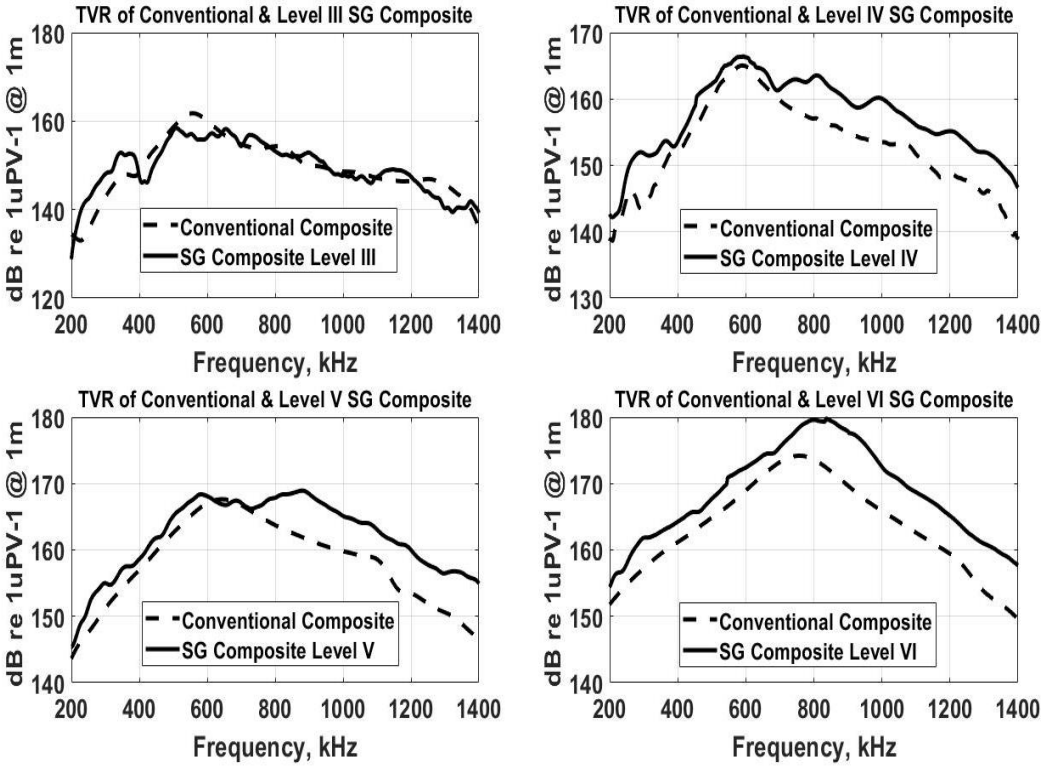

Figure 3-2: Simulated TVR of the conventional and the SG composite (Level III to Level VI)

Table 3-1: Simulated TVR result summary for SG composites from Level III to Level VI and equivalent conventional composites

Fractal Generation Level	VF	SG Composite		Conventional Composite	
		Bandwidth	Sensitivity	Bandwidth	Sensitivity
Level III	57.8 %	47.1 %	158.5 dB	35.2 %	161.8 dB
Level IV	68.4 %	71.4 %	166.5 dB	40.1 %	165.0 dB
Level V	76.3 %	82.8 %	168.4 dB	62.7 %	167.6 dB
Level VI	82.2 %	46.5 %	179.6 dB	45.0 %	174.2 dB

It can be seen that the SG composite at the third fractal generation level behaved approximately the same as the conventional composite. However, as the fractal generation level increases beyond three, the SG composite starts to show improved fractional bandwidth when compared to the conventional composite design. For example, at fractal generation level IV, the -6 dB bandwidth of the unmatched SG fractal composite plate is 71.4 % compared to 40.1 % for the conventional composite plate.

The effective thickness-mode electromechanical coupling coefficient, k_t, is a well understood figure of merit for transducer performance, which was introduced in Section 2.2.2.2, and can be calculated as a function of separation of the electrical resonant frequency, f_{ele}, and the mechanical resonance, f_{mech}, of the device using Equation (2-12).

The k_t values of the four SG fractal composites and their equivalent conventional 1-3 composites were determined using the FE derived impedance spectra, these data are

plotted in Figure 3-3. In order to make further comparison, the k_t of the conventional 1-3 composites across the VF range was determined using the Smith-Auld model [57], again these data are plotted in Figure 3-3, where it can be seen that the k_t simulated with the Smith-Auld model matches with the results achieved by the FE model for the conventional composites. In addition, the general behaviour of 1-3 connectivity composites can be extracted, where a maximum in k_t is typically observed in the 50-65 % VF range. The motivation in the design of the 1-3 composite is to attain a maximal k_t, where in theory this is limited by the k_{33} of the piezoelectric material.

Considering the data for the SG composite devices shown in Figure 3-3, k_t is observed to exhibit different behaviour to that of the conventional 1-3 composite, attaining a maximum at a higher VF than would typically be observed in a 1-3 connectivity composite. Furthermore, it can be clearly seen from Figure 3-3 that the k_t of the SG composites is always higher than the equivalent conventional 1-3 composites across all the VF in this study. Moreover, k_t of the Level V SG composite is beyond the k_{33} of PZT-5H ceramic, typically 0.70. By considering Equation (2-12), it can be seen that the frequency separation of the electrical resonance and mechanical resonance governs the magnitude of k_t. In the SG composite device, there are number of coupled modes that act in concert at the thickness mode, thereby extending the frequency separation of the two resonances resulting in a k_t for the device beyond the theoretical maximum.

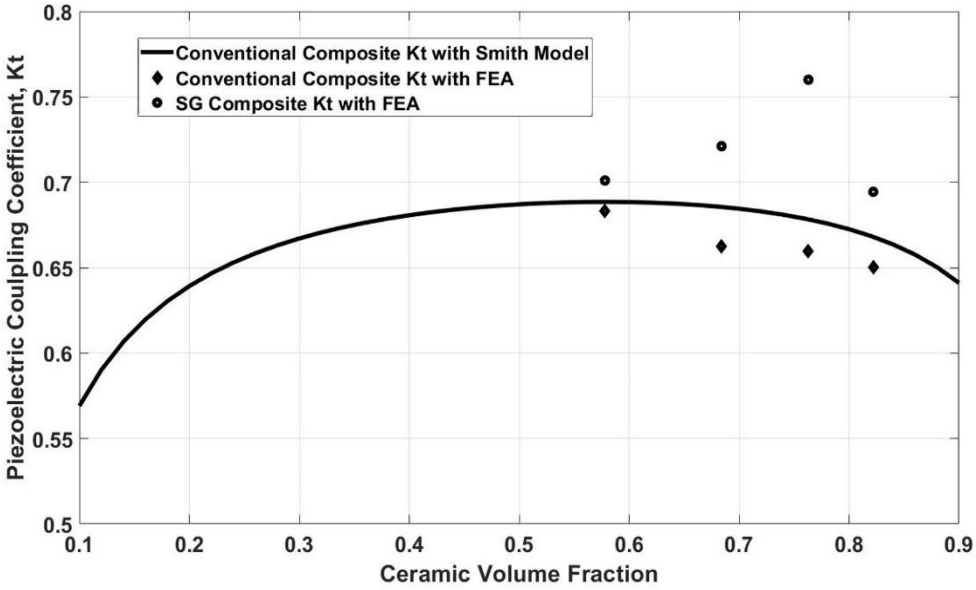

Figure 3-3: Simulated k_t for SG and conventional 1-3 composite with different ceramic volume fraction

Considering the difficulties of the fabrication process, the Level IV SG fractal composite is considered as a good initial choice for studying and fabricating, which will undergo further analysis and its performance will be compared to a conventional 1-3 composite of the same VF in the subsequent Section of this Chapter. While it is recognized that a VF of 68.4 % is not the optimized choice for the conventional 1-3 composite in imaging applications, the device still gives a reasonable performance before the k_t further decreases with increased VF.

3.2.2. SG Fractal Composite at Fractal Generation Level IV

3.2.2.1. Electrical Impedance Profile

Figure 3-4 (a) illustrates the Level IV SG fractal composite design, where the active phase of this SG composite is comprised of equilateral triangular ceramic pillars with different lateral length scales. Figure 3-4 (b) shows an equivalent conventional parallelepiped 1-3 composite design. Consistency is maintained between the two composite designs in five aspects by ensuring each device has the same fundamental design parameters.

1) PZT-5H ceramic (Meggitt A/S, Kvistgard, Denmark) and hardset polymer (Robnor Resin Ltd, UK) are chosen to be the active and passive phase, respectively.
2) The lateral length of the smallest triangular pillar at the 4^{th} fractal generation level in the SG composite, L_4 as defined in Equation (3-1), is chosen to be 1 mm and this same pillar width value is assigned to the conventional composite design. The kerf width of the conventional composite is 0.2 mm. The thickness of both devices is set to be 2.6 mm for the purpose of minimizing the negative effect caused by the pillar vibrating in the lateral direction.
3) VF of both composite designs is 68.4 % because of the fixed configuration layout of the SG fractal geometry.
4) The active aperture area for both composite designs is approximately the same, which is 111 mm^2.
5) The same matching layer arrangement will be incorporated into both composite designs.

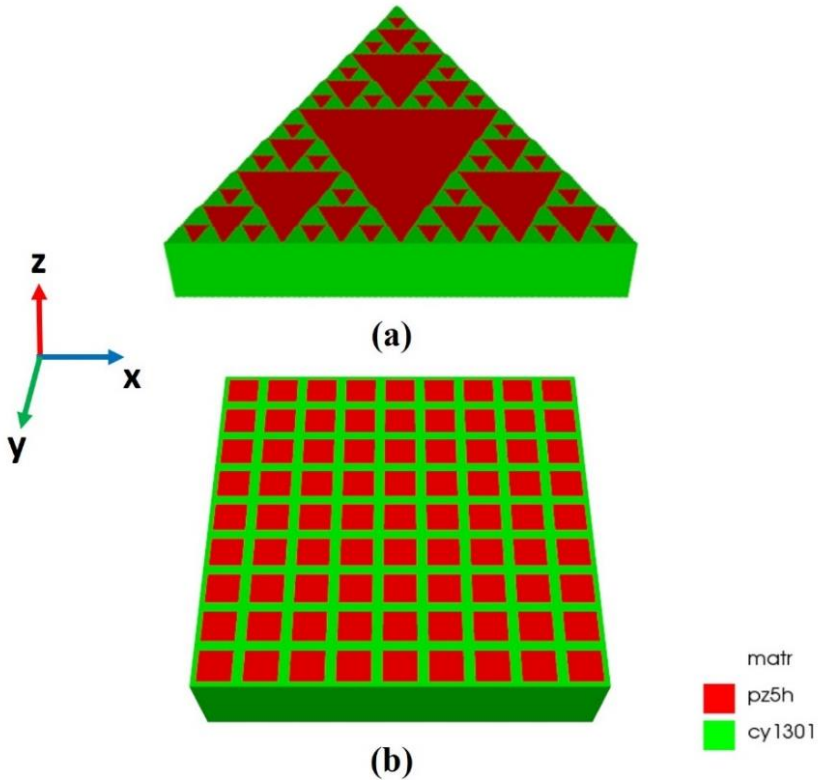

Figure 3-4: FE composite model: (a) Level IV SG fractal composite; (b) conventional 1-3 composite

The electrical impedance of the Level IV SG composite and conventional composite are simulated in a water load without a matching layer. The FE derived electrical impedance magnitude spectra of both composites is plotted in Figure 3-5. The SG fractal composite and the conventional composite exhibit electrical impedance minima at 580 kHz and 575 kHz, respectively and impedance maxima at 837 kHz and 751 kHz, respectively. The electrical resonant and mechanical resonant frequencies of each composite were used to calculate the effective electromechanical coupling coefficient, k_t. Compared to the conventional design, the SG fractal composite achieved a larger value of k_t, which is 0.72 against 0.65 for the conventional composite, as illustrated in Figure 3-5. Therefore, a

better energy conversion and improved bandwidth may be realized by the SG fractal design.

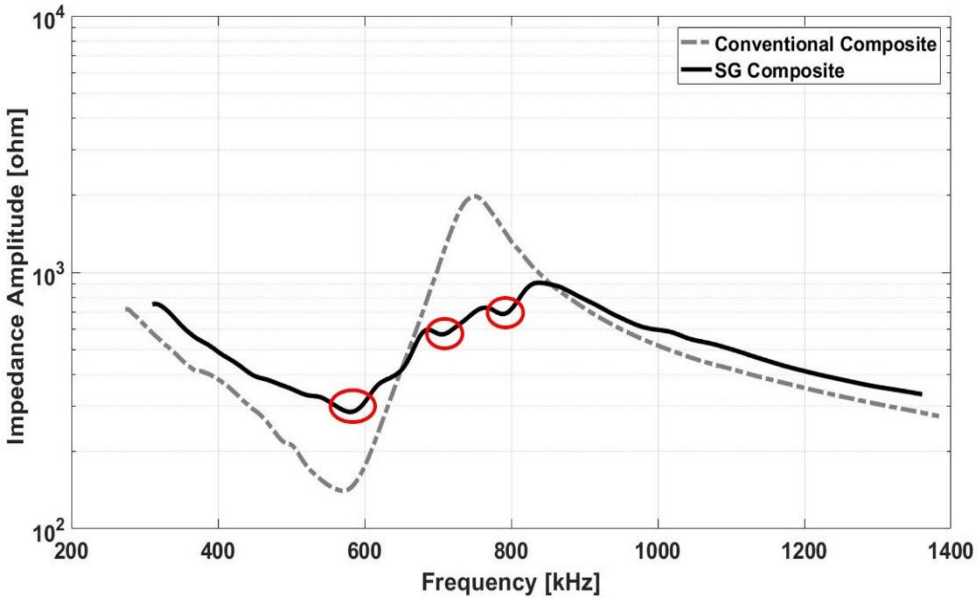

Figure 3-5: FE derived electrical impedance magnitude spectrum of the SG and the conventional composite operating into a water load

3.2.2.2. Vibration Modal Analysis

It can be seen in Figure 3-5 that a multi-modal characteristic is exhibited in the SG fractal design due to its varying pillar length scale. Three key modes are identified in the SG fractal design at 580.0 kHz, 705.4 kHz and 790.0 kHz, which are marked with red circles in Figure 3-5. In order to explore the resonance behaviour of the SG fractal composite in detail, the displacement mode shape in the thickness direction was investigated at each frequency. All thickness displacement data plotted in Figure 3-6 were normalized to the maximum value of the first resonant mode shown in Figure 3-6 (a), for the purpose of comparing the mode strength.

The surface dilation quality factor Q_{dil}, which is used for describing the uniformity of the surface displacement as described in Section 2.2.2.1, was calculated in the thickness direction using Equation (2-11) for each of the three resonance frequencies shown in Figure 3-6. The calculated result is presented in Table 3-2.

Table 3-2: Calculated Q_{dil} at each resonance frequencies

Resonance Frequency	**580.0 kHz**	**705.4 kHz**	**790.0 kHz**
$\boldsymbol{Q_{dil}}$	**0.72**	**0.21**	**0.20**

From Figure 3-6 and Table 3-2, the strong thickness mode behaviour in the pillars associated with the 2nd, 3rd and 4th fractal generation levels at 580 kHz has produced the highest Q_{dil}, which is 0.72. For the resonances at 705.4 kHz and 790 kHz, the lateral resonances from the 1st and 2nd fractal generation levels dominate the vibrational response and the corresponding Q_{dil} figures are 0.21 and 0.20, respectively. These dilation quality factors are lower than a conventional 1-3 composite device, which is 0.95 for the equivalent device used in this study, due to the antiphase resonance behaviour present in the triangular pillars with large pillar aspect ratio in fractal generation Level I and II, although the main thickness mode resonance vibrational response for the SG device is still considered to be sufficiently high for acceptable operational performance. It is worth noting that the design premise of the fractal geometry composite is to couple different resonance modes and hence, the design philosophy is not directly comparable to the well-known conventional 1-3 composite theory.

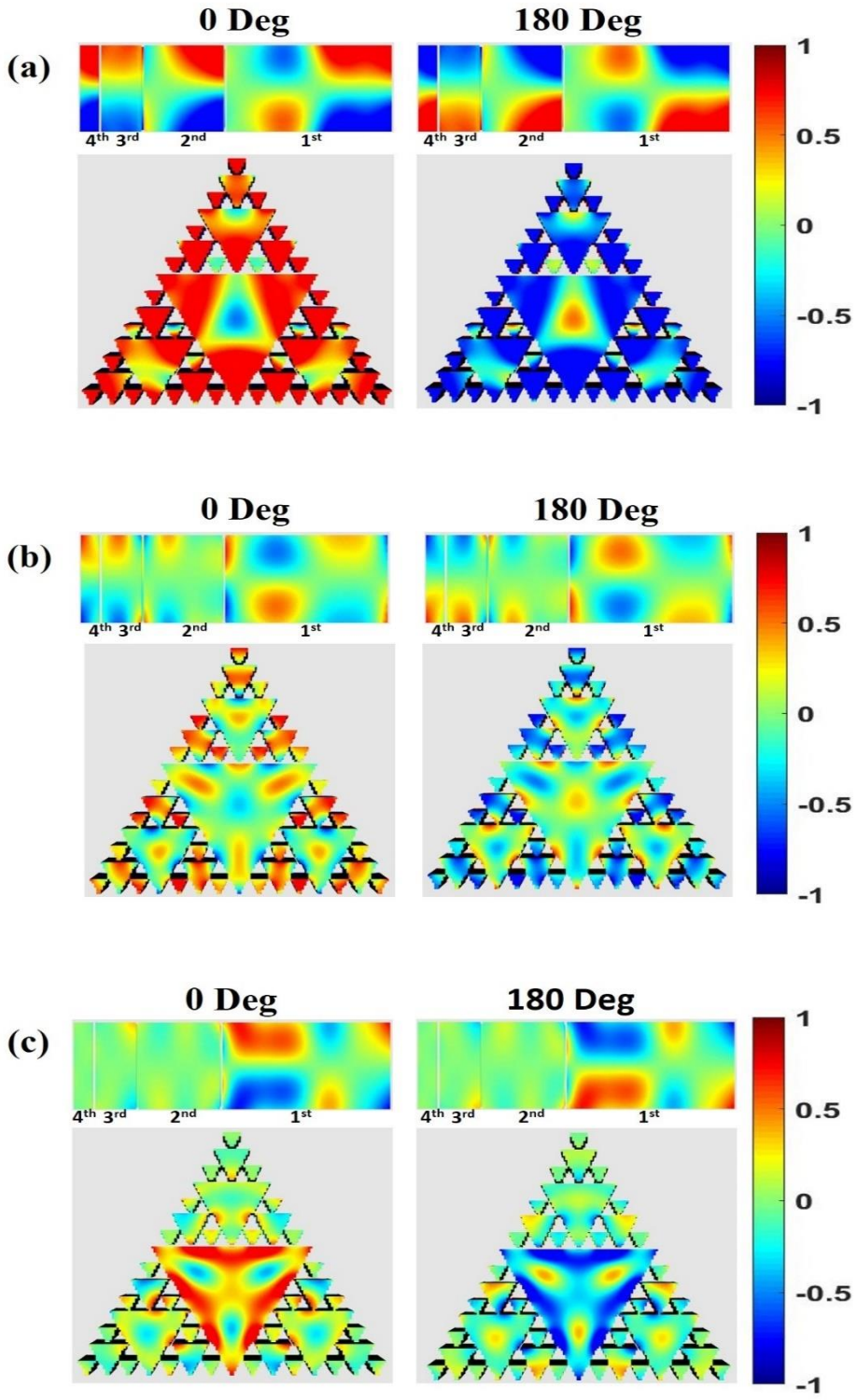

Figure 3-6: SG composite displacement mode shape in thickness direction at: (a) 580.0 kHz; (b) 705.4 kHz; (c) 790.0 kHz

3.2.2.3. Matching Layer Design

In order to provide a good impedance match between the transducer and the liquid load, FE models are constructed, where both devices are matched to a water load via a dual matching layer scheme. For the purpose of maximising the output signal strength and to avoid obscuring the distinct resonances of the SG fractal structure, the backing layer was not incorporated into the transducer designs in this Chapter. A schematic of the transducer arrangement is depicted in Figure 3-7.

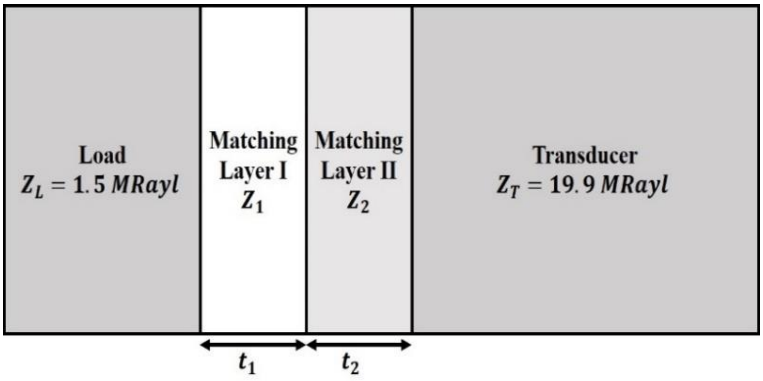

Figure 3-7: Schematic of an ultrasound transducer with a dual matching layer

Z_L is the acoustic impedance of the load, which is 1.5 MRayl for the water and Z_T is the acoustic impedance of the transducer itself, which is calculated as 19.9 MRayl using the Smith-Auld model [57] according to the VF of the composite. The ideal acoustic impedance of each matching layer, Z_1 and Z_2, can be calculated using Equations (3-3) and (3-4) [118].

$$Z_1 = Z_T^{\frac{1}{7}} \times Z_L^{\frac{6}{7}} \tag{3-3}$$

$$Z_2 = Z_T^{\frac{4}{7}} \times Z_L^{\frac{3}{7}} \tag{3-4}$$

The calculated values for Z_1 and Z_2 for a theoretically optimal matching layer are 2.2 MRayl and 6.6 MRayl, respectively. Consequently, the CY221/HY956EN medium set polymer (Robnor Resin Ltd, UK) with an acoustic impedance of 2.68 MRayl is chosen as the material for Matching Layer I. The CY1301/HY1300 hard setting polymer (Robnor Resin Ltd, UK) filled with 3 μm alumina powder using 70 % weight fraction was used for Matching Layer II, which has an acoustic impedance of 6.96 MRayl [119].

Once the acoustic impedance of each layer is selected, layer thicknesses can be determined using the transfer matrix method via Equation (3-5) and (3-6) [120],

$$tan\,\theta_1 = \alpha^{\frac{1}{2}}\left[\frac{(Z_1 - \beta Z_2)}{\beta Z_1 - Z_2}\right]^{-\frac{1}{2}} \tag{3-5}$$

$$tan\,\theta_2 = \left[\frac{\alpha(Z_1 - \beta Z_2)}{\beta Z_1 - Z_2}\right]^{\frac{1}{2}} \tag{3-6}$$

where θ_n is the phase shift in each matching layer as determined by the wavelength λ_n and the thickness t_n of each matching layer, which is given in the Equation (3-7) and the coefficients, α and β can be calculated using Equations (3-8) and (3-9), respectively.

$$\theta_n = 2\pi \frac{t_n}{\lambda_n} \tag{3-7}$$

$$\alpha = \frac{Z_T - Z_L}{\frac{Z_1 Z_T}{Z_2} - \frac{Z_2 Z_L}{Z_1}} \tag{3-8}$$

$$\beta = \frac{Z_T Z_L}{Z_1 Z_2} \tag{3-9}$$

By using these materials and equations at the transducers' operating frequency, 580.0 kHz, the resulting thickness of the first matching layer is 580 μm and 1093 μm for the second matching layer.

The TVR of the SG fractal composite with and without a matching layer was simulated using the FE modelling method and the result is shown in Figure 3-8. It can be seen that after the dual matching layer designed in this Section was applied, the sensitivity of the SG fractal composite was increased by 2 dB.

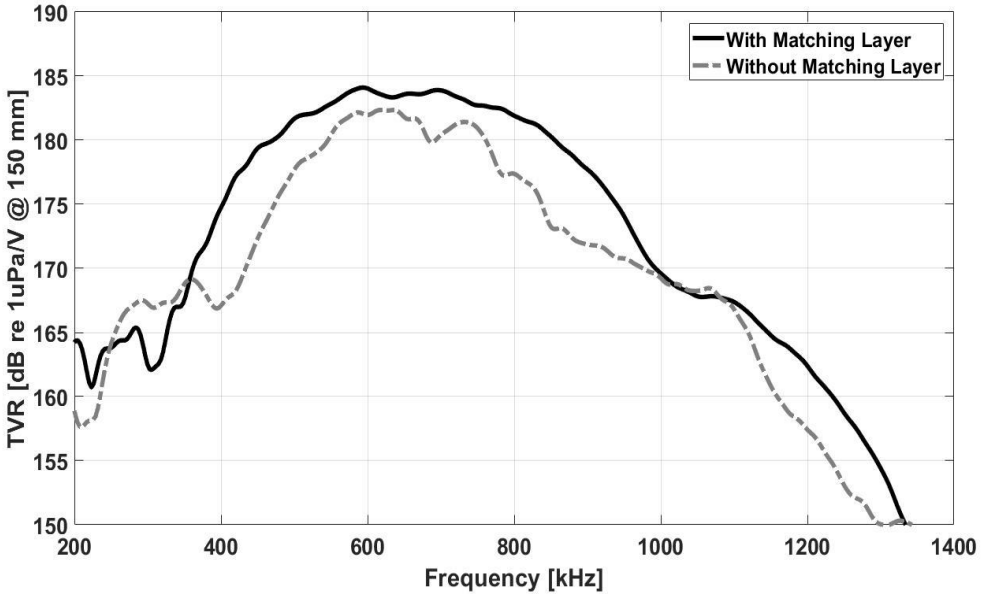

Figure 3-8: Simulated TVR of the SG composite with and without matching layer

3.2.3. Simulation of Single Element SG Fractal Composite Transducer

3.2.3.1. Transmission, Reception and Pulse-Echo Response Modelling

The performance of the two equivalent composite devices, each incorporating a dual matching layer designed in Section 3.2.2, was then assessed by considering the transmitting voltage response (TVR) defined in Equation (3-2); the open circuit voltage response (OCV), can be calculated via Equation (3-10); and the pulse-echo response.

$$OCV = 20\,log((V_{out}/V_{in})/(Pressure/V_{in})) \quad (3\text{-}10)$$

FE models are constructed to simulate the operation of both devices when matched to a water load via a dual matching layer scheme. The predicted TVR, OCV and far-field pulse-echo response are shown in Figure 3-9, Figure 3-10 and Figure 3-11, respectively.

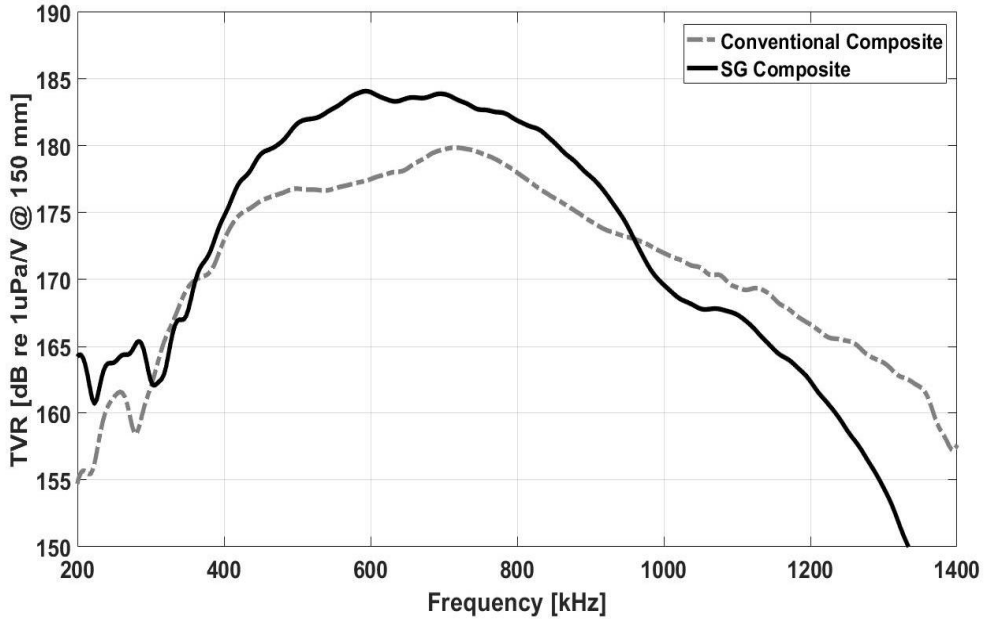

Figure 3-9: Simulated TVR spectrum of the SG and the conventional composite ultrasonic transducers

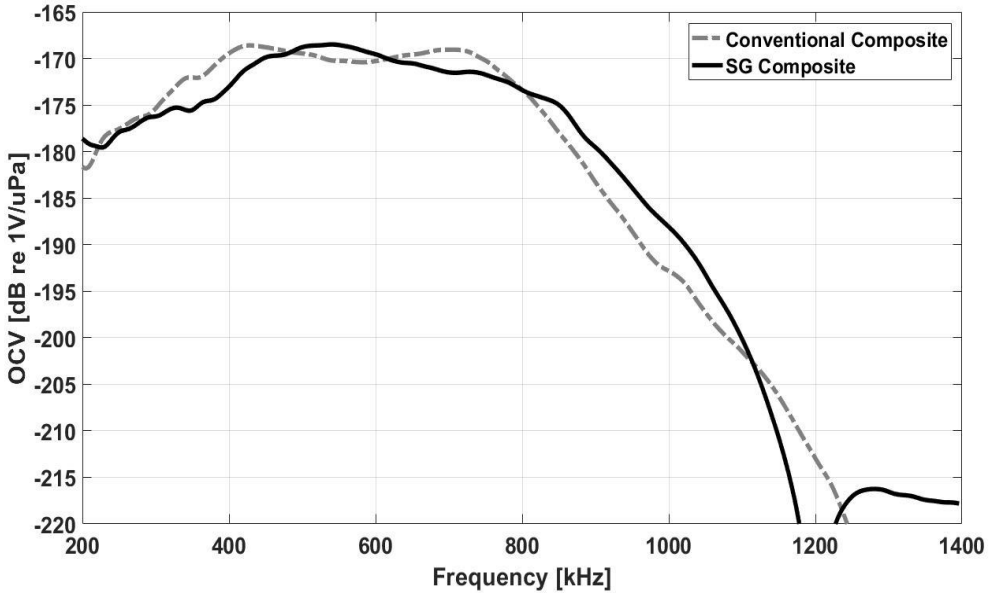

Figure 3-10: Simulated OCV spectrum of the SG and the conventional composite ultrasonic transducers

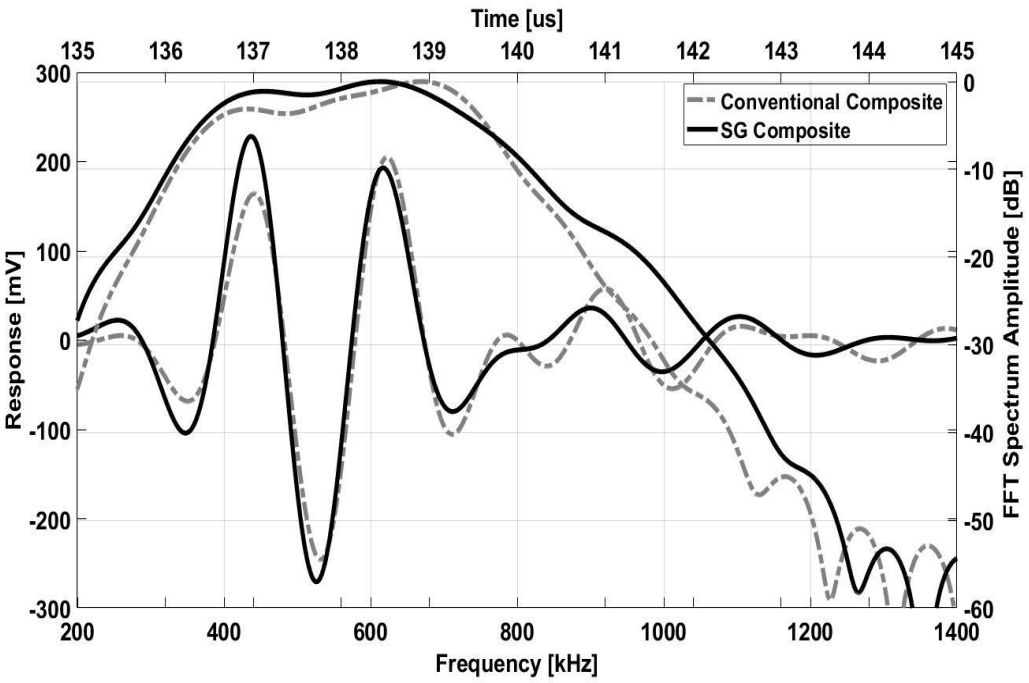

Figure 3-11: Simulated pulse-echo responses of the SG and the conventional composite ultrasonic transducers

The peak gain and -6 dB operational bandwidth for both devices in one-way transmission and reception mode and two-way pulse-echo model are listed in Table 3-3. It can be seen that by using the SG fractal geometry as the structure of a piezoelectric composite transducer design, both operational bandwidth and sensitivity level are enhanced. In transmission mode, a 8.8 % bandwidth improvement and a 4.2 dB sensitivity increment were achieved. In reception mode, although the peak gain of the OCV of the SG fractal device and conventional device are approximately the same, the bandwidth was enhanced by 5.4 % when compared to the conventional device. Lastly, in the two-way pulse-echo mode, the bandwidth and signal strength improvement are 12.1 % and 10.7 % for the SG fractal design, when compared to the conventional composite design.

Table 3-3: Simulated pules-echo, transmission and reception results

	SG Composite	Conventional Composite
Transmission Bandwidth (%)	76.9 %	70.8 %
TVR Peak Gain (dB)	184.1 dB	179.9 dB
Reception Bandwidth (%)	85.2 %	80.8 %
OCV Peak Gain (dB)	-168.5 dB	-168.6 dB
Pulse-Echo Bandwidth (%)	66.7 %	59.5 %
Pulse-Echo Peak-to-Peak Voltage (mV)	498.9 mV	450.8 mV

3.2.3.2. Beam Profile Modelling

The beam profile of the SG fractal and the conventional composite in the y-z plane at their rotating centre axis, indicated with the red dash line in Figure 3-12 (a) and (b), was simulated using the Huygens-Fresnel principle at their electrical resonant frequencies, which are 580 kHz and 575 kHz, respectively. It can be seen from the Figure 3-12 (a) and (b) that the near-far-field point of the SG fractal and the conventional composite is 9.9 mm and 15.6 mm, respectively according to their different geometry. The SG fractal composite also has a tighter focal zone area, when compared to the conventional composite design, where the -3dB focal zone length is 26.1 mm against 45.7 mm, respectively.

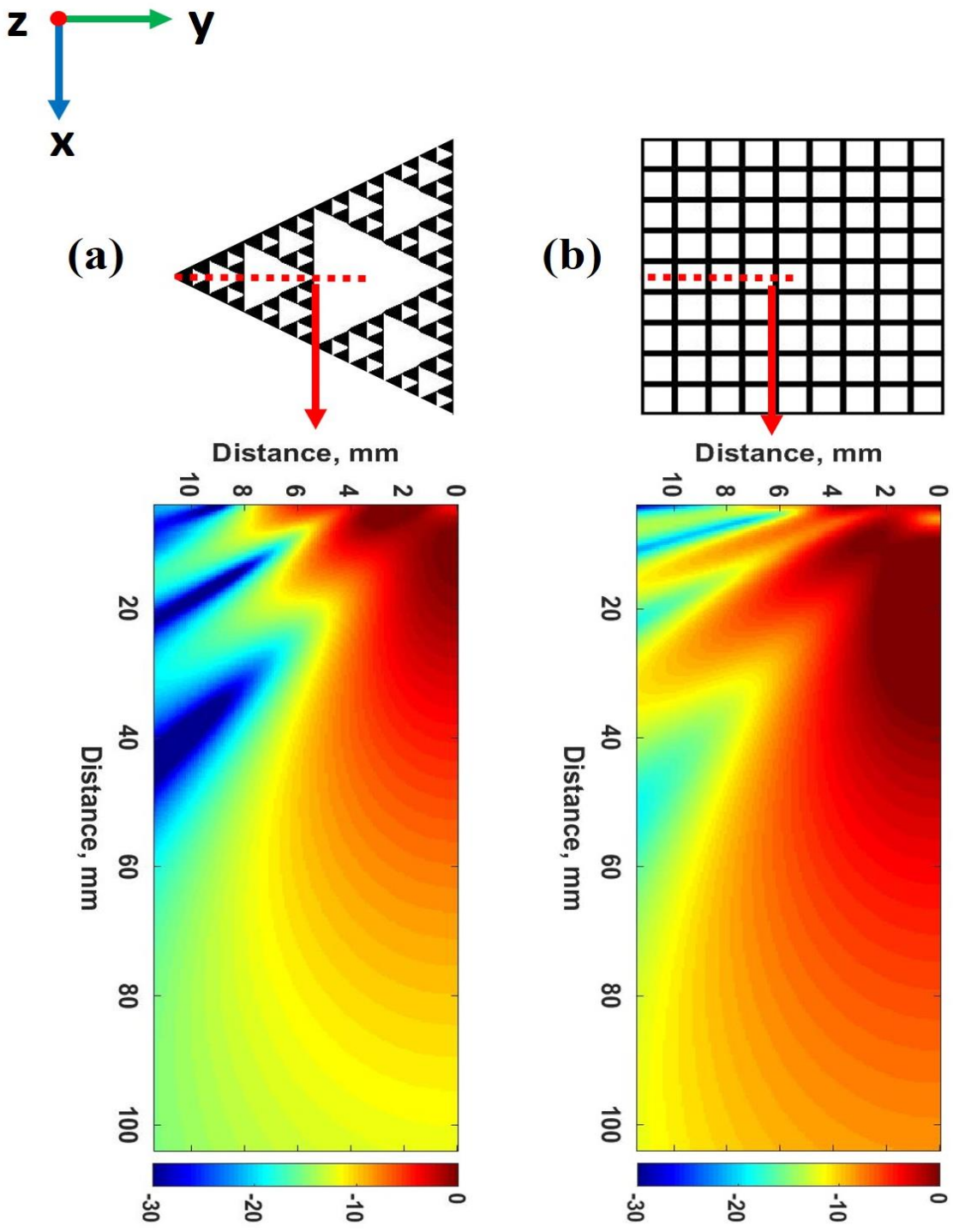

Figure 3-12: Beam profile of: (a) SG composite; (b) Conventional composite

In order to evaluate and compare the side lobe level of the two composite designs, the directivity function of both composites at their far field (a distance of 50 mm from the transducer front face has been selected) is plotted in Figure 3-13. The side lobes of the SG fractal composite and conventional composite in the far field are -17 dB and -12 dB, respectively, where a 5 dB side lobe reduction is achieved by incorporating the SG fractal composite microstructure.

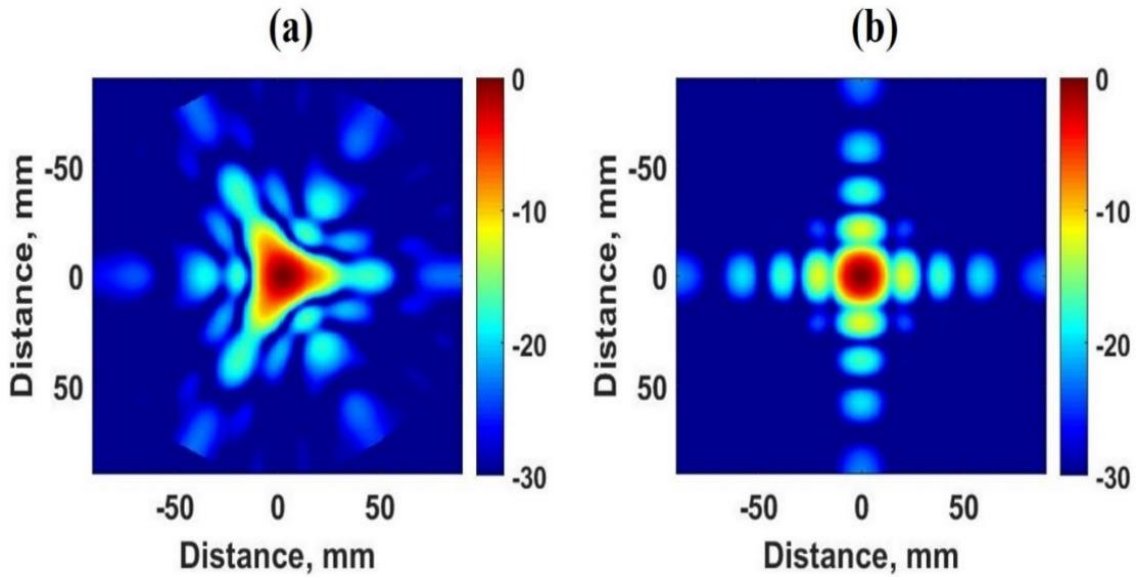

Figure 3-13: Directivity function at far field of: (a) SG composite;(b) Conventional composite

3.3. Single Element SG Fractal Composite Transducer Fabrication

Based on the positive simulation results in Section 3.2, an initial prototype SG fractal composite transducer at fractal generation level IV was manufactured. The manufacturing process of this fractal composite involved a 3D printing technique to produce a mould, followed by a pillar placement methodology, which is described in four steps.

1) The equilateral triangular ceramic pillars at different fractal generation levels were prepared by dicing (MicroACE Series 3 Dicing Machine, Loadpoint, UK) commercial PZT-5H ceramic plates (Meggitt A/S, Kvistgard, Denmark) into appropriate geometries, as shown in Figure 3-14 (a). The lateral dimension of these equilateral triangular ceramic pillars from level I to level IV is 8 mm, 4 mm, 2 mm and 1 mm, respectively.
2) 3D printing technique (Pico Plus 27, ASIGA, USA) was used to manufacture a mould to represent the negative of the SG fractal geometry, which is shown in Figure 3-14 (b), for the function of holding the ceramic pillars in position.
3) The ceramic pillars were placed in the mould, shown in Figure 3-14 (c) and filled with CY1301/HY1300 hardset epoxy polymer (Robnor Resin Ltd, UK), as shown Figure 3-14 (d).
4) Once the polymer filler was fully cured, the mould was machined off and the composite plate was lapped down to the desired thickness, 2.6 mm. The prototype

of this SG fractal composite is shown in Figure 3-14 (e) and is the first manufactured piezoelectric device based on fractal theory.

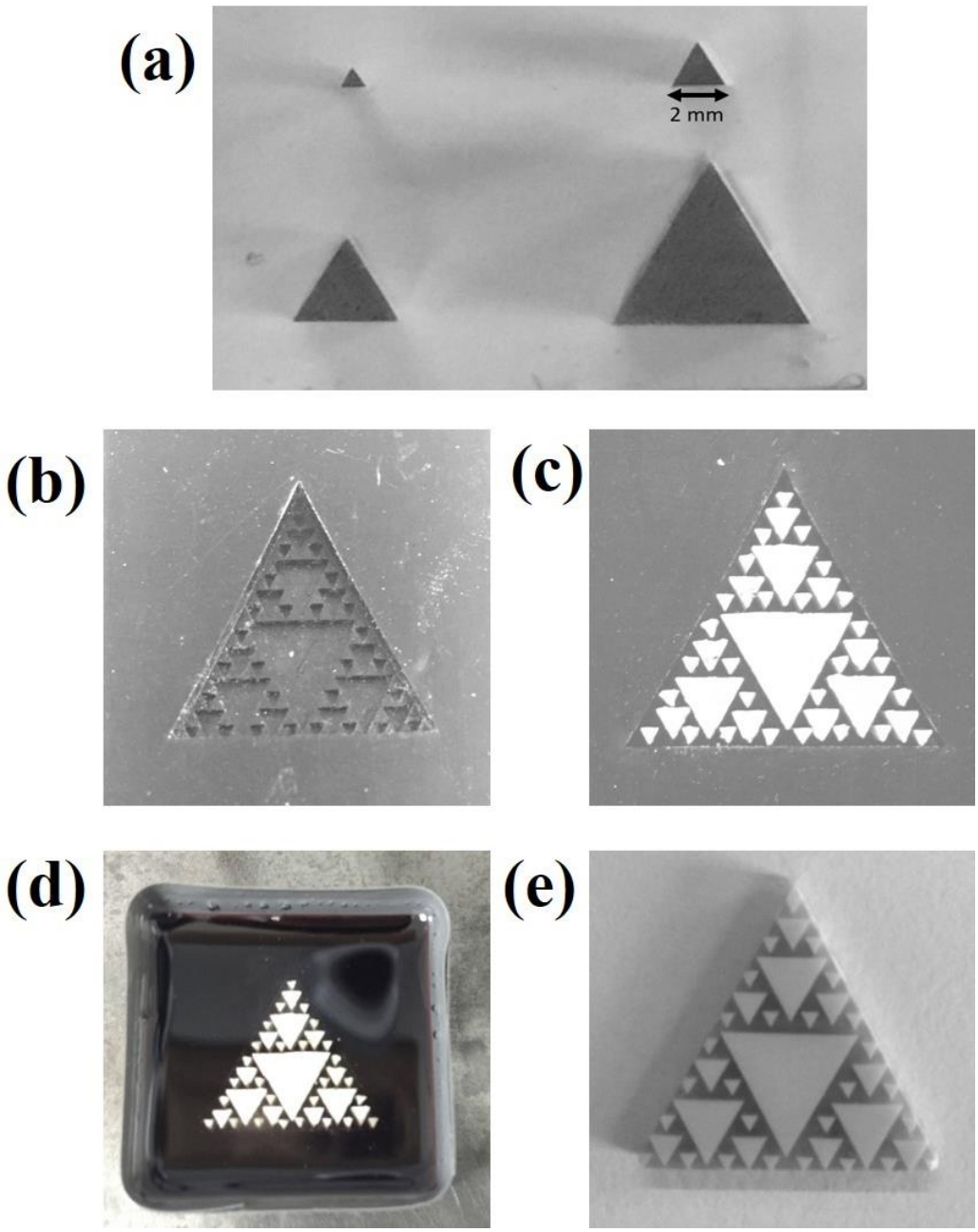

Figure 3-14: SG fractal composite fabrication process: (a) individual cut ceramic pillars with different sizes; (b) 3D printed mould; (c) ceramic pillars are placed in the mould; (d) the mould is filled with polymer; (e) the surplus mould is machined off.

An equivalent conventional parallelepiped 1-3 composite was also fabricated using the traditional ‘dice-and-fill’ technique, in order to compare performance. For each device a dual matching layer was employed, the design of which is described in Section 3.2.2.3. Finally, each device was secured into a water proof housing. Figure 3-15 shows a photograph of the complete SG fractal piezoelectric composite transducer (Left) and an equivalent conventional composite (Right) together with a £1 coin (Middle) which has a diameter of 25 mm.

Figure 3-15: SG fractal (Left) & conventional composite (Right) ultrasonic transducer

3.4. Experimental Validation of Single Element SG Fractal Composite Transducer

The performance of the manufactured SG fractal composite transducer was characterized experimentally in three different modes: one-way transmission (TVR), one-way reception (OCV) and two-way pulse-echo. The measured TVR, OCV and the pulse-echo response

of the SG fractal composite device are compared with the equivalent conventional composite design and an unfocused commercial ultrasound transducer (A301 S, Panametrics, USA). The specifications of the three devices are stated in Table 3-4.

Table 3-4: Transducer Specification

	Pulse-Echo Centre Frequency	**Active Aperture Area**
SG Fractal Composite Transducer	596 kHz	131.9 mm^2
Conventional Composite Transducer	587 kHz	123.2 mm^2
Panametrics Commercial Transducer	547 kHz	615.7 mm^2

It should be noticed that the commercial device has a much larger active area compared with the two fabricated devices: this significant active area difference will be taken into account in the experimental results comparison between these three devices.

3.4.1. Electrical Impedance Response of Fabricated Devices

The electrical impedance responses of the fabricated devices with matching layers were measured in air and they correlated well with the simulation results, as shown in Figure 3-16. The k_t were measured as 0.58 and 0.54 for the SG fractal and conventional composite, respectively.

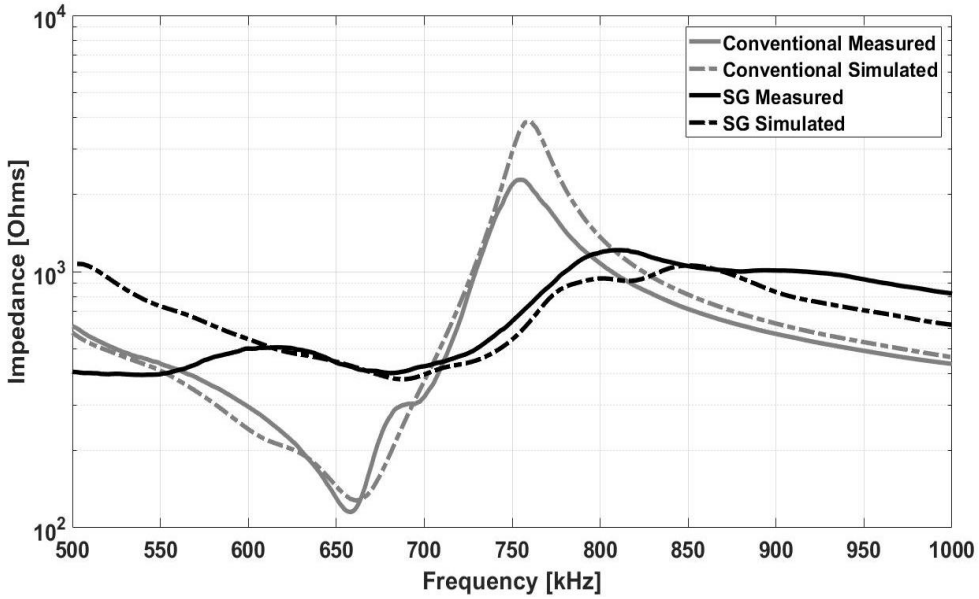

Figure 3-16: Simulated and measured electrical impedance

3.4.2. Transmission Response Characterisation

For characterizing the performance of the devices in transmission mode, the TVR of these three devices was measured experimentally. A function generator (33210A, KEYSIGHT, USA) was used to excite each testing transducer with a 20-cycle tone burst sine signal and the frequency of the tone burst signal varied from 300 kHz to 1500 kHz with a step of 5 kHz. A calibrated hydrophone (IP-124, GEC Marconi Ltd, UK), which has a flat frequency response from 10 kHz to 50 MHz and reception sensitivity of 50 nV/Pa [121], is located in the far field of the transducer (150 mm away from the transducer front face) for capturing the transmitted signal. The experimental setup for measuring the TVR is shown in Figure 3-17. The input and received signal were displayed using an oscilloscope in the time domain. The TVR in frequency domain was obtained using Fast Fourier transform (FFT) and Equation (3-2).

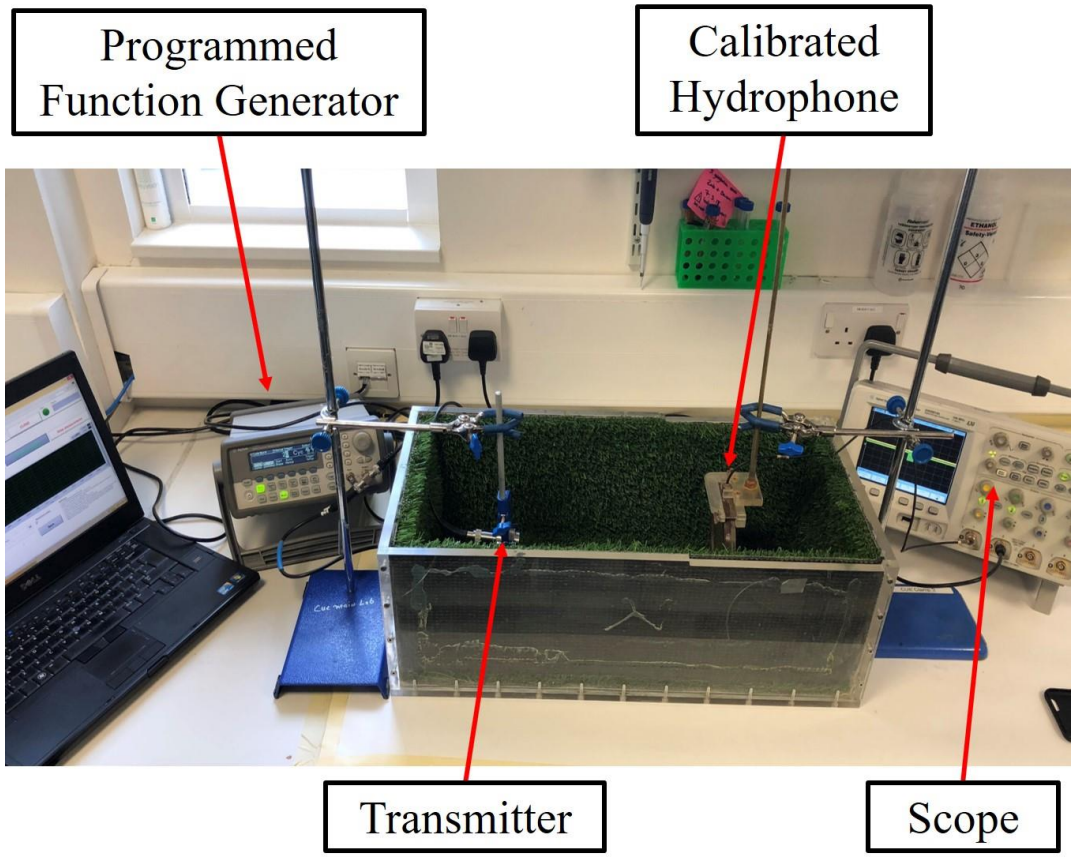

Figure 3-17: TVR measurement experimental setup

The TVR spectra of the three devices are shown in Figure 3-18. The -6 dB transmitting operational bandwidth of these devices is calculated as 64.0 % for the SG fractal device, 50.3 % for the equivalent conventional composite design and 31.2 % for commercial transducer. This equates to a 27.2 % and 105.1 % bandwidth improvement by the SG fractal device. In terms of the sensitivity level, the peak gain of the SG fractal device is 3.8 dB higher than the conventional composite design. However, the peak gain of the SG fractal device is 1.9 dB lower when compared to the commercial transducer, which is due to the significant difference in active aperture areas of each device.

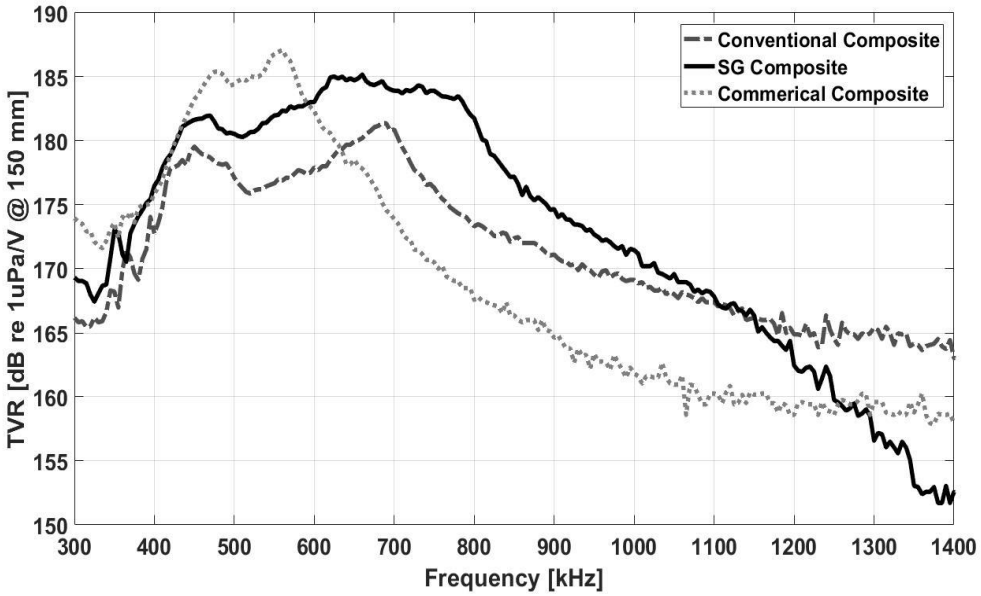

Figure 3-18: Measured TVR spectrum of the three ultrasonic transducers

3.4.3. Reception Response Characterisation

In order to test the performance of the SG fractal device in reception mode, a broadband 9 μm customised PVDF transmitter, which has the centre frequency at 900 kHz and -6 dB bandwidth from 150 kHz to 1750 kHz, was used as a transmitter for generating a common wideband acoustic signal and a calibrated hydrophone was initially used as the reference receiver. The impulse response of this customised PVDF transmitter is shown in Figure 3-19. The experimental setup is shown in Figure 3-20. The field pressure characteristic generated by the PVDF transmitter was measured by the calibrated hydrophone first. Once a calibrated reference signal was recorded, the PVDF transmitter was replaced by each of the three devices and the field pressure measured. The distance between the reference hydrophone and the receiving device was maintained at 150 mm.

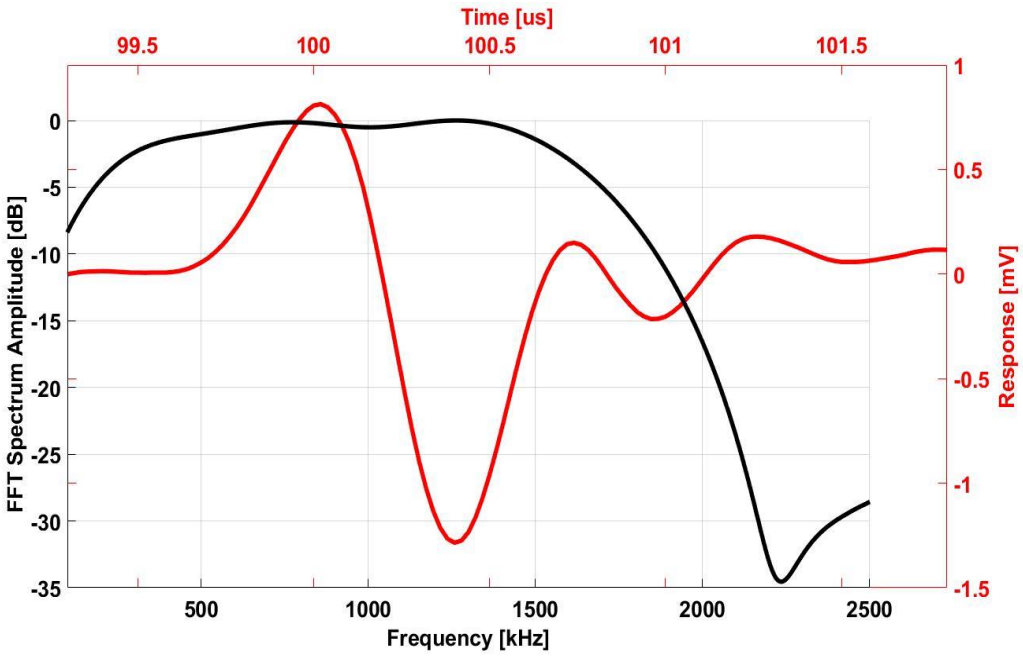

Figure 3-19: Impulse response of customised PVDF transmitter

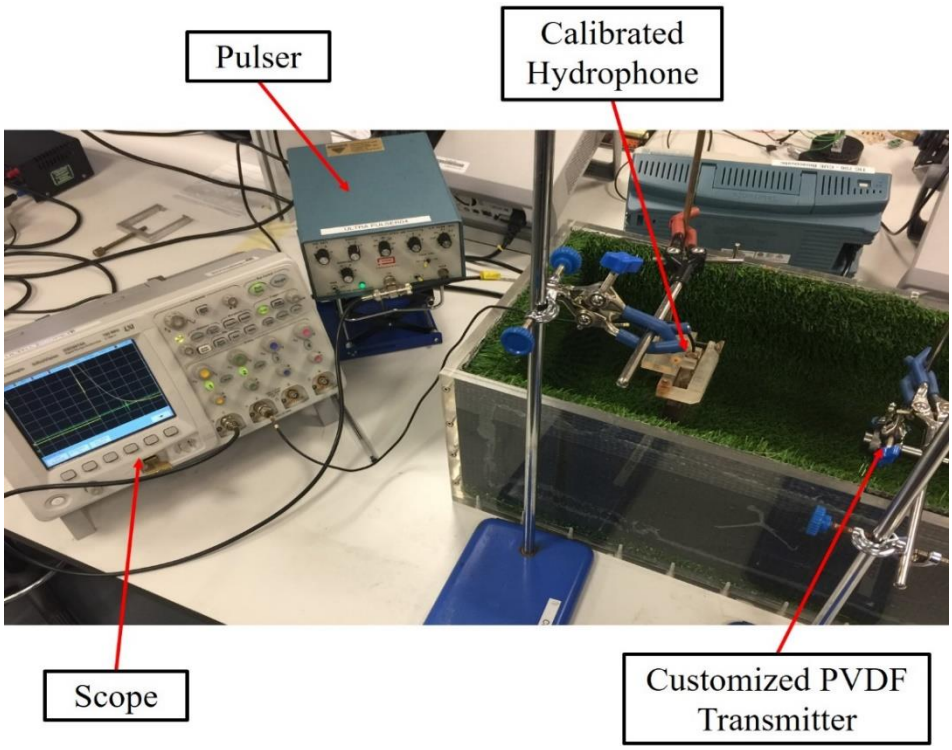

Figure 3-20: OCV measurement experimental setup

The OCV response can be calculated using Equation (3-10) and the resulting measured spectra are shown in Figure 3-21. It can be seen in Figure 3-21 that the -6 dB receiving bandwidth of the SG fractal device, the conventional composite design and the commercial transducer is 78.8 %, 76.9 % and 59.3 %, respectively, resulting in a 2.5 % and 32.9 % bandwidth extension being realized by the SG fractal design. In terms of the sensitivity level, the commercial device is less than 1 dB higher than the SG fractal design and conventional device.

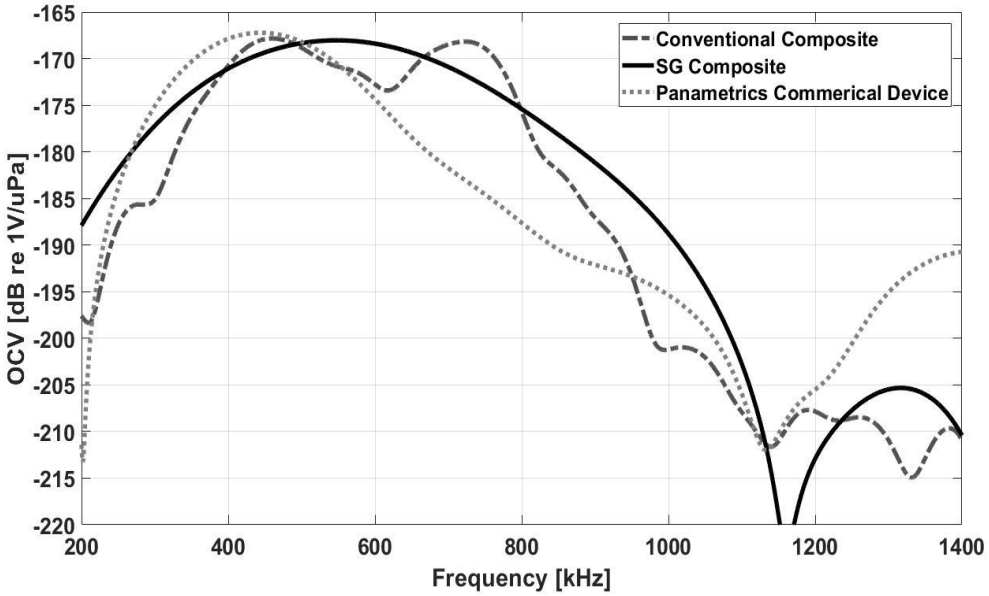

Figure 3-21: Measured OCV spectrum of the three ultrasonic transducers

3.4.4. Pulse Echo Response Characterisation

In order to further validate the advantage of designing a composite ultrasound transducer using a fractal geometry, the pulse-echo response of each device was measured

experimentally. The transducer was positioned in a water tank and a flat glass reflector with a thickness of 50 mm was placed in the far field of the transducer, which is 100 mm away from the transducer front face. The pulser / receiver (5052 PR, Panametrics, USA) was used to excite each transducer and then receive the reflected echo signal. The received echo signal was amplified with a gain of 20 dB by the instrumentation and displayed using an oscilloscope, where the experimental setup is shown in Figure 3-22. The measured time domain waveforms, normalized with respect to the transducer active area, are shown in Figure 3-23 and the resulting frequency responses are shown in Figure 3-24.

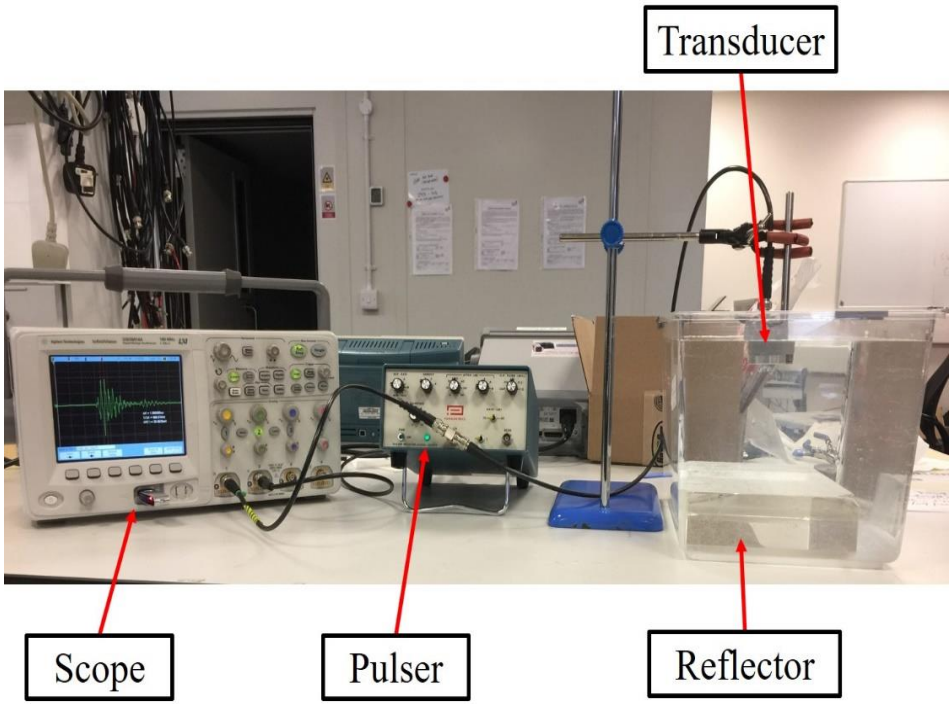

Figure 3-22: Pulse-echo measurement experimental setup

The resulting peak-to-peak echo signals from the front and back faces of the glass reflector in Figure 3-23 and the -6 dB fractional bandwidths for the three devices calculated from Figure 3-24 are listed in Table 3-5.

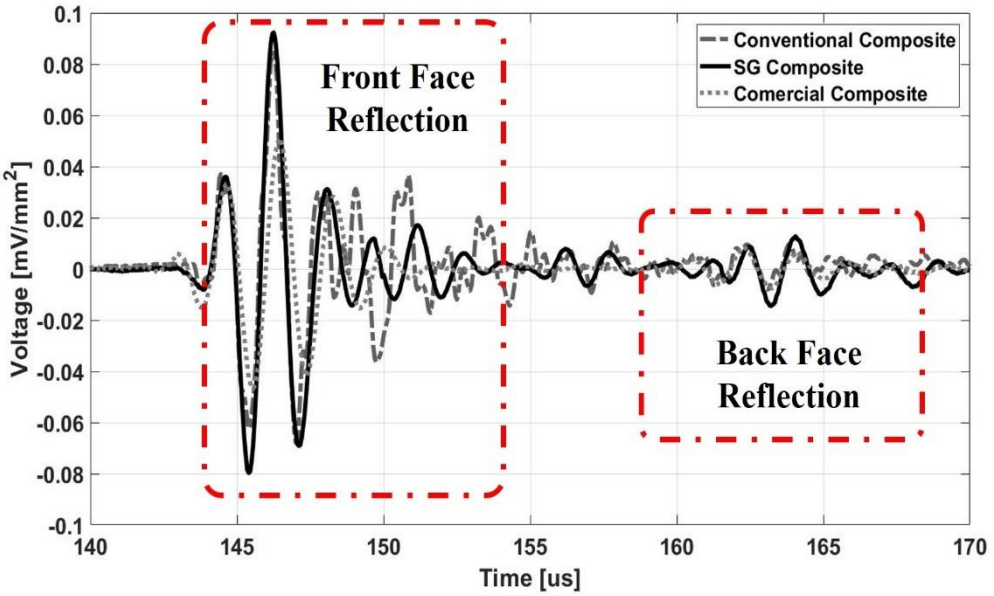

Figure 3-23: Measured time-domain pulse-echo waveform

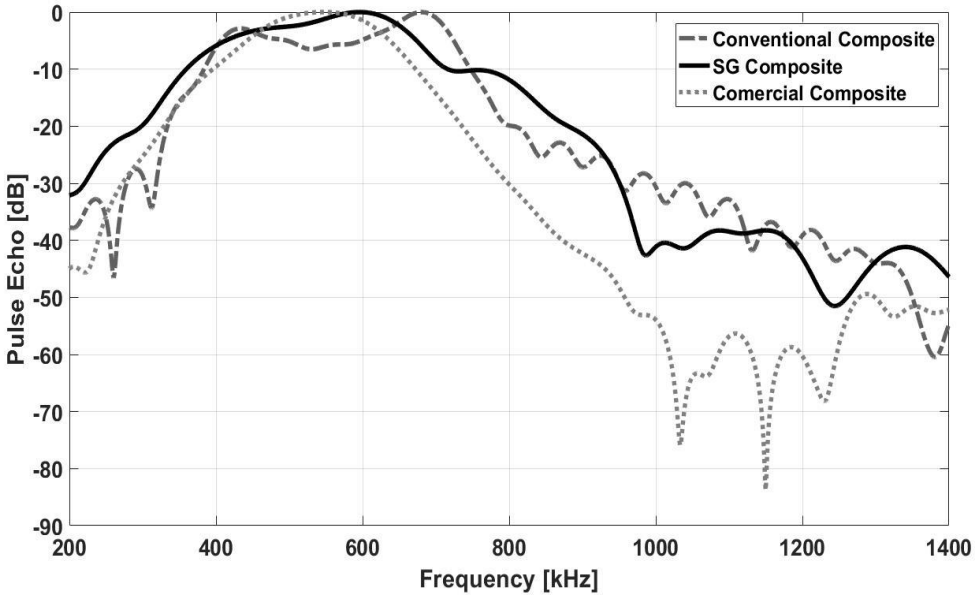

Figure 3-24: Pulse-echo frequency response spectra

Table 3-5: Pulse echo experimental results

	Front Face Echo	Back Face Echo	- 6dB Bandwidth
SG Fractal Composite Transducer	0.17 mV/mm^2	0.027 mV/mm^2	47.5 %
Conventional Composite Transducer	0.14 mV/mm^2	0.014 mV/mm^2	47.8 %
Panametrics Commercial Transducer	0.10 mV/mm^2	0.016 mV/mm^2	38.9 %

In the two-way pulse-echo experimental setup, the SG fractal device displayed an improved signal strength compared to the other devices. When the received time domain echo signal is normalized with respect to the transducer active aperture area, the signal strength of the SG fractal design is increased by 21.4 % and 70.0 % with respect to the conventional composite and commercial devices. The -6 dB bandwidth of the SG fractal design is approximately the same as the conventional composite design but enhanced by 22.1 % when compared with the commercial transducer.

3.5. Alternative Piezoelectric Composite Design Using SG Fractal Electrode

The SG transducer does appear to realise a marked improvement in device performance. This comes at a cost though, as the manufacture of the device is quite intricate and time consuming. There is motivation therefore to investigate a device that has the primary SG fractal geometric features but is easier to manufacture.

In this Section, the SG fractal geometry is used as an electrode pattern and applied to a conventional triangular cut composite. The performance of this SG fractal electroded composite is compared with the fully electroded composite in both transmission and reception mode through the FE simulated TVR and OCV spectrum.

Figure 3-25 illustrates the conventional 1-3 triangular cut composite which has similar design parameters as the SG fractal composite introduced in Section 3.2.2.

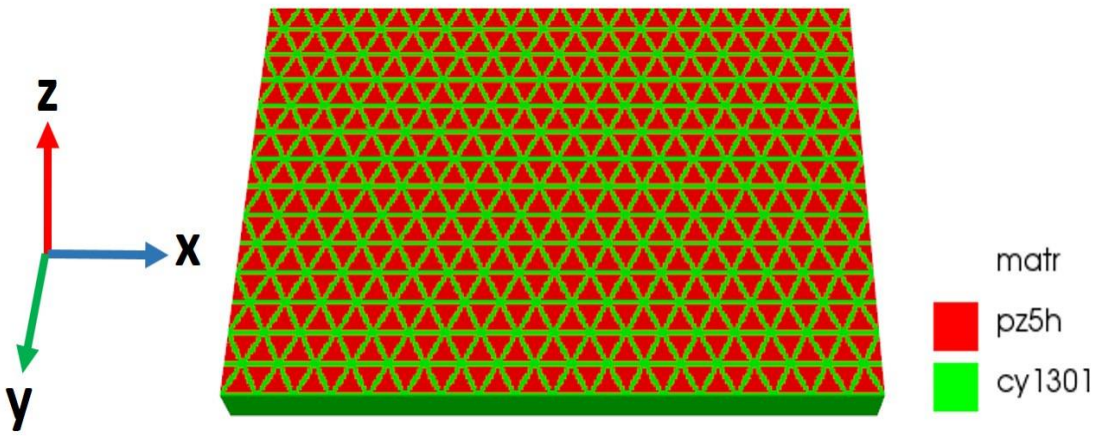

Figure 3-25: 1-3 Triangular Cut composite active layer used as substrate for fractal electrode

The specification of the conventional triangular cut composite is shown in Table 3-6.

Table 3-6: Specification of Conventional Triangular Cut Composite Design

	Material	**Thickness**	**Pillar Width**	**Ceramic Volume Fraction**
Triangular Cut Composite	PZT-5H & Hardset Polymer	2.6 mm	1.0 mm	61.6 %

A SG fractal electrode, shown in Figure 3-26 (a) and a full electrode, shown in Figure 3-26 (b) is applied on this 1-3 triangular-cut composite substrate respectively in order to explore the influence of using the SG fractal electrode pattern on a conventional composite design.

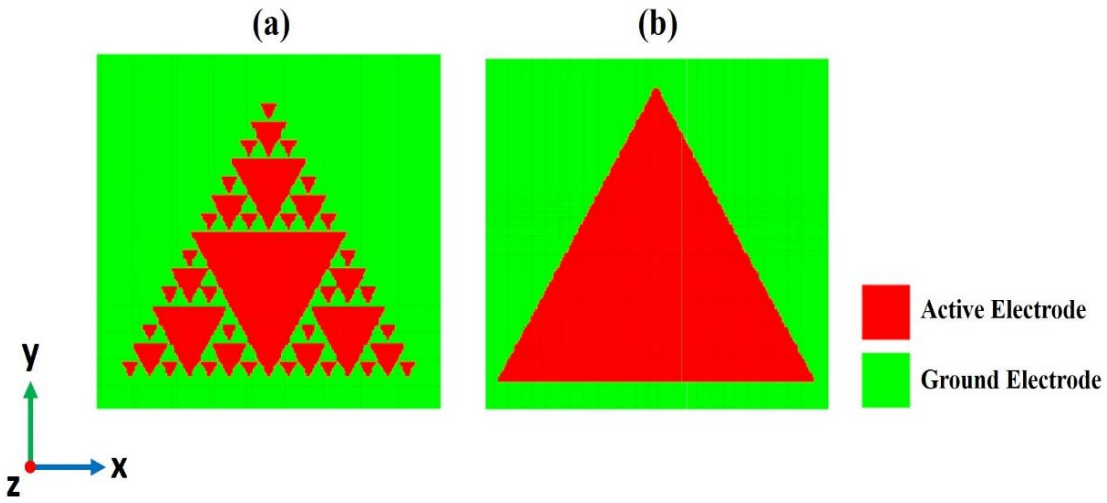

Figure 3-26: Electrode pattern applied to a conventional 1-3 composite design: (a) SG fractal electrode configuration; (b) Full electrode configuration

The resulting TVR and OCV response achieved from the FE simulation for these two electrode configurations is shown in Figure 3-27 and Figure 3-28, respectively.

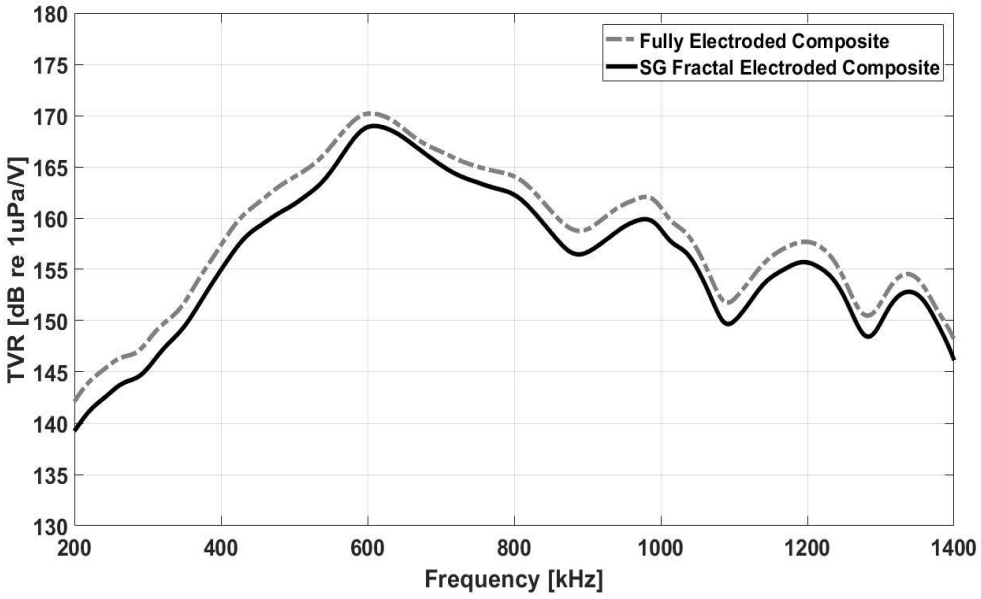

Figure 3-27: Simulated TVR spectra with full and fractal electrode patterns

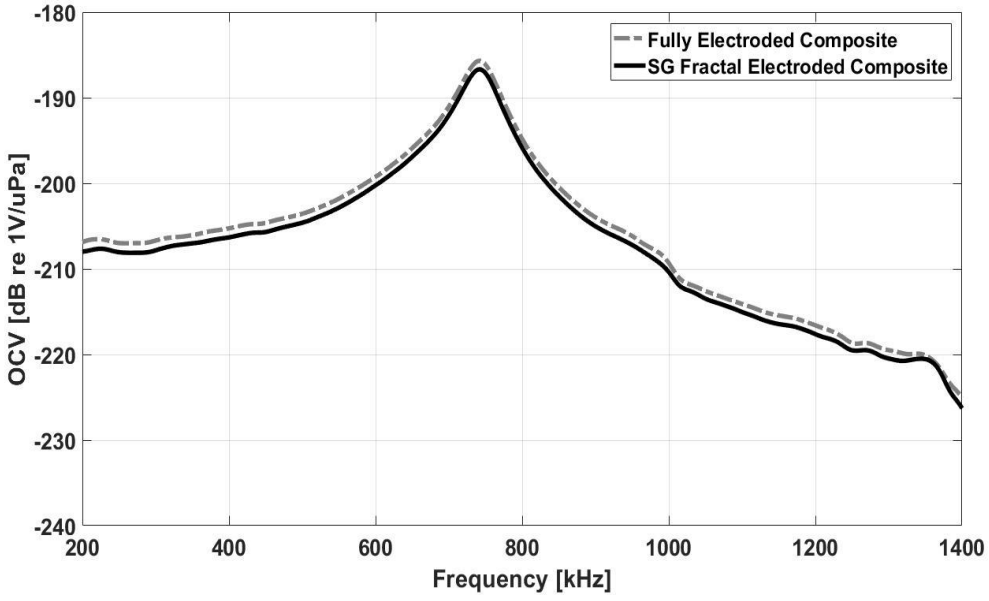

Figure 3-28: Simulated OCV spectra with full and fractal electrode patterns

As shown in Figure 3-27, in the transmission mode, the composite material performed better with a full electrode. The sensitivity dropped by 1 dB when a SG fractal electrode

was used. The primary reason is that a fully electroded device can drive more active ceramic material compared to a fractal electrode. In the reception mode, shown in Figure 3-28, the performance of the SG fractal electroded composite and fully electroded composite are approximately the same as each other. Albeit, that the standard composite structure slightly outperforms the fractal electroded device.

3.6. Discussion & Chapter Summary

In this Chapter, a novel 1-3 piezoelectric composite design using a SG fractal geometry was proposed in order to explore the potential of further extending the operational bandwidth and sensitivity of the transducer. Two equivalent 1-3 composite designs were compared to this end, one with a conventional periodic parallelepiped shaped pillar structure and one with the SG fractal geometry at fractal generation Level IV, both theoretically, using a FE analysis package, and experimentally.

The electrical impedance of a SG fractal composite was simulated and a multi-modal characteristic was found in the SG fractal composite design. By analysing the displacement mode shape in the thickness direction, it was observed that this multi-modal behaviour was due to the triangular pillars in different sizes resonating at different frequencies in the thickness direction. The beam profile of both composites, predicted using Huygens-Fresnel principle, also indicated that by using the SG fractal geometry, the side lobe amplitude can be reduced by 5 dB. The FE modelling results showed that the bandwidth extension can be realized by coupling different resonance modes of triangular pillars with varying length scales in the SG fractal composite design. Moreover, the

absence of parallel faces between elements in this SG fractal composite design leads to a reduction in the inter-pillar resonant activity in the lateral dimension. Therefore, the thickness coupling efficiency can be increased, which results in a sensitivity improvement of the SG fractal composite device.

Following the simulation results, a single element transducer utilizing the SG fractal microstructure, was fabricated using a pillar placement method, where the ceramic pillars in different sizes were positioned individually in a 3D printed mould. The TVR, OCV and pulse-echo response were used to illustrate the bandwidth and sensitivity improvement that arose from the fractal composite design and compared with a conventional 1-3 composite design, as well as with a commercial Panametrics ultrasound transducer. In transmission mode, a bandwidth improvement of 27.2 % and a sensitivity enhancement of 3.8 dB was found with the SG fractal design compared to the equivalent conventional composite design and up to a 105.1 % bandwidth improvement when compared to the commercial device. In reception mode, the bandwidth improvement for the SG fractal design was 2.5 % and 32.9 % when compared to the conventional and commercial transducers, respectively. Moreover, in pulse-echo mode, the SG fractal design demonstrated a 21.4 % and 70.0 % sensitivity improvement when compared to the conventional 1-3 transducer and commercial device, respectively. The bandwidth of the SG fractal design was also 22.1 % enhanced with respect to the commercial device.

It should be noted that neither the 1-3 composite or the SG fractal devices have been backed, whereas the commercial device incorporates both matching and backing to extend its bandwidth. Therefore, the device comparison is not equivalent, but the commercial

device does provide a known benchmark performance against which the other devices can be compared. This is particularly evident in Figure 3-23, where the axial resolution of the commercial device would highlight this device for conventional imaging applications. Nevertheless, the SG device has achieved a wider operational bandwidth when compared to the equivalent standard 1-3 composite and hence, the addition of a backing layer in future designs should provide additional damping to improve the axial resolution performance and increase the operational bandwidth.

The possibility of enhancing transducer performance by using a fractal electrode was also studied in this Chapter. However, the FE simulation results showed that the performance of a triangular cut composite cannot be improved by applying an electrode with the SG fractal configuration, when compared to the situation when it was fully electroded.

CHAPTER IV

PIEZOELECTRIC COMPOSITE DESIGN INCORPORATING SIERPINSKI CARPET FRACTAL GEOMETRY

In the previous Chapter, the fractal geometry, Sierpinski Gasket, was employed to develop a single element ultrasound transducer, which has achieved improved performance in terms of bandwidth, sensitivity and beam forming when compared to traditional 1-3 piezoelectric composite design.

In this Chapter, another fractal geometry named as, Sierpinski Carpet (SC) will be studied using the FE analysis package, PZFlex. This modelling approach will be used to go through a number of parameter sweep simulations in order to find an optimal design of the SC fractal composite with maximised bandwidth performance. The transmitting voltage response (TVR), open circuit voltage response (OCV) as well as the pulse-echo response of this SC fractal composite will be simulated to provide quantitative comparisons between the SC fractal composite and a conventional 1-3 composite design.

In addition to using the SC fractal geometry as the structure of the composite design, the influence of using a SC fractal electrode pattern on a conventional 1-3 composite will also be investigated in this Chapter, in order to further corroborate the results achieved in Chapter III, where it was demonstrated that the operating performance of a composite will not be improved by using a fractal electrode configuration.

4.1. Sierpinski Carpet Geometry

Figure 4-1 shows the first three fractal generation levels of the SC fractal geometry. It can be seen from Figure 4-1 that the SC fractal geometry starts with a square at generation Level 0. When the SC fractal geometry moving to the next generation level, Level I, the square is divided into 9 congruent sub-squares in a form of 3-by-3 grid structure and the sub-square at the central is removed. The same iterative rule can be applied to the rest of 8 sub-squares to achieve the SC fractal geometry in the generation Level II, ad infinitum for another higher generation level.

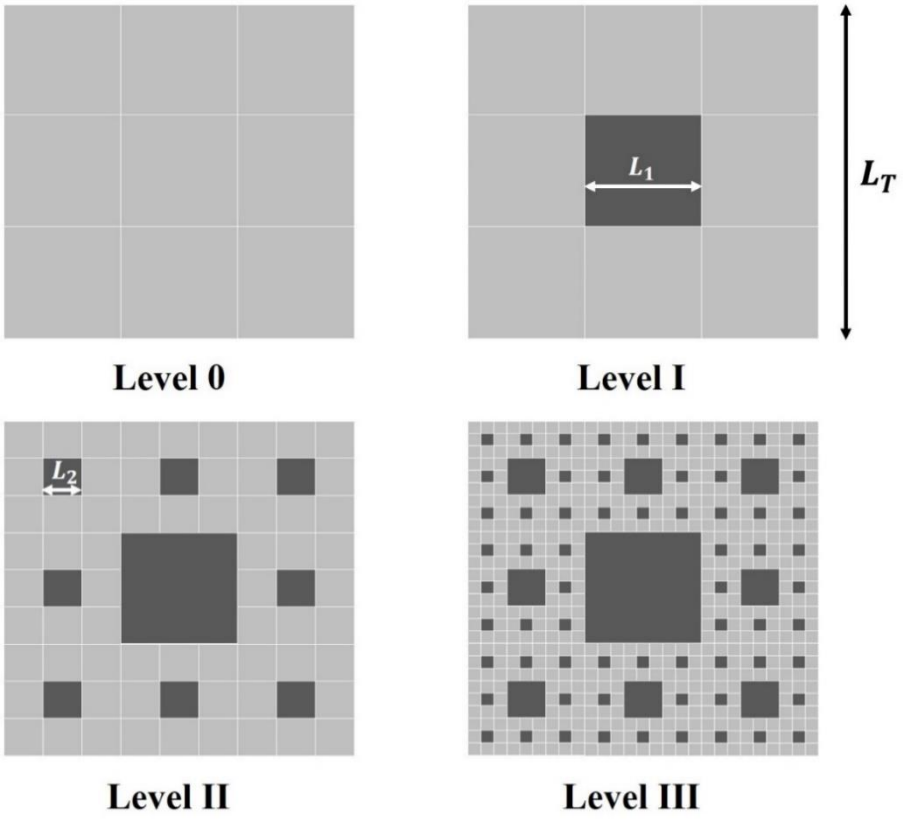

Figure 4-1: SC fractal geometry at first three generation levels. Note that the smallest piezoceramic elements in the Level III configuration have width, L_3

For a SC fractal geometry at generation Level N (N > 0) with a total lateral length of L_T, the lateral length of the piezoelectric element, L_k (k ≤ N), can be calculated using Equation (4-1).

$$L_k = \frac{L_T}{3^k} \tag{4-1}$$

4.2. Piezoelectric Composite Design Using Sierpinski Carpet Geometry

The SC fractal geometry at generation Level III shown in the Figure 4-1 is now considered as the microstructure of a 1-3 composite, where PZT-5H (Meggitt A/S, Kvistgard, Denmark) is used as the active piezoelectric material and hardset polymer (Robnor Resin Ltd, UK) is employed to be the passive filler material. Two 3D FE models of a SC composite and a conventional periodic 1-3 have been developed as shown in Figure 4-2.

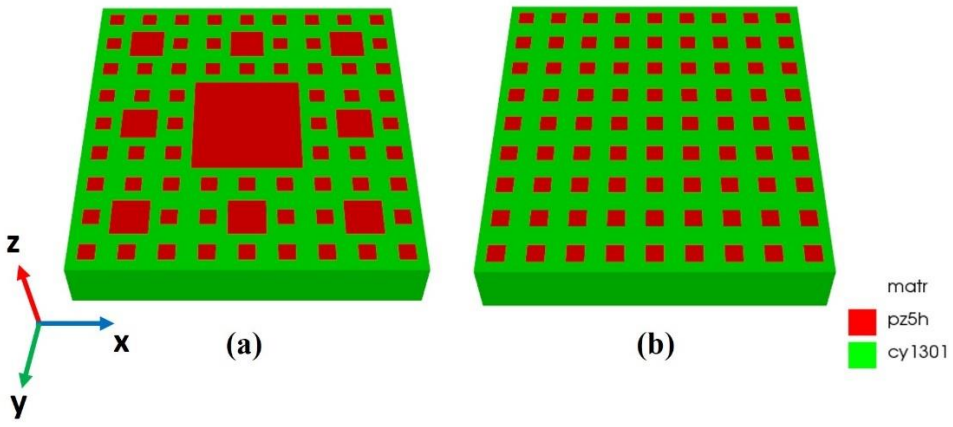

Figure 4-2: FE composite model: (a) Level III SC fractal composite; (b) conventional 1-3 composite

In order to find an optimal solution for the SC fractal composite design, particularly with respect to wide operational bandwidth, three design parameter sweep simulations are performed using PZFlex regarding the pillar width, material thickness and the distance between two smallest pillars of this SC composite. The resulting mechanical Q-factors, defined as the ratio of the centre frequency value to the half amplitude bandwidth in the conductance spectrum, were calculated to describe the device bandwidth. A low value of the Q-factor equates to a broadband characteristic.

4.2.1. Simulation Sweep I: Varying the Pillar Width

First of all, considering the manufacturing difficulties in the future, the pillar width of the smallest pillar at fractal generation Level III, L_3, is varied from 0.5 mm to 2.0 mm with the step of 0.1 mm. Secondly, the thickness of the SC composite is set to be 2.6 mm for the purpose of keeping a reasonable pillar aspect ratio (AR), ranging from 0.19 to 0.77, to produce a good surface dilation quality for the device. The resulting conductance spectrum and the calculated Q-factor for different values of L_3 are shown in Figure 4-3 Figure 4-4, respectively. The peak of each main lobe in the conductance spectrum is marked with a red dot.

It can be seen from Figure 4-4 that when the value of the L_3 equals to 0.5 mm, the lowest Q-factor value calculated from the main lobe of the conductance spectra can be achieved, which means the highest bandwidth is obtained, when compared to other conditions. As the result, the value of L_3 is chosen to be 0.5 mm for maximizing the bandwidth performance of the SC fractal composite design.

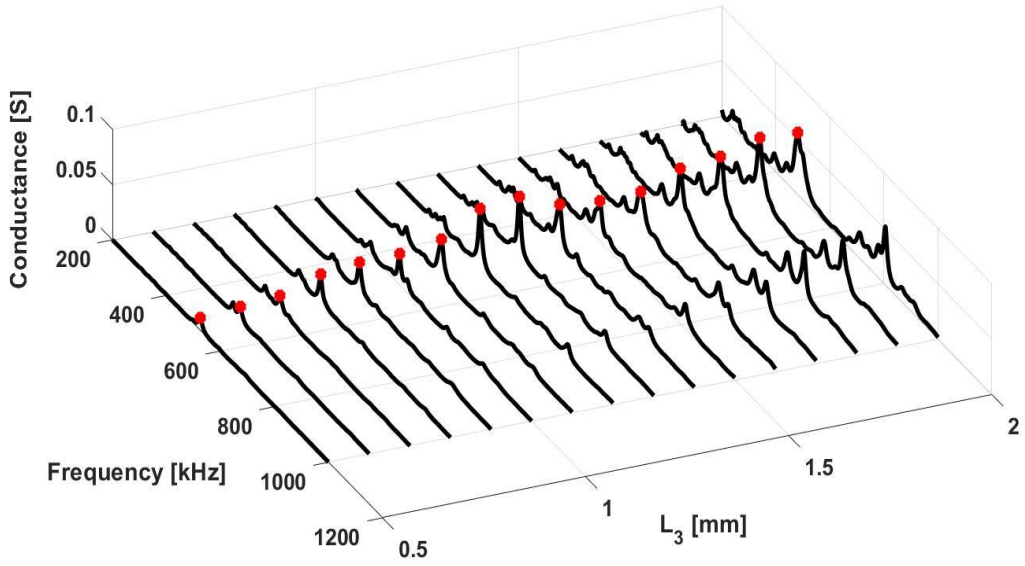

Figure 4-3: FE derived conductance spectrum for different values of L_3 in the SC composite design

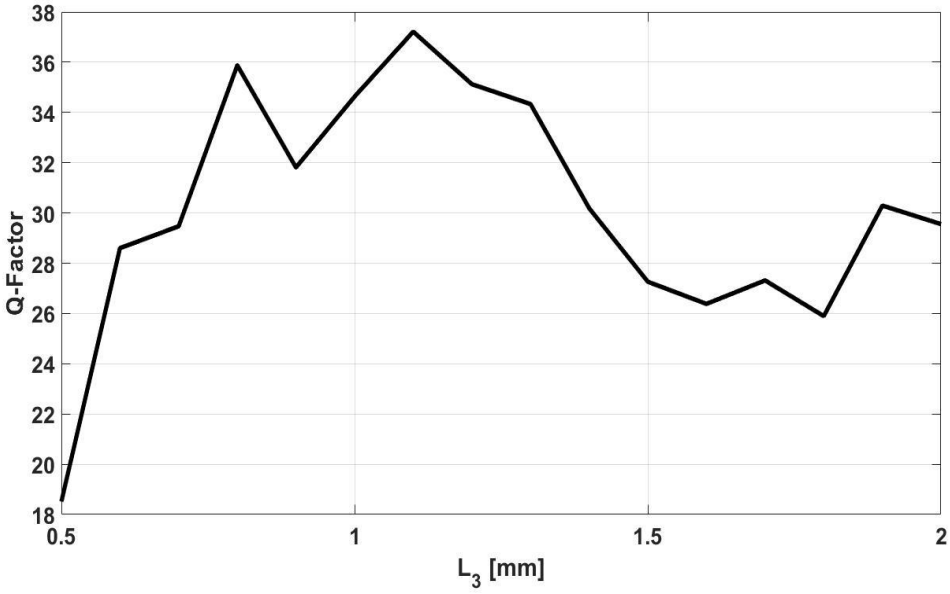

Figure 4-4: Q-factor for different values of L_3 in the SC composite design

4.2.2. Simulation Sweep II: Varying the Thickness

In the second simulation sweep, the value of the L_3 is fixed as 0.5 mm and the thickness of the SC composite is varied from 1.5 mm to 3.0 mm with a step of 0.1 mm in order to find an optimal thickness value for maximizing operational bandwidth. The resulting conductance spectrum and Q-factor for different active layer thicknesses are shown in Figure 4-5 and Figure 4-6, respectively.

Figure 4-6 clearly shows that the lowest Q-factor calculated from the conductance main lobe can be obtained when the material thickness equals 2.4 mm, which again is where the highest bandwidth is predicted to be achieved.

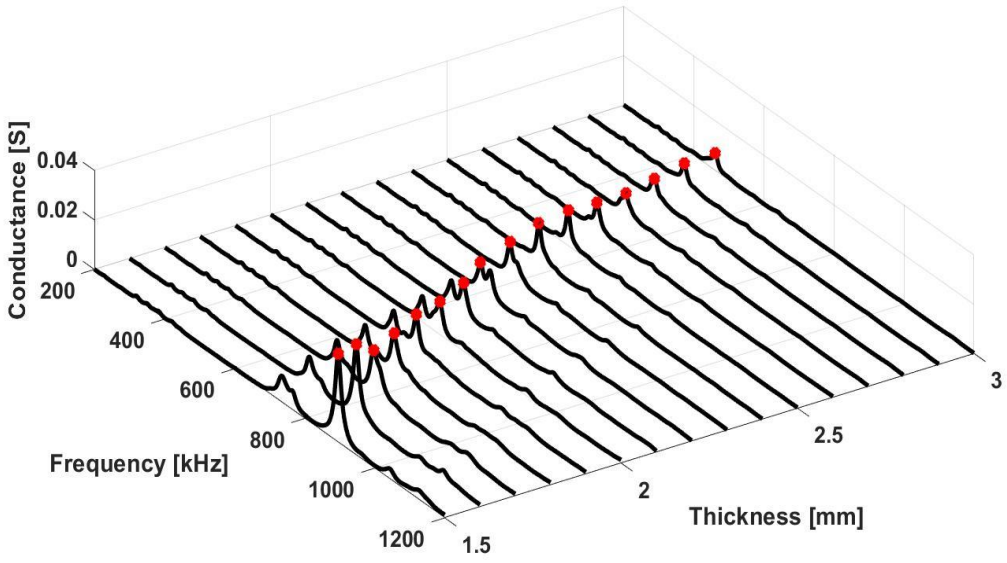

Figure 4-5: FE derived conductance spectrum for different values of thickness in the SC composite design

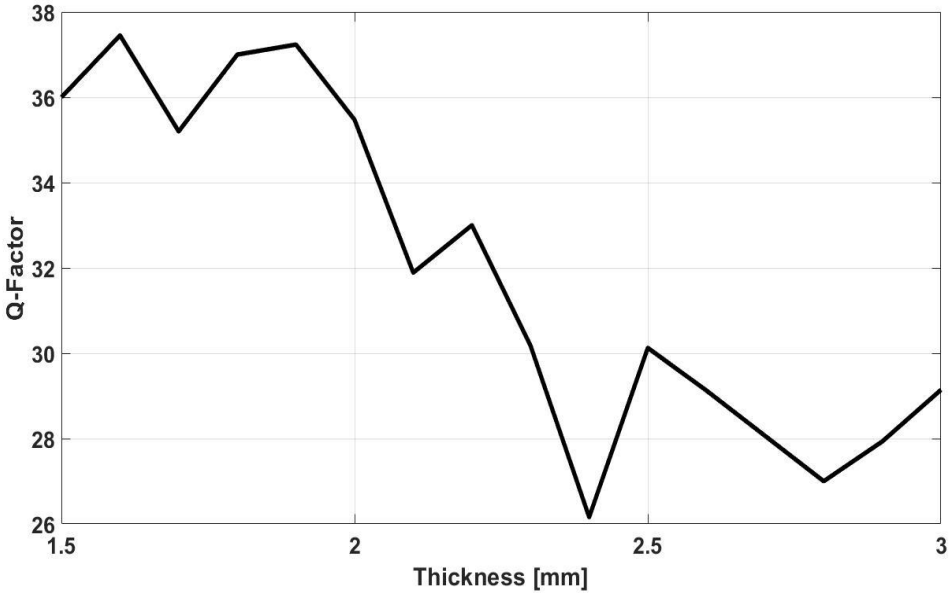

Figure 4-6: Q-factor for different values of thickness in the SC composite design

4.2.3. Simulation Sweep III: Varying the Pillar Separation Distance

According to the results from previous two simulation sweeps, a composite design using SC fractal geometry at generation Level III with good operational bandwidth performance can be obtained when the composite thickness is 2.4 mm and L_3 is 0.5 mm. However, the ceramic volume fraction (VF) of this SC composite has been fixed at 30 % in the thickness parameter simulation. In order to further optimise the composite performance, a simulation sweep was introduced regarding the distance between two smallest pillars, d_{s-s}, in this SC composite design. This spatial variation in the composite microstructure will modify VF, as illustrated in Figure 4-7.

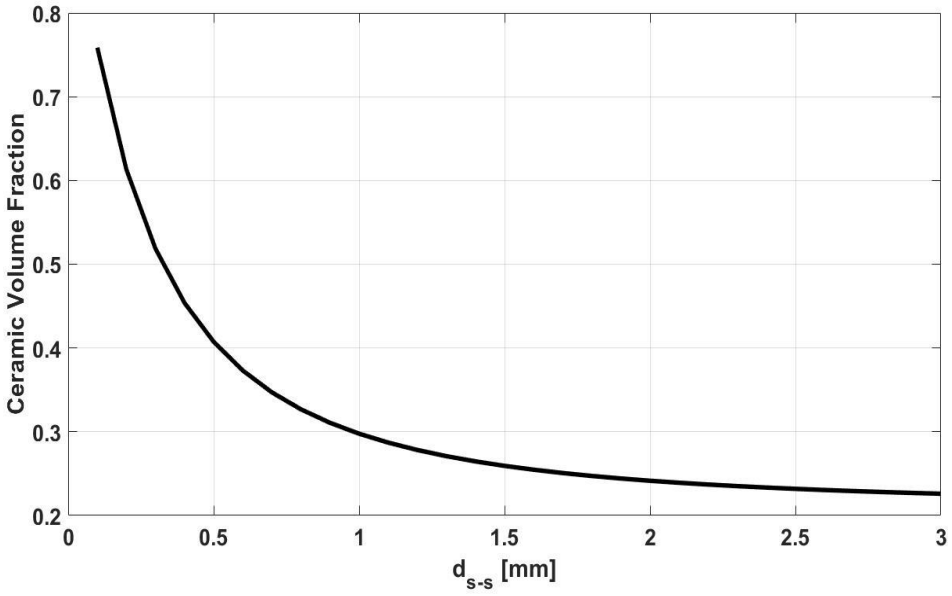

Figure 4-7: Ceramic volume fraction variation with respect to different values of d_{s-s}

It can be seen from Figure 4-7 that the VF of the SC composite decreases exponentially with an increased in value of d_{s-s}. Hence, a parameter sweep simulation with d_{s-s} varying from 0.3 mm to 2.0 mm with a step size of 0.1 mm is performed and the resulting conductance spectra and the calculated Q-factor are shown in Figure 4-8 and Figure 4-9, respectively.

It can be observed in Figure 4-9 that when the distance between two smallest pillars, d_{s-s}, in the SC composite equals to 0.5 mm, the SC composite has the smallest Q-factor value. At this point, the complete design of a SC composite is finished and Table 4-1 describes the full manufacturing specification of the designed SC composite configuration.

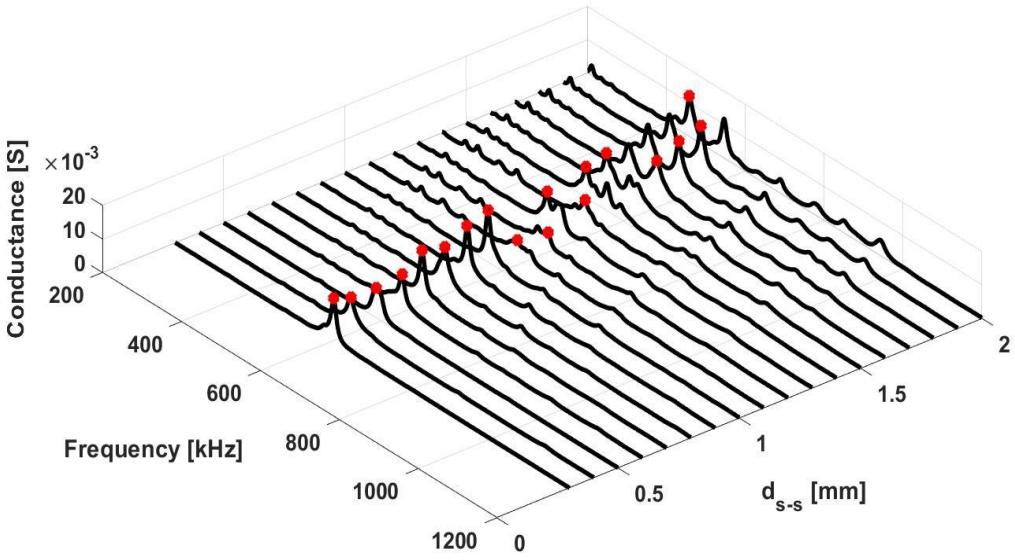

Figure 4-8: FE derived conductance spectrum for different values of d_{s-s} in the SC composite design

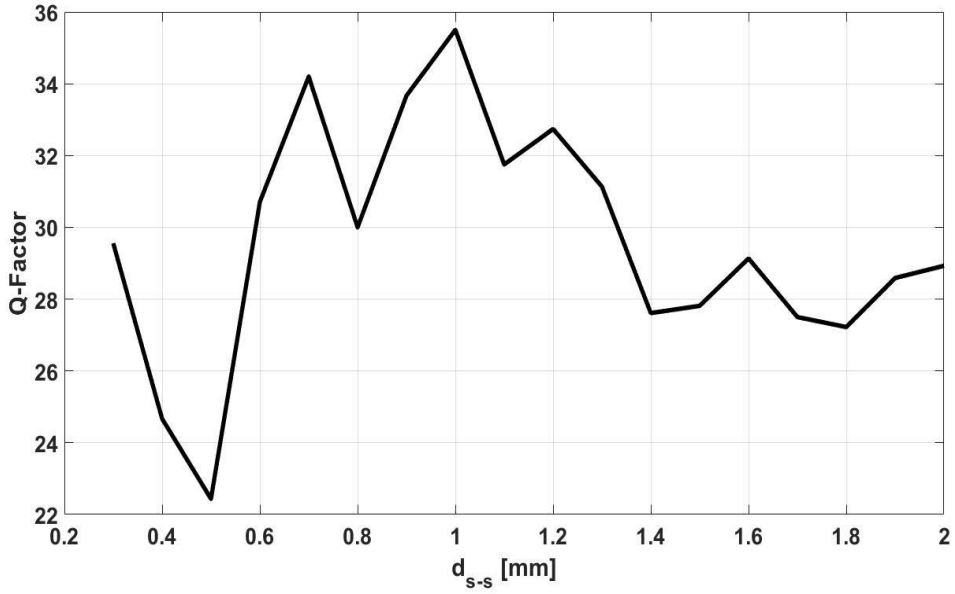

Figure 4-9: Q-factor for different values of d_{s-s} in the SC composite design

Table 4-1: SC composite model specification

Active Phase Material	**Passive Phase Material**	L_1	L_2	L_3	**Thickness**	d_{s-s}	**VF**
PZT-5H	Hardset Polymer	3.0 mm	1.0 mm	0.5 mm	2.4 mm	0.5 mm	0.41

In order to evaluate any operational improvement of the SC composite design with respect to a conventional composite design, an equivalent conventional parallelepiped 1-3 composite, as shown in Figure 4-2 (b) is designed for comparison. In order to keep consistency and provide a fair comparison between the two composite designs, the fundamental design parameters of the conventional 1-3 composite is kept the same with the SC composite. Thus, the 1-3 composite incorporated the same piezoceramic and polymer materials as the SC device and has fabrication parameters as detailed in Table 4-2.

Table 4-2: 1-3 composite model specification

Active Phase Material	**Passive Phase Material**	**Pillar Width**	**Thickness**	**Kerf Width**	**VF**
PZT-5H	Hardset Polymer	0.5 mm	2.4 mm	0.28mm	0.41

4.3. Finite Element Modelling of Single Element SC Fractal Composite Transducer

4.3.1. Electrical Impedance

The electrical impedance of the Level III SC composite and its equivalent conventional 1-3 composite is initially simulated without a matching layer. The FE derived impedance magnitude spectra of both composites are shown in Figure 4-10.

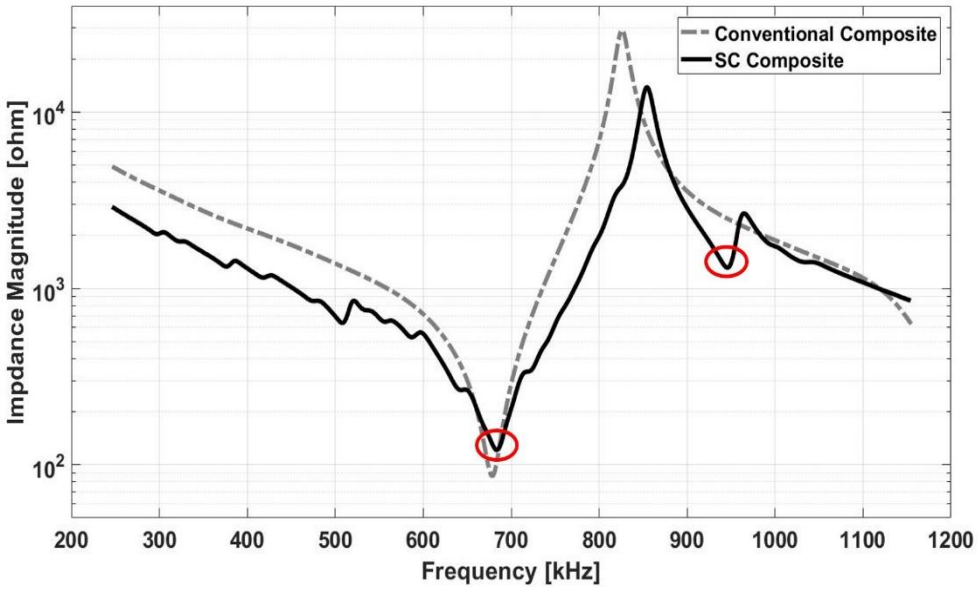

Figure 4-10: FE derived electrical impedance magnitude spectrum of the SC and the conventional composite

It can be seen from the Figure 4-10 that the SC composite with multiple pillar sizes has two main resonant frequencies, the minima of which are located at 684 kHz and 946 kHz, respectively, and marked with a red circle in the Figure. There is only one resonance mode

in the impedance magnitude spectrum of the conventional 1-3 composite, which is at the frequency of 679 kHz. The global minima and maxima frequencies of each composite design is considered as their main electrical resonant and mechanical resonant frequency and were used to calculate the effective electromechanical coupling coefficient, k_t. The k_t of SC fractal composite is 0.64 against 0.61 for the conventional 1-3 composite. Hence, similar to the SG result presented in Chapter III, a lager k_t value can be obtained by using the SC fractal geometry, where a potential energy conversion and bandwidth enhancement may be realized. This is an encouraging result, albeit recognizing that the 1-3 composite configuration has not been fully optimised.

4.3.2. Vibrational Mode Analysis

As shown in Figure 4-10, two resonant modes can be found in the SC fractal composite design, which is due to its multiple piezoceramic pillar sizes.

In order to explore the resonance behaviour of the SC composite at these resonance frequencies, the displacement mode characteristic in thickness direction was investigated for the SC composite at each frequency marked with red circle in Figure 4-10. For the purpose of comparing the strength of each mode, all thickness displacement data were normalised to the maximum thickness displacement of the first resonant mode shown in Figure 4-11 (a). It should be noted that the displacement is presented as a top down view onto the front vibrating surface of the transducer.

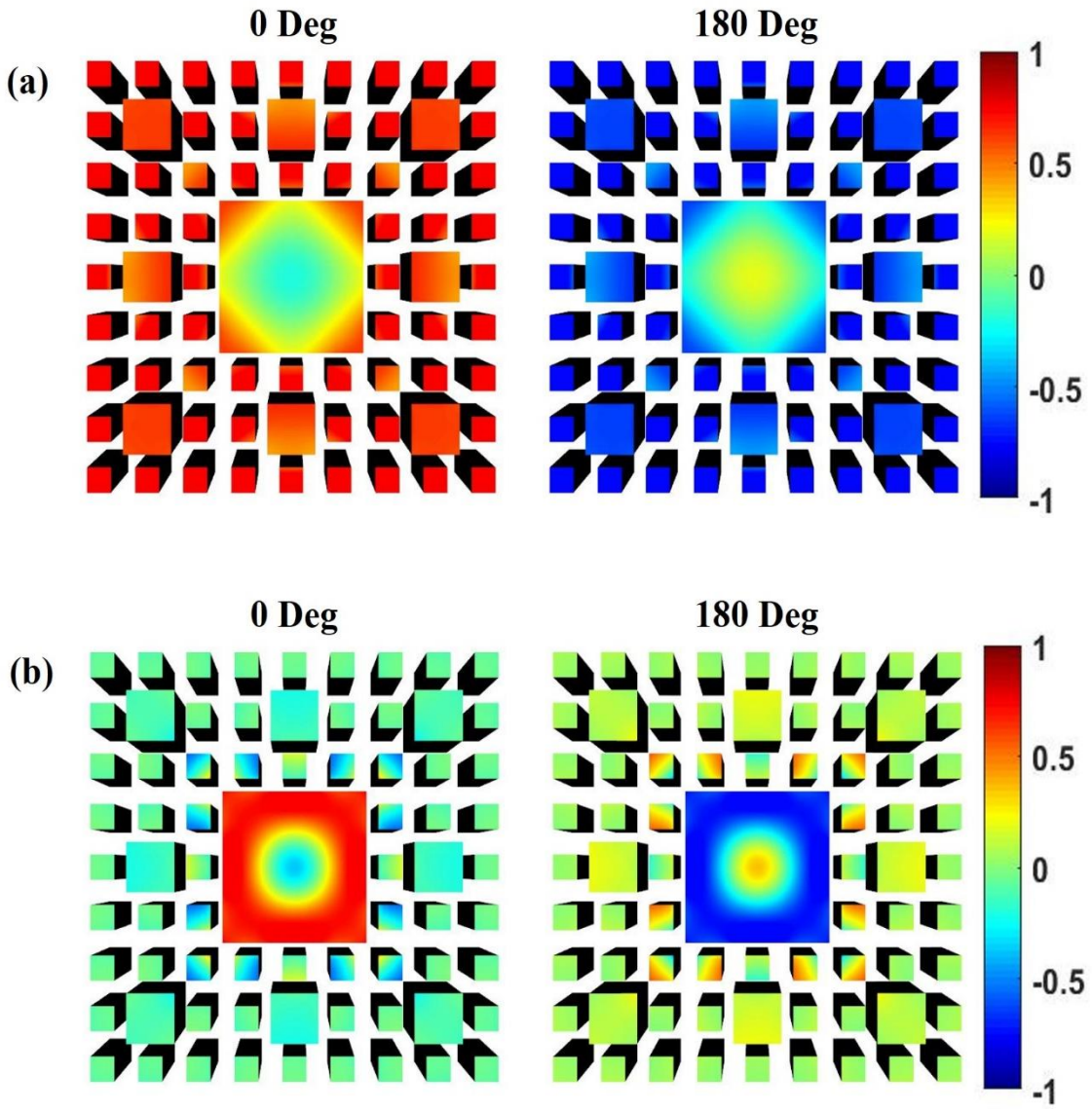

Figure 4-11: SC composite displacement mode shape in thickness direction at: (a) 684 kHz and (b) 946 kHz

It can be observed from Figure 4-11 (a) that at 684 kHz, a strong thickness vibration behaviour is exhibited in the ceramic pillar at generation Level II and III, which have the pillar widths of 0.5 mm and 1.0 mm, respectively. The surface dilation quality factor, Q_{dil} defined in Equation (2-11), describes the uniformity of the surface displacement and was

calculated as 0.88. At the frequency of 946 kHz, in Figure 4-11 (b), the lateral resonance of the pillar at generation Level I with pillar width of 3.0 mm dominates the vibrational response and leads to a very low FE derived Q_{dil} of 0.16. As for the conventional 1-3 composite, at its resonance frequency, 679 kHz, the Q_{dil} of 0.97 was calculated. It can be noticed that similar to the condition of SG composite design described in Chapter III, the Q_{dil} of SC composite is lower than the conventional 1-3 composite. Again, the reason is due to the surface antiphase resonance behaviour evident in the pillar with large pillar aspect ratio at low fractal generation level. It needs to be emphasized again that the design premise of the fractal geometry composite is to couple multiple resonance modes and hence, the design philosophy is not directly comparable to the well-known conventional 1-3 composite theory.

4.3.3. Matching Layer Design

The same dual matching layer scheme as described in Section 3.2.2.3, is used to couple both composites to a water load. The outer matching layer is a 413 μm layer of CY221/HY956EN medium set polymer (Robnor Resin Ltd, UK) and the inner matching layer is a 883 μm layer of loaded hardset polymer (50% weight fraction using 3 μm alumina powder) (Robnor Resin Ltd, UK). The FE simulated TVR of the SC fractal composite with and without this matching layer configuration is plotted in Figure 4-12. It can be seen that the sensitivity of the SC composite can be enhanced by approximately 3 dB after applying this dual matching system.

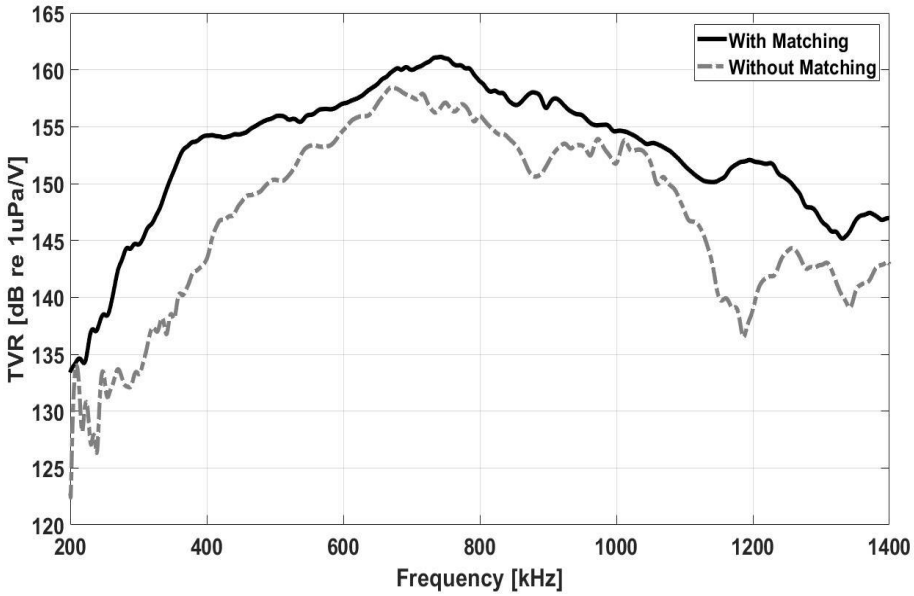

Figure 4-12: Simulated TVR spectrum of the SC composite with and without matching layer

4.3.4. Transmission and Reception Response Modelling

The one-way transmission and reception response of both SC and conventional composite was simulated using this FE analysis method. Both devices are matched to a water load via a dual matching layer scheme. The predicted TVR and OCV are shown in Figure 4-13 and Figure 4-14, respectively. The peak gain and -6 dB operational bandwidth of both devices in one-way transmission and reception mode are summarized in Table 4-3.

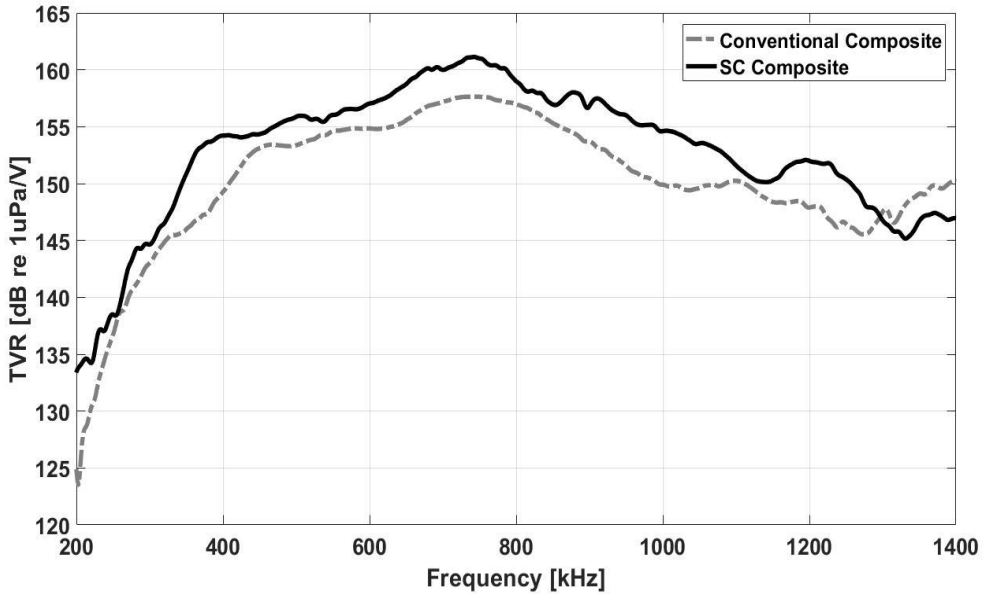

Figure 4-13: Simulated TVR spectrum of the SC and the conventional composite ultrasonic transducers

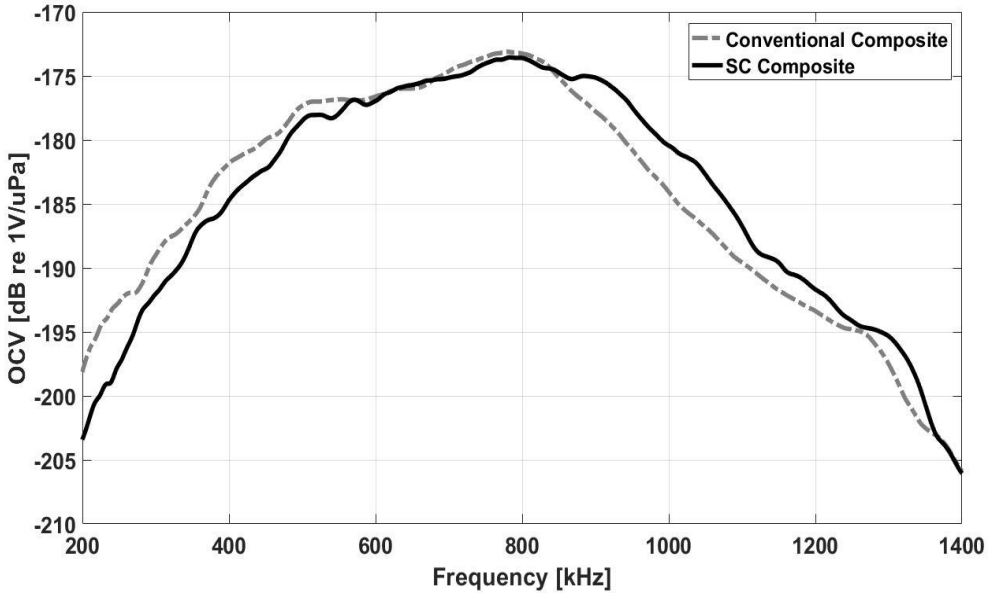

Figure 4-14: Simulated OCV spectrum of the SC and the conventional composite ultrasonic transducers

Table 4-3: Simulated transmission and reception TVR and OCV results

	SC Composite	Conventional Composite
Transmission Bandwidth (%)	70.5 %	64.1 %
TVR Peak (dB)	161.1 dB	157.6 dB
Reception Bandwidth (%)	63.5 %	57.5 %
OCV Peak (dB)	-173.5 dB	-173.1 dB

From Table 4-3, in transmission mode, both the operational bandwidth and sensitivity of the composite device can be improved by using the SC fractal geometry as the structure of a piezoelectric composite design rather than an equivalent 1-3 composite design. The bandwidth of the SC composite is improved by 10.0 % and sensitivity is increased 3.5 dB. In reception mode, the SC fractal composite bandwidth is 10.4 % higher than the conventional composite, but the sensitivity is 0.4 dB lower. This result correlates well to the results achieved in Chapter III using the SG fractal configuration. Hence, it can be hypothesised that when using a fractal geometry, both bandwidth and sensitivity can be improved in transmission mode, but in the reception mode only bandwidth enhancement can be realised.

4.3.5. Pulse-Echo Response Modelling

The two-way far-field pulse-echo response of both composite designs was also simulated when matched to a water load via the dual matching layer scheme design in Section 4.3.3. The predicted result is shown in Figure 4-15.

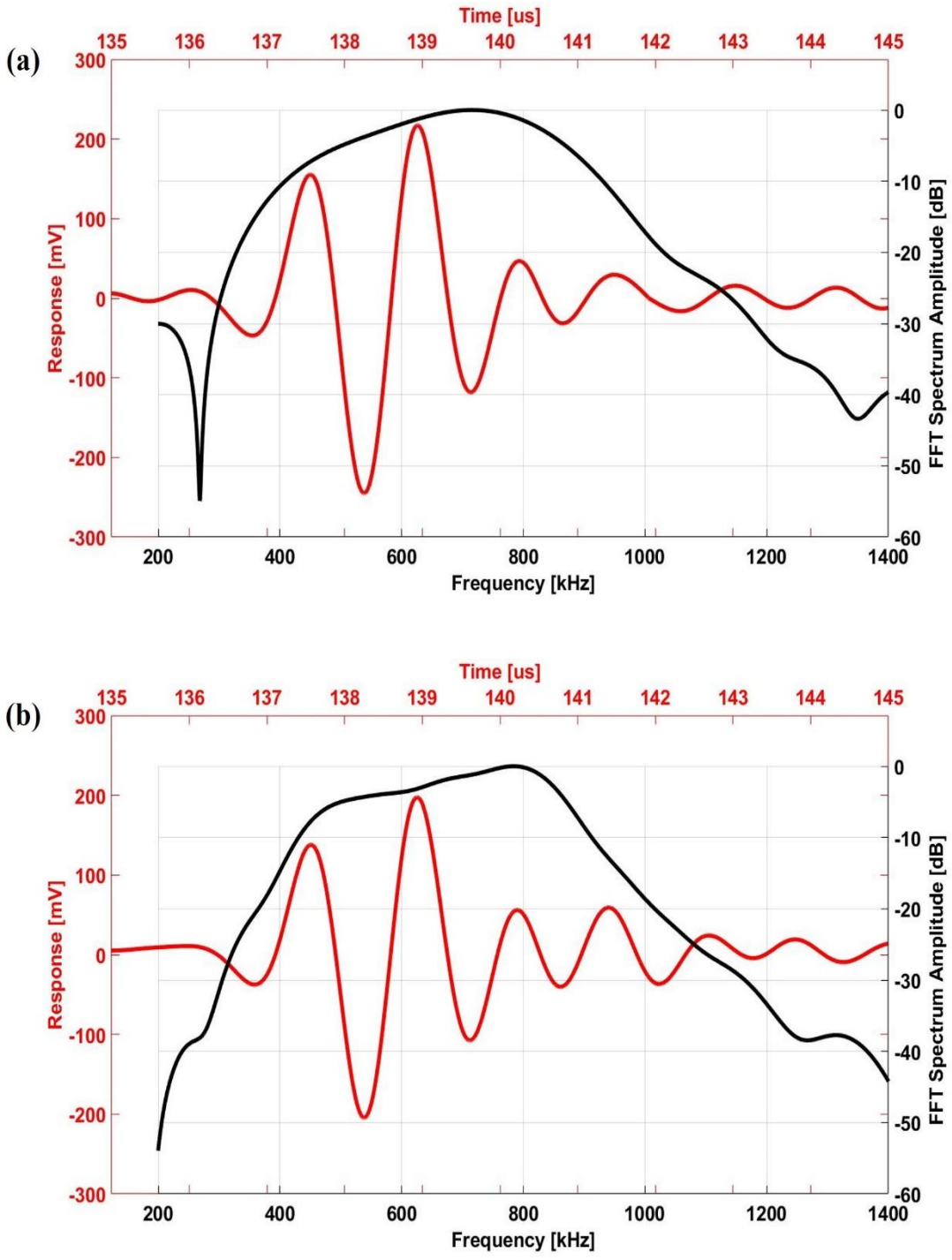

Figure 4-15: Simulated pulse-echo responses of: (a) SC composite; (b) conventional 1-3 composite

It can be determined from Figure 4-15 (a) that the SC fractal composite has the -6 dB bandwidth of 57.1 % and peak-to-peak voltage of 462.3 mV, where the conventional 1-3 composite has the -6 dB bandwidth of 51.7 % and peak-to-peak voltage of 402.0 mV. This corresponds to a 10.4 % bandwidth improvement and 15.0 % sensitivity enhancement achieved by the SC composite, when compared with the conventional composite. Again, this correlates well with the SG results presented in Chapter III.

4.3.6. Beam Profile Modelling

The beam profile of the SC fractal and the conventional composite in x-z plane, defined in Figure 4-2, was simulated using Huygens-Fresnel principle at their primary electrical resonant frequency, which is 684 kHz and 679 kHz, respectively.

According to Section 4.2, the lateral dimension is different for two designs, which is 9.0 mm for the SC fractal composite and 7.0 mm for the conventional composite. Due to the difference in lateral dimension and microstructure between two composite designs, the natural focal point of the SC fractal and the conventional composite is observed at 10.4 mm and 6.2 mm, respectively in Figure 4-16. It can be noticed from the Figure 4-16, there are two strong side lobes in the SC composite beam profile, which might be produced by the medium sized pillar at fractal generation Level II. In order to evaluate and compare the side lobe level of two composite designs, the directivity function of both composites is their far field (50 mm) is plotted in Figure 4-17.

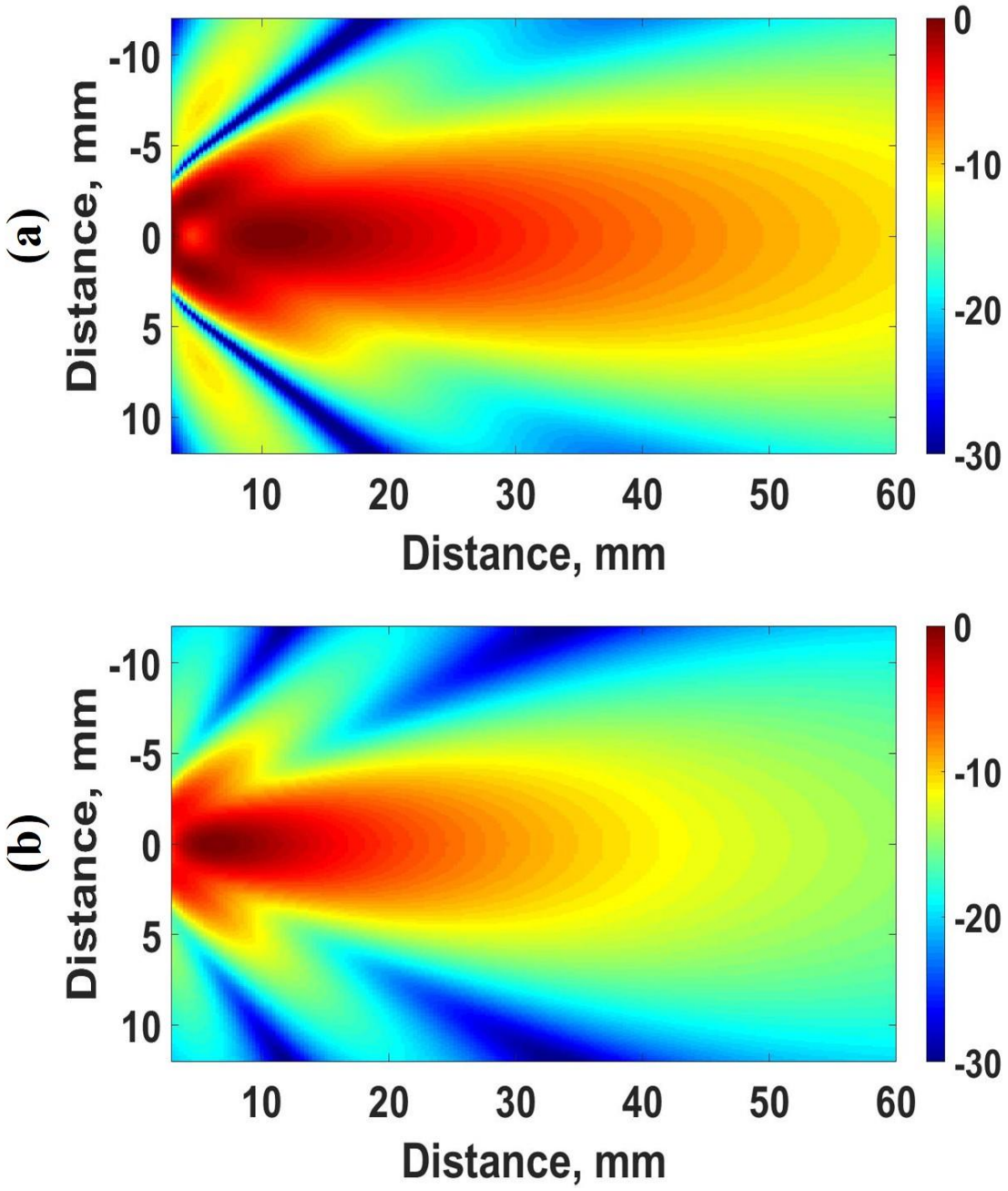

Figure 4-16: Simulated beam profile of: (a) SC composite; (b) Conventional composite

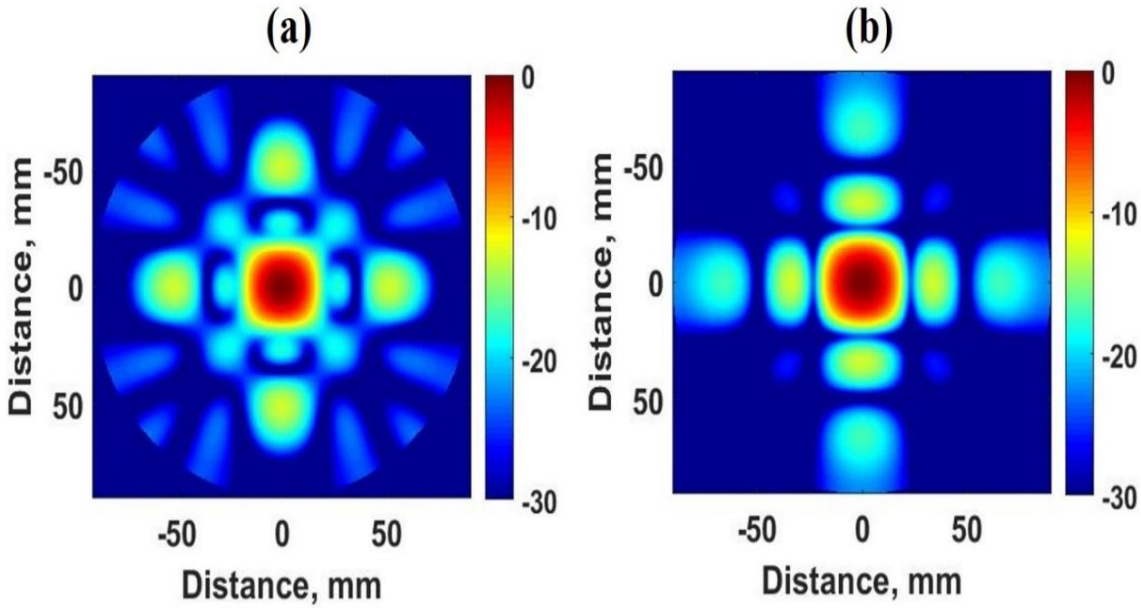

Figure 4-17: Directivity function at far field point of: (a) SC composite;(b) Conventional composite

It can be observed in Figure 4-17, in far field, the side lobe distribution is different between two composites, where the conventional 1-3 composite has fewer sidelobes when compared with the SC fractal composite. However, side lobe level for the SC and conventional composite are both -13 dB, with no improvement gained by using the SC design. This result differs from what has been achieved in Chapter III, in which the fractal designs demonstrated improved directivity compared to conventional designs.

4.4. Piezoelectric Composite Design Using SC Fractal Electrode

In this Section, the SC fractal geometry is used as the electrode pattern, shown in the Figure 4-18 (a), and applied on a conventional 1-3 composite which was designed earlier

in this Chapter. For comparison, this 1-3 conventional composite is fully electrode, which can be shown in Figure 4-18 (b).

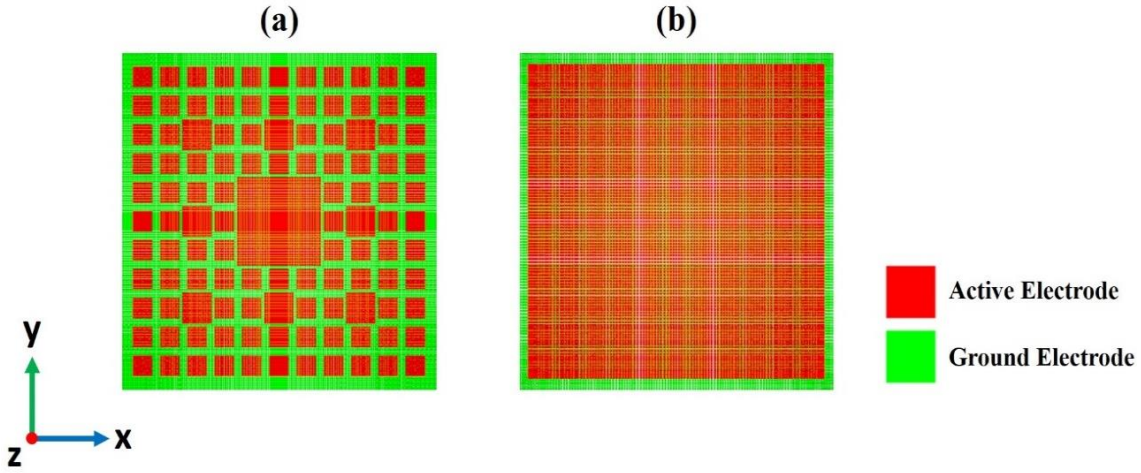

Figure 4-18: Electrode pattern applied to a conventional 1-3 composite design: (a) SC fractal electrode configuration; (b) Full electrode configuration

The predicted TVR and OCV response from the FE model of both electrode configurations is shown in Figure 4-19 and Figure 4-20, respectively.

The results shown in Figure 4-19 and Figure 4-20 indicates that applying SC electrode pattern on a conventional composite would not improve the performance of the composite when compared to the standard condition when the composite is fully electrode. In the TVR spectrum, the peak gain of the composite with SC fractal electrode and full electrode is 155.3 dB and 155.5 dB, respectively and the -6 dB bandwidth is 51.3 % and 58.5 %, respectively. In the OCV spectrum, the composite with SC fractal electrode has the peak gain of -185.7 dB and -6 dB bandwidth of 22.3 %, where the composite with full electrode has the -185.2 dB peak gain and 22.3 % -6 dB bandwidth.

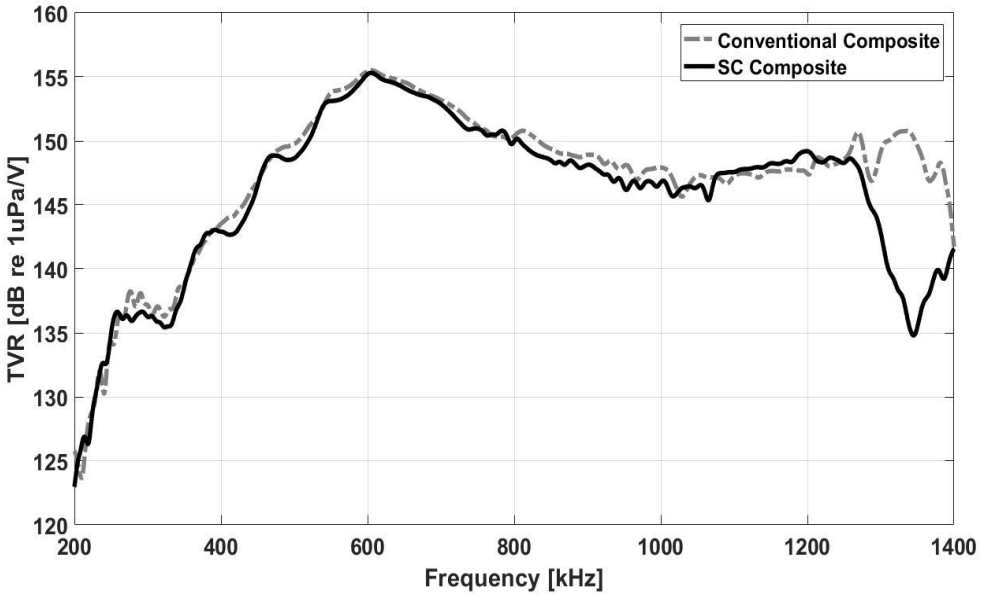

Figure 4-19: TVR spectrum of composite with full and SC fractal electrode patterns

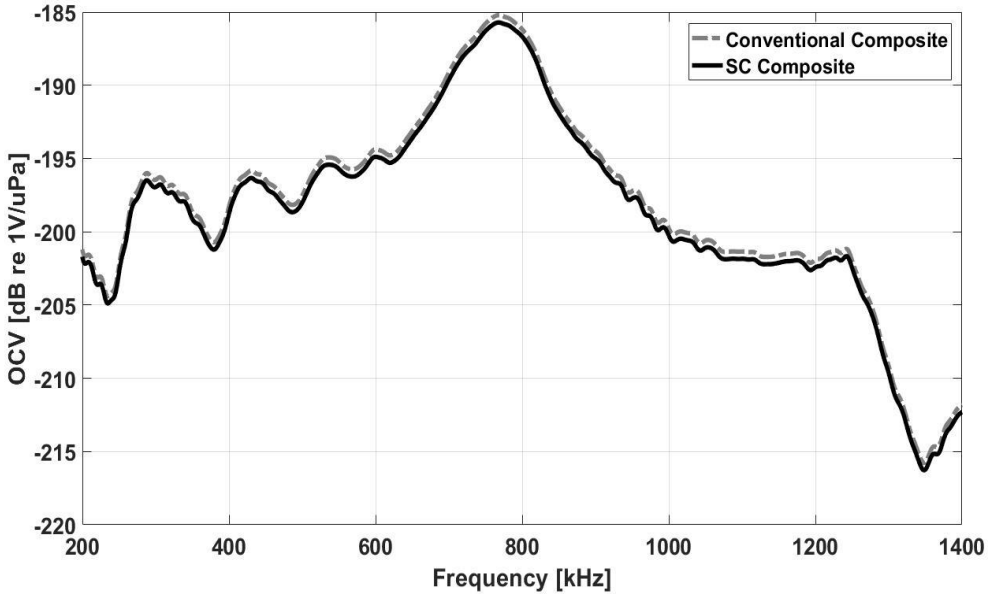

Figure 4-20: OCV spectrum of composite with full and SC fractal electrode patterns

This result is approximately same as with the SG fractal electrode pattern case in Chapter III. Hence, it can be surmised that the performance of the composite is not improved by using a fractal electrode pattern instead of a full electrode.

4.5. Conclusion and Future Work

In this Chapter, a second fractal geometry, SC, was studied using simulation only, in order to investigate a new composite design with improved bandwidth. Three parameter sweep simulations were conducted on key geometrical considerations for the microstructure, with an optimal SC fractal composite design proposed for performance evaluation. The operating characteristics of this SC composite were then assessed through simulated TVR, OCV and pulse-echo response and compared to an equivalent conventional 1-3 composite design. In one-way transmission mode and two-way pule-echo mode, both bandwidth and sensitivity of the device can be improved by incorporating a fractal microstructure. In one-way reception mode, designing a composite using a fractal geometry could result in a bandwidth enhancement but sensitivity will be lower, when compared with the conventional 1-3 composite. Moreover, the bandwidth and sensitivity performance of a conventional composite cannot be improved by using a fractal electrode configuration. Interestingly, these simulation results correlate well those highlighted in Chapter III for the SG fractal geometry case.

However, there is one different result presented in this Chapter, which is the side lobe of the composite with SC fractal geometry cannot be reduced, when compared to the conventional composite. In fact, the sidelobe activity in the far field is more wide spread

for the SC fractal device. This could be explained as that the characteristic of the beam profile is related to the property of the fractal geometry. As a result, it can be said that there is no guarantee that applying a fractal geometry on a composite design could lead to a reduction of side lobe level.

Lastly, the reason that the SC composite studied in this Chapter was not fabricated using the same method described in Chapter III is because the pillar in triangular shape can allow for a large pillar aspect ratio without a significant negative effect on transducer behaviour. As the result, a triangular pillar with larger lateral dimension can be prepared and placed into a 3D printed mould individually. However, the square pillar needs a smaller pillar aspect ratio for vibrational uniformly in thickness direction, which leads to the smallest pillar width of SC composite (0.5 mm) is much smaller than the SG composite (1.0 mm) described in Chapter III. The ceramic pillar with such fine scale is very difficult and time consuming to fabricate and hence, it was considered out of the scope for this PhD thesis. Nevertheless, the work described in Chapter III has provided a proof of the concept regarding the enhanced operational performance which can be achieved by fractal composite microstructures when compared to an equivalent standard 1-3 composite. Hence, there is confidence in the simulation results presented here and their potential to be realized in a fabricated device in the future.

For example, an advanced manufacturing technique like, 3D printing or high precision laser cutting could be used to fabricate a SC composite configuration and it could eventually be possible to produce a microstructure with a much higher fractal generation level, i.e. with much finer scale piezoceramic elements.

CHAPTER V

LINEAR ULTRASONIC ARRAY DEVELOPMENT INCORPORATING CANTOR SET FRACTAL GEOMETRY

In Chapter III and IV, two single element piezoelectric composite transducers were developed using the Sierpinski Gasket (SG) [115] and Sierpinski Carpet (SC) fractal geometry, respectively, to introduce substructures with varying length scales. These two single element fractal composite transducers exhibited a larger bandwidth in both transmission and reception modes of operation when compared to corresponded equivalent conventional parallelepiped 1-3 composite designs. However, due to fabrication challenges, only the SG fractal composite transducer was fabricated, and it is difficult to extend this single element SG fractal composite design to an array transducer. Subsequently, in this Chapter, another fractal geometry known as the Cantor Set (CS) will be used to design and fabricate a 2-2 fractal composite which can be manufactured easily using the conventional 'dice-and-fill' technique [65].

First of all, the design space of this CS fractal array is explored using the FE modelling approach. A series of parameter sweep simulations are performed to design a CS fractal array transducer and a conventional array transducer with optimized performance.

Subsequently, two 24-element array devices, one with the CS fractal geometry at fractal generation Level II and the other with conventional 2-2 connectivity configuration, are fabricated using the 'dice-and-fill' technique. The experimental performance of the fabricated active layer and each individual element, both CS and conventional 2-2 array, is characterized and compared. The surface dilation characteristic and the crosstalk performance of both array devices are measured using a 3D laser doppler vibrometer. Moreover, the imaging and defect sizing capability of the two arrays is then evaluated by employing full matrix capture (FMC) and the total focusing method (TFM) with a wire-water phantom.

The output of this Chapter has been published as two conference papers in International Ultrasonic Symposium [122], [123] and will be combined as a journal paper in the near future.

5.1. Cantor Set Fractal Geometry

An iteration rule for defining the features of the CS fractal geometry was developed in terms of a scaling factor, k (where $0 < k < 0.5$). As shown in Figure 5-1, a CS fractal geometry of total length L_0 at generation Level 0 is iterated to the next generation level with the scaling factor, k. The geometrical feature of this CS fractal geometry at generation Level N can be determined by the value of S_n and L_n using Equations (5-1) and (5-2), respectively. The detail of the derivative for Equations (5-1) and (5-2) can be found in Appendix B.

$$S_n = L_0 \cdot k^n \tag{5-1}$$

$$L_n = L_{n-1} \cdot k, (n \geq 1) \tag{5-2}$$

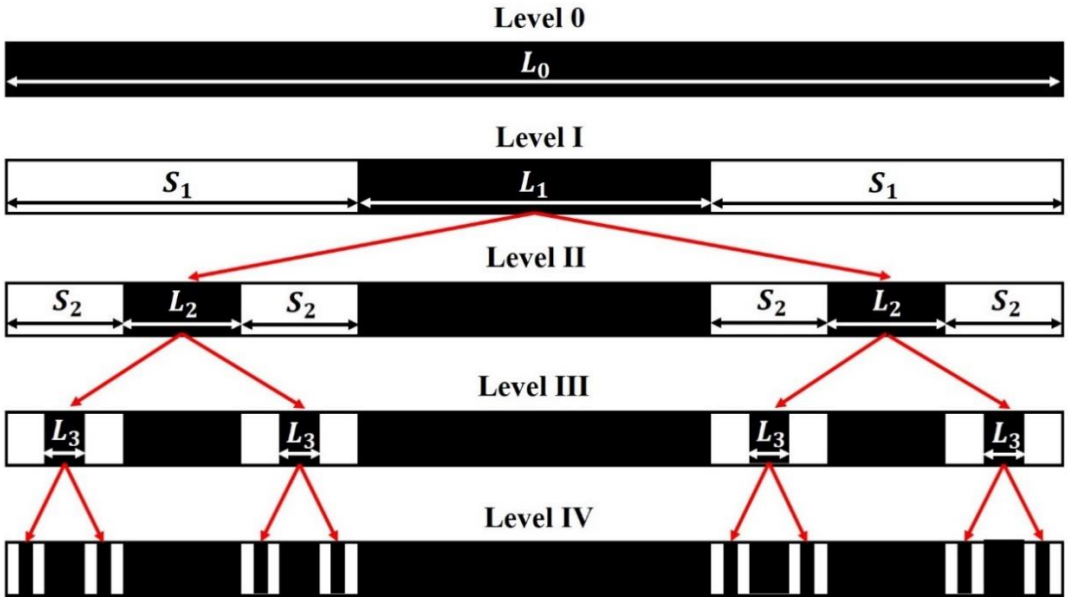

Figure 5-1: Schematic diagram of the first four fractal generation levels of the Cantor Set fractal geometry

5.2. Array Element Design Using Cantor Set Geometry

In order to explore the influence of adopting this CS fractal geometry as the structure of an array transducer, two FE models representing a single array element incorporating a fractal generation Level II CS fractal geometry and a conventional periodic 2-2 composite microstructure were developed, as illustrated in Figure 5-2 (a) and (b), respectively. The thickness of each array design is 1.5 mm, corresponding to an electrical resonance frequency of approximately 1 MHz. PZT-5H ceramic (Meggitt A/S, Kvistgard, Denmark) and hardset polymer (Robnor Resin Ltd, UK) are chosen to be the active phase and passive phase materials, respectively. In order to optimise the bandwidth performance of these two models, a number of parameter sweep simulations were performed. The mechanical Q-factor, introduced in Section 4.2, will be used again to indicate device bandwidth through spectral measurements of the conductance spectrum. The target here is to produce a design with a low value of the Q-factor to indicate that a broadband device can be realised.

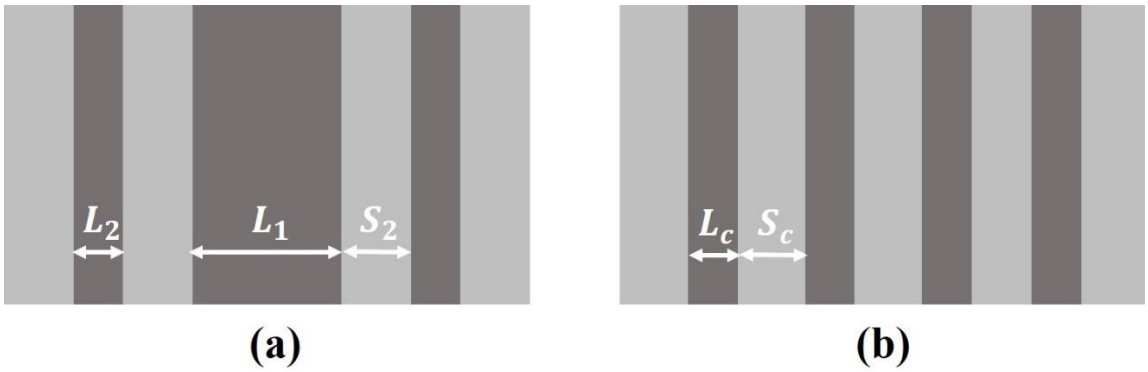

Figure 5-2: Schematic diagram of a single element within the array, (a) Level II CS fractal; (b) 2-2 composite (Dark grey: Ceramic; Light grey: Polymer)

5.2.1. Simulation Sweep I: Varying the Pillar Width

As illustrated in Figure 5-2 (a), the first parameter sweep simulation was performed by keeping the scaling factor, *k*, of one CS fractal array element to be 0.33, where a standard CS fractal geometry at fractal generation Level II can be obtained, then varying the value of the pillar width at the second generation level, L_2, from 0.1 mm to 1.0 mm with a step size of 0.05 mm. The resulting conductance spectra and Q-factor predictions for different values of L_2 are shown in Figure 5-3 and Figure 5-4, where the peak of each main lobe is marked with a red dot.

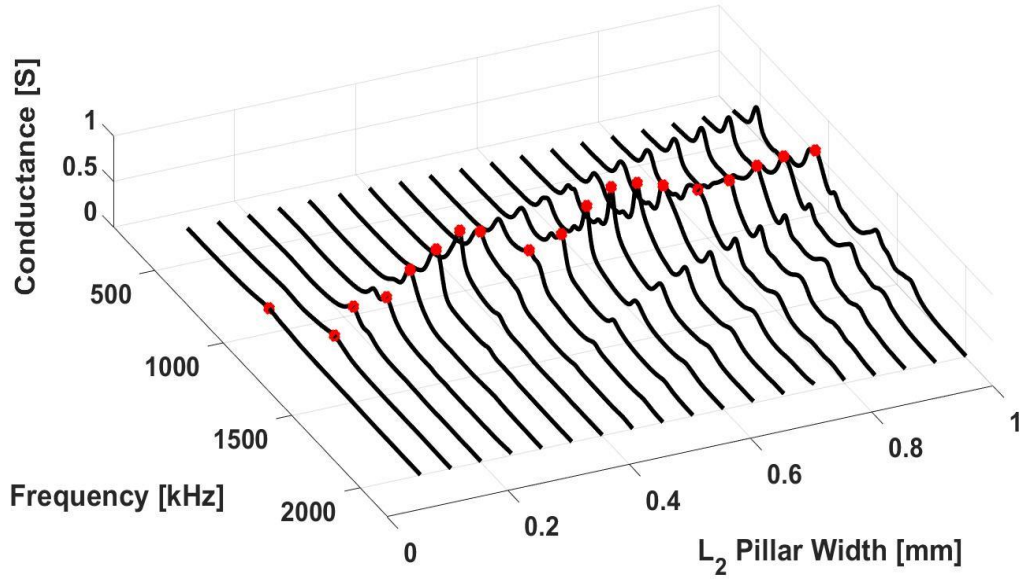

Figure 5-3: FE derived conductance spectrum for different values of L_2 in the CS fractal array design

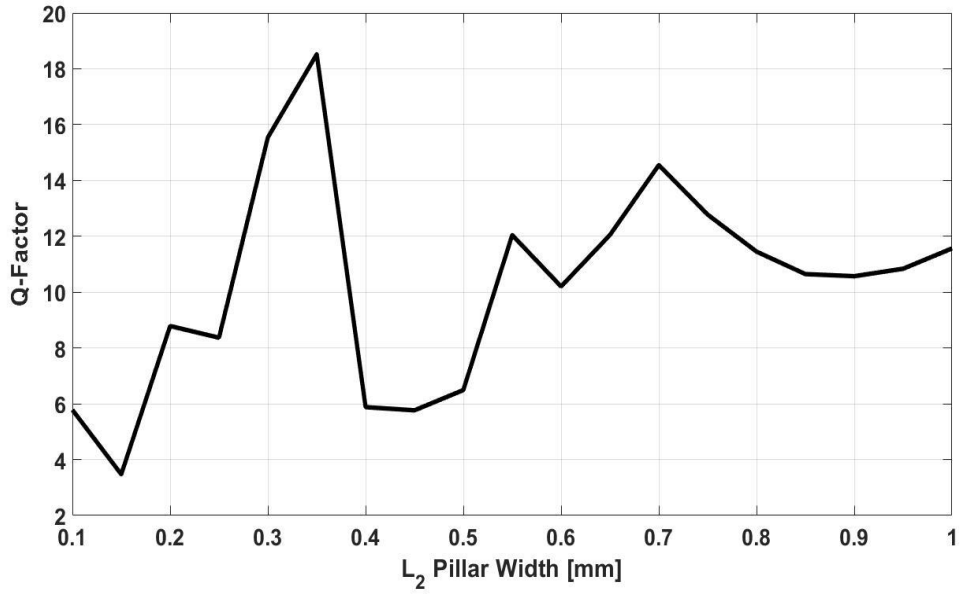

Figure 5-4: Q-factor for different values of L_2 in the CS fractal array design

From Figure 5-4, it can be identified that the lowest Q-factor value calculated from the main lobe of the conductance spectra can be achieved when L_2 is 0.15 mm, which means that the highest predicted bandwidth was obtained with this arrangement compared to other conditions. Another region of interest is for L_2 between 0.4 and 0.5, which represents another local minima in the Q-factor plot, although for this work the global minimum at 0.15 mm will be selected.

5.2.2. Simulation Sweep II: Varying the Scaling Factor

After determining a desired value of L_2, the second parameter sweep simulation was performed by fixing the value of L_2 to be 0.15 mm and varying the scaling factor, *k*, from

0.2 to 0.4 with a step of 0.01. The resulting conductance spectra and Q-factor predictions for each different scaling factor, *k*, are shown in Figure 5-5 and Figure 5-6.

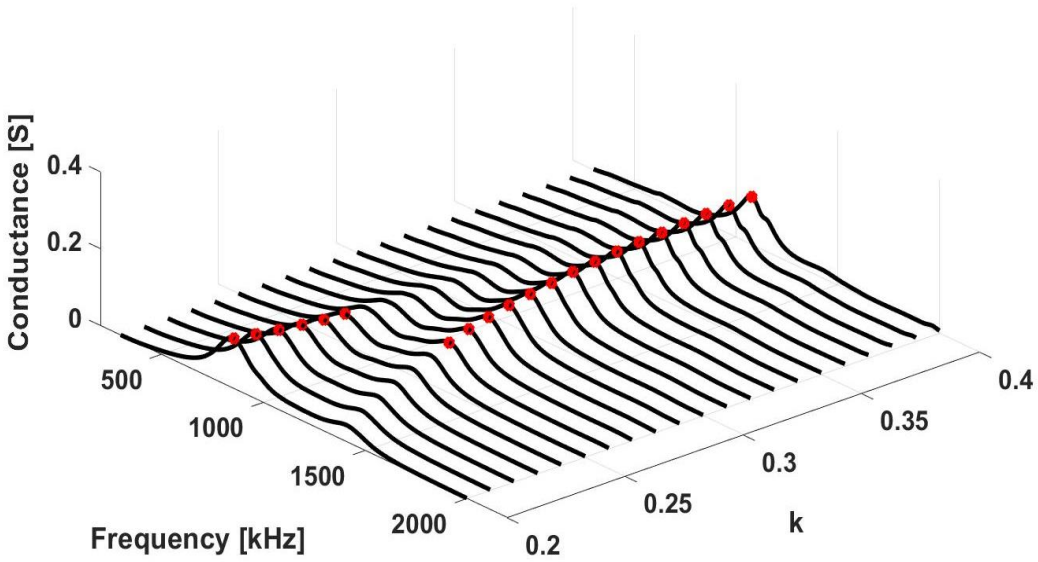

Figure 5-5: FE derived conductance spectrum for different values of k in the CS fractal array design

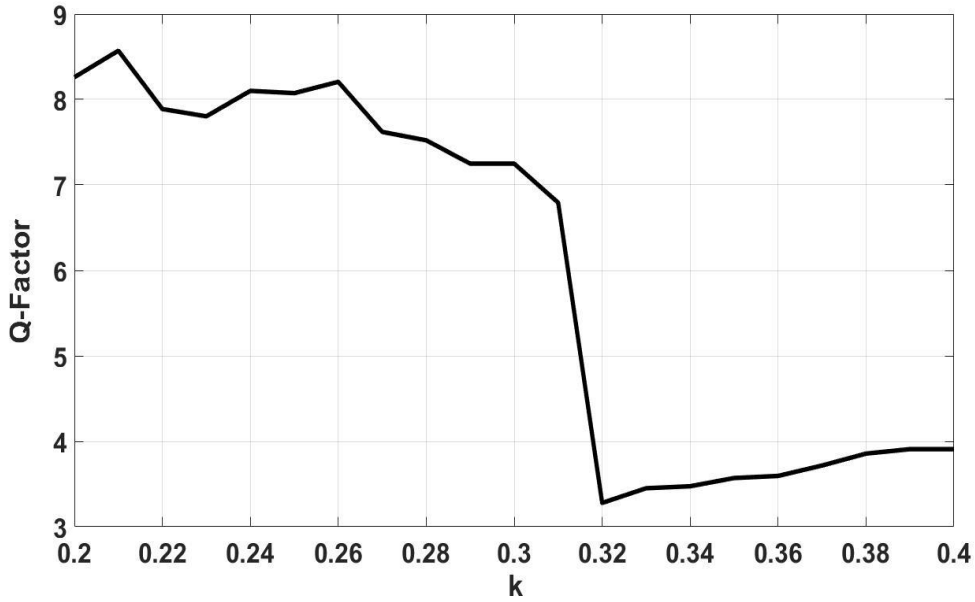

Figure 5-6: Q-factor for different value of k in the CS fractal array design

In Figure 5-6, it is observed that when *k* equals 0.32, the lowest Q-factor calculated from the conductance main lobe can be obtained and this value will be used in the next simulation stage. It should be noted that all values of *k* above 0.32 could be considered as appropriate for a wide bandwidth design.

5.2.3. Simulation Sweep III: Varying the Saw Width

The last parameter sweep simulation determines an optimal design for the conventional 2-2 composite array element. By setting the value of the pillar width of one conventional array element, L_c, as shown in Figure 5-2 (b), to be 0.15 mm, which is the same as L_2 in the CS fractal design, then varying the saw width, S_c, from 0.1 mm to 0.3 mm, with a step size of 0.05 mm, the resulting conductance spectra and the Q-factor predictions are shown in Figure 5-7 and Figure 5-8.

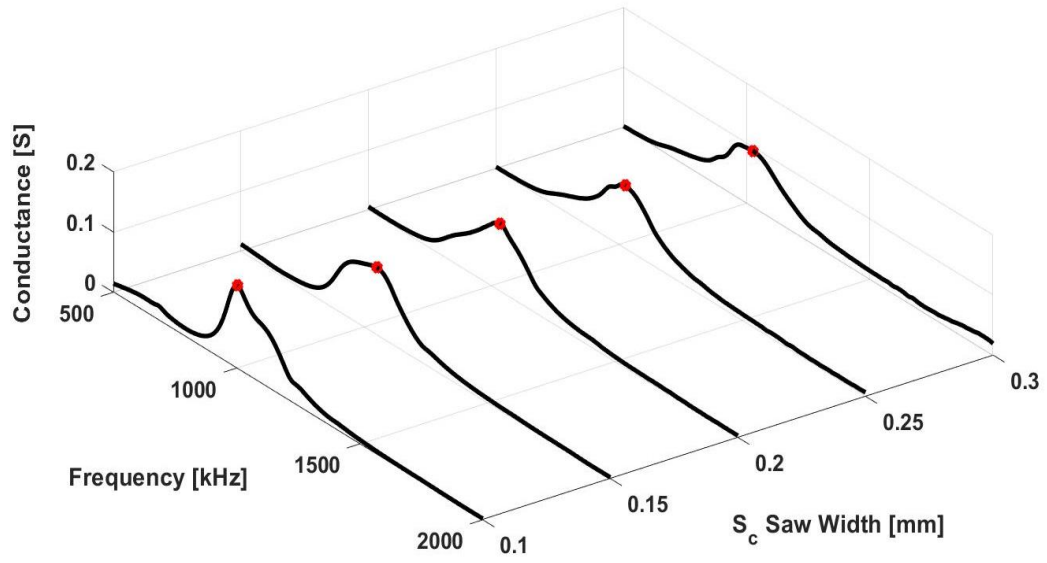

Figure 5-7: FE derived conductance spectrum for different values of the saw width, S_c, in the conventional array design

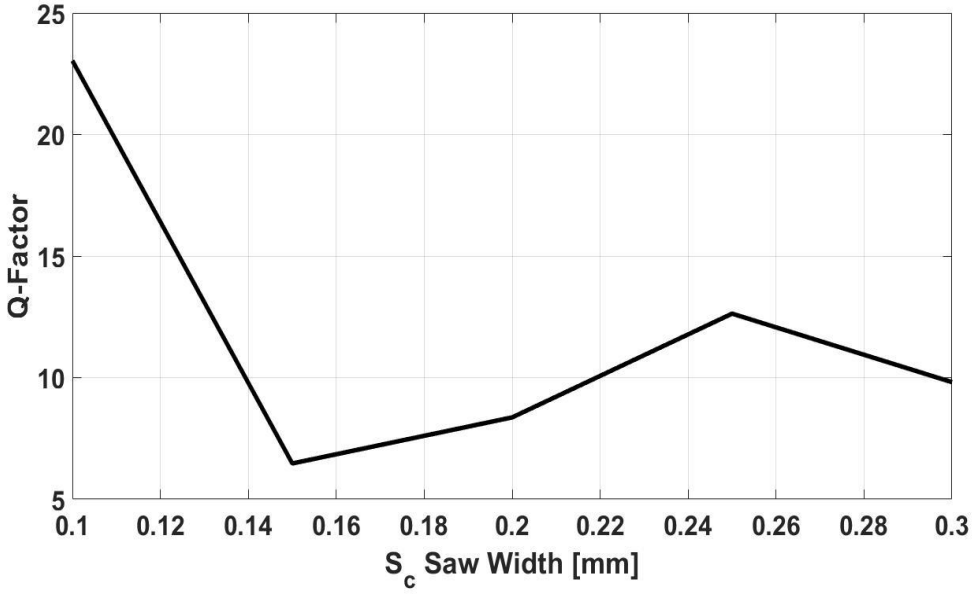

Figure 5-8: Q-factor for different values of the saw width, S_c, in the conventional array design

As illustrated in Figure 5-8, the highest bandwidth for the conventional 2-2 array element to be used for this work can be achieved when the saw width equals 0.15 mm.

5.3. Array Single Element Performance Modelling

The parameter simulation sweeps have produced 2-2 composite microstructures designed for maximised bandwidth, for both the CS fractal and the conventional linear array element, which are shown in Figure 5-9. For the CS fractal array design, the scaling factor, *k*, and the pillar width at the second generation Level, L_2, were set to be 0.32 and 0.15 mm respectively, where the pillar width at the first generation Level, L_1, and saw width, S_2, was calculated to be 0.47 mm and 0.15 mm respectively. For the conventional array design, the pillar width, L_c, and the saw width, S_c, were both determined as 0.15 mm. Both

designs have a similar ceramic volume fraction, which is 58.5 % for the CS fractal array design and 50.0 % for the conventional design. The materials selected for the active and passive phase is PZT5H ceramic (Meggitt A/S, Kvistgard, Denmark) and hardset polymer (Robnor Resin Ltd, UK), respectively for both devices.

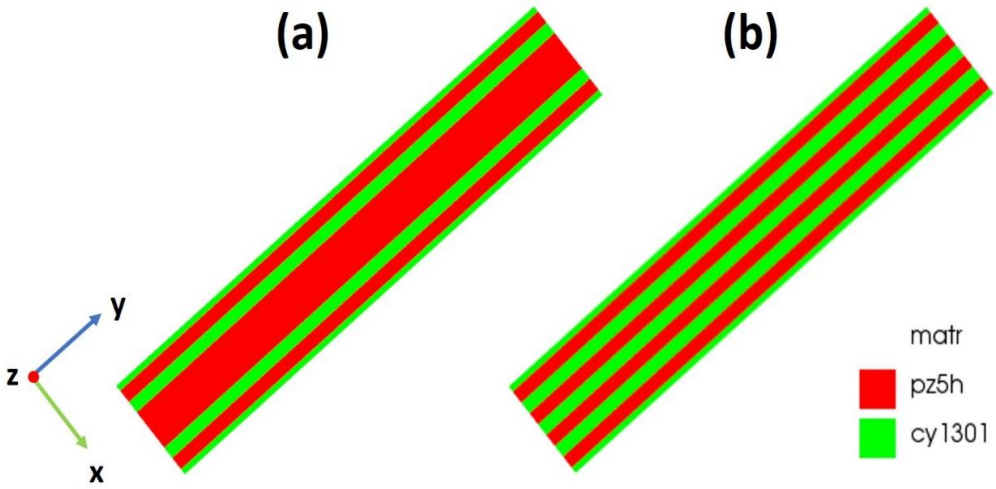

Figure 5-9: FE model of a single array element within the:(a) Level II CS fractal array; (b) conventional 2-2 array

5.3.1. Electrical Impedance

The electrical impedance magnitude spectra of one element without matching and backing in each array design was simulated and is shown in Figure 5-10. It can be seen that there are two permanent resonant modes marked with red circles exhibited in the CS fractal array element, which are located at impedance minima frequencies of 817 kHz and 1086 kHz. For the conventional array design with a uniform structure, one dominant resonant mode is evident and occurs at a frequency of 1040 kHz.

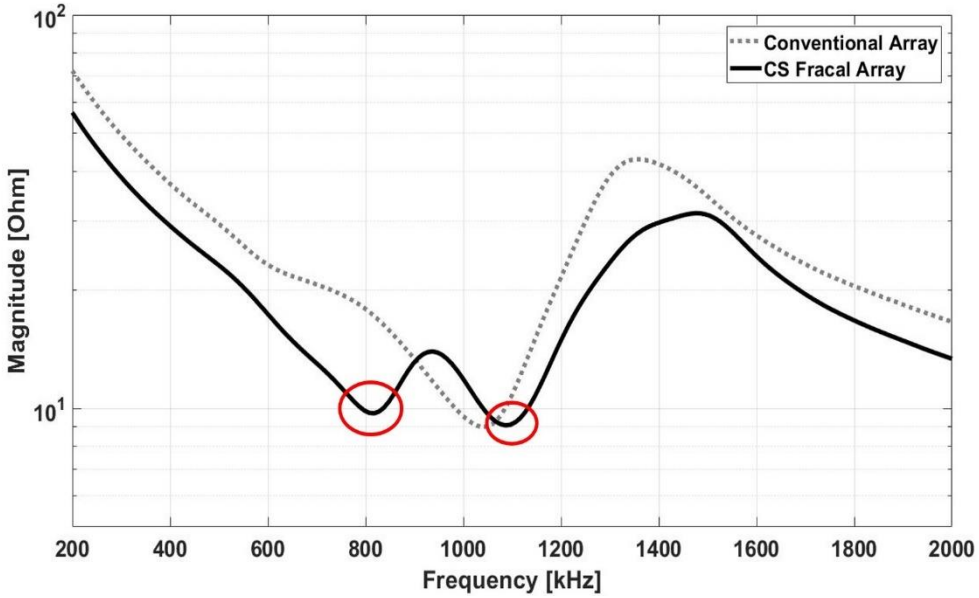

Figure 5-10: FE derived electrical impedance magnitude spectrum of the CS and conventional array element

5.3.2. Vibrational Mode Analysis

Following the electrical impedance analysis of the CS and conventional array element, the displacement mode shape at each resonant frequency of one array element from each array configuration was investigated, where the displacement along the thickness direction seen from the x-z plane is shown in Figure 5-11. In order to compare the strength of each mode, all thickness displacement data plotted in Figure 5-11 were normalized with the maximum displacement value of the unique resonant mode of the conventional array element shown in Figure 5-11 (c). It should be noted that the vibrational characteristics of the piezoceramic material only is represented in this diagram to facilitate ease of comparison of the performance of the active material in each case.

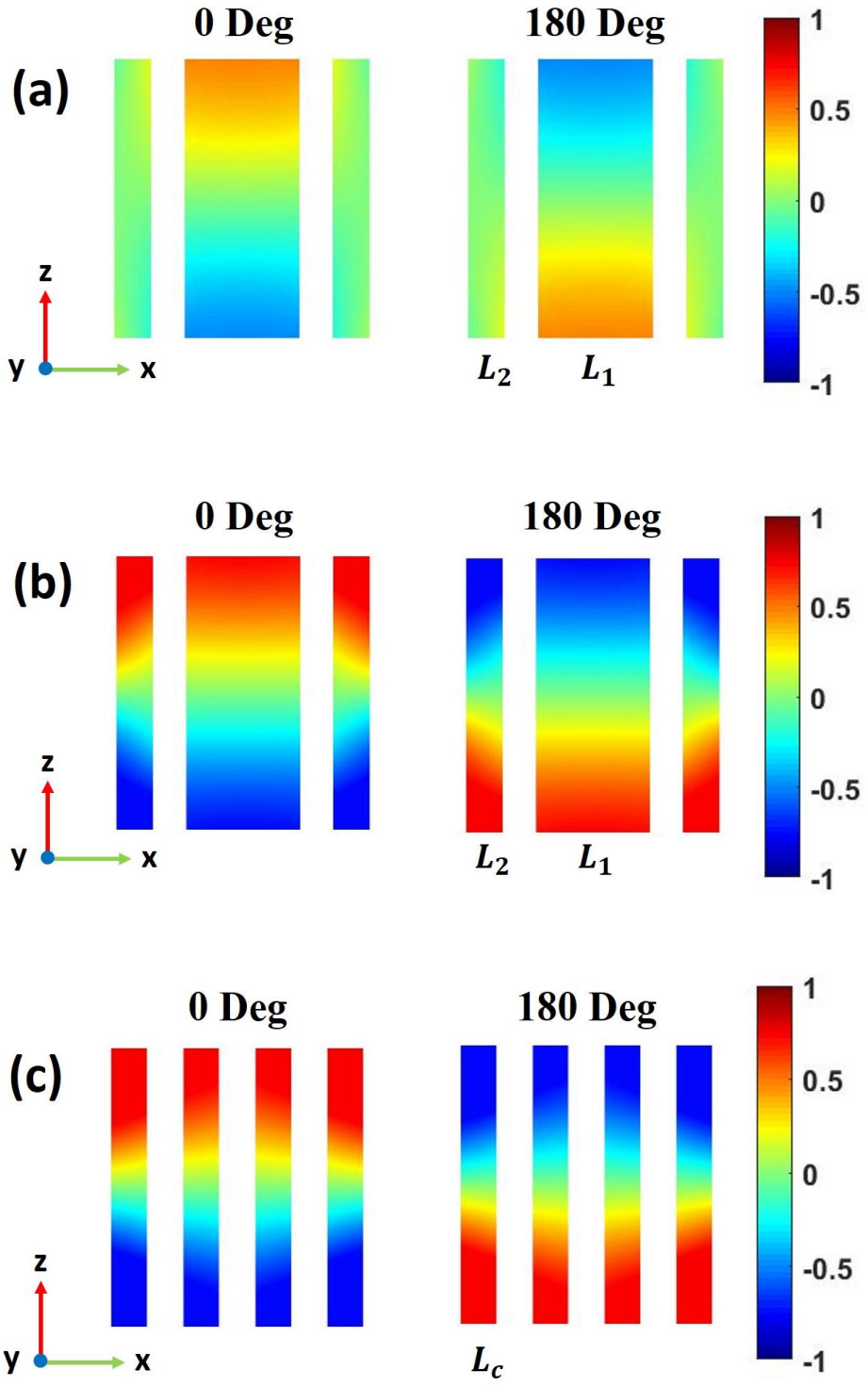

Figure 5-11: Array element thickness displacement mode shape of (a) CS fractal array at 817 kHz; (b) CS fractal array at 1086 kHz and (c) conventional array at 1040 kHz

It can be seen from Figure 5-11 (a), at the first resonant frequency of the CS fractal array element, 817 kHz, a thickness mode vibration characteristic can be seen in the pillar in the first fractal generation level. As shown in Figure 5-11 (b), at the second resonant frequency of the CS fractal array element, 1086 kHz, a strong thickness vibration behaviour can be found in both the first and second fractal generation level pillars. Consequently, 1086 kHz is considered to be the main thickness resonance frequency of the CS fractal array element. For the conventional array design in Figure 5-11 (c), at its only resonant frequency of 1040 kHz, all the ceramic pillars vibrate uniformly and in phase along the thickness direction.

5.3.3. Lamb Wave Dispersion in CS and Conventional Array Design

It is well known that the mechanical crosstalk of an ultrasound array configuration mainly originates from the Lamb wave propagating across the active aperture of the array [124]. The Lamb wave mode is directly related to the centre-to-centre spacing of the array elements in terms of its wavelength. In order to have a further understanding about the vibration behaviour of both array designs, the dispersion properties of both array designs were studied in this Section using FE models. The schematic of a 2-D FE model for analysing the dispersion property of an array with 2-2 connectivity is shown in Figure 5-12.

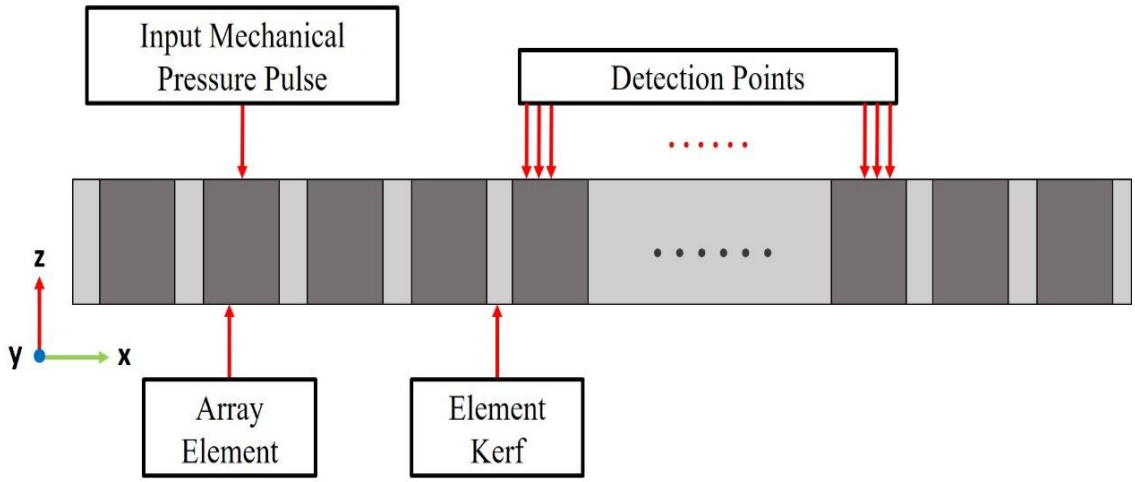

Figure 5-12: Schematic of FE model for investigating the dispersion property of an array with 2-2 connectivity

Each array element shown in Figure 5-12 correlates to a CS fractal or conventional 2-2 array element, as designed in this Chapter. The array was excited by a wideband mechanical pressure pulse on the surface of the array material. The time history displacement data, in both the thickness direction (z-axis) and lateral direction (x-axis), in response to the impulsive excitation at the array surface were recorded at each detection point (every mesh node) across the array aperture. This predicted spatial time domain displacement data was then processed by utilising the 2D FFT approach, where the dispersion characteristics of the CS fractal and conventional linear array configuration can be obtained as the Lamb wave phase velocity with respect to frequency, as shown in Figure 5-13.

Three modes have been identified as the zero-order asymmetrical lamb mode, a_0; the zero-order symmetrical lamb mode, s_0, and the first-order symmetrical lamb mode, s_1. It

can be seen in Figure 5-13 that the stopband of the a_0, s_0 and s_1 mode is much lower for the CS array design compared to the conventional design.

In order to investigate the influence of these three modes on an array design, an operating load line was plotted as a dash line in both characteristics, as shown in Figure 5-13. This load line corresponds to a constant wavelength and defines the array centre-to-centre element spacing, which is 1.22 mm for the CS fractal array and 1.20 mm for the conventional array. In Figure 5-13 (a), the load line only intersects with the dispersion data at 1150 MHz, which corresponds to the s_1 mode. The mode strength at this frequency was evaluated as -35.3 dB according to the magnitude of the resulting 2D FFT coefficient. However, in Figure 5-13 (b), the load line intersects with the dispersion curve at three frequencies, 630 kHz, 1050 kHz and 1338 kHz, which corresponds to the, a_0, s_0 and s_1 mode, respectively. The strength of these modes at each frequency was then calculated as -7 dB, -2.6 dB and -10.1 dB, respectively.

By recalling the impedance characteristics of both array configurations in Section 5.3.1 and considering the mode strength of each Lamb wave mode, it can be concluded that the CS fractal array is weakly coupled with the s_1 mode. However, for the conventional array, the s_0 and s_1 modes are strongly coupled with its thickness mode as a result of the regular periodic array structure. This could result is a higher cross talk level, which will be experimentally measured later in Section 5.5.3.

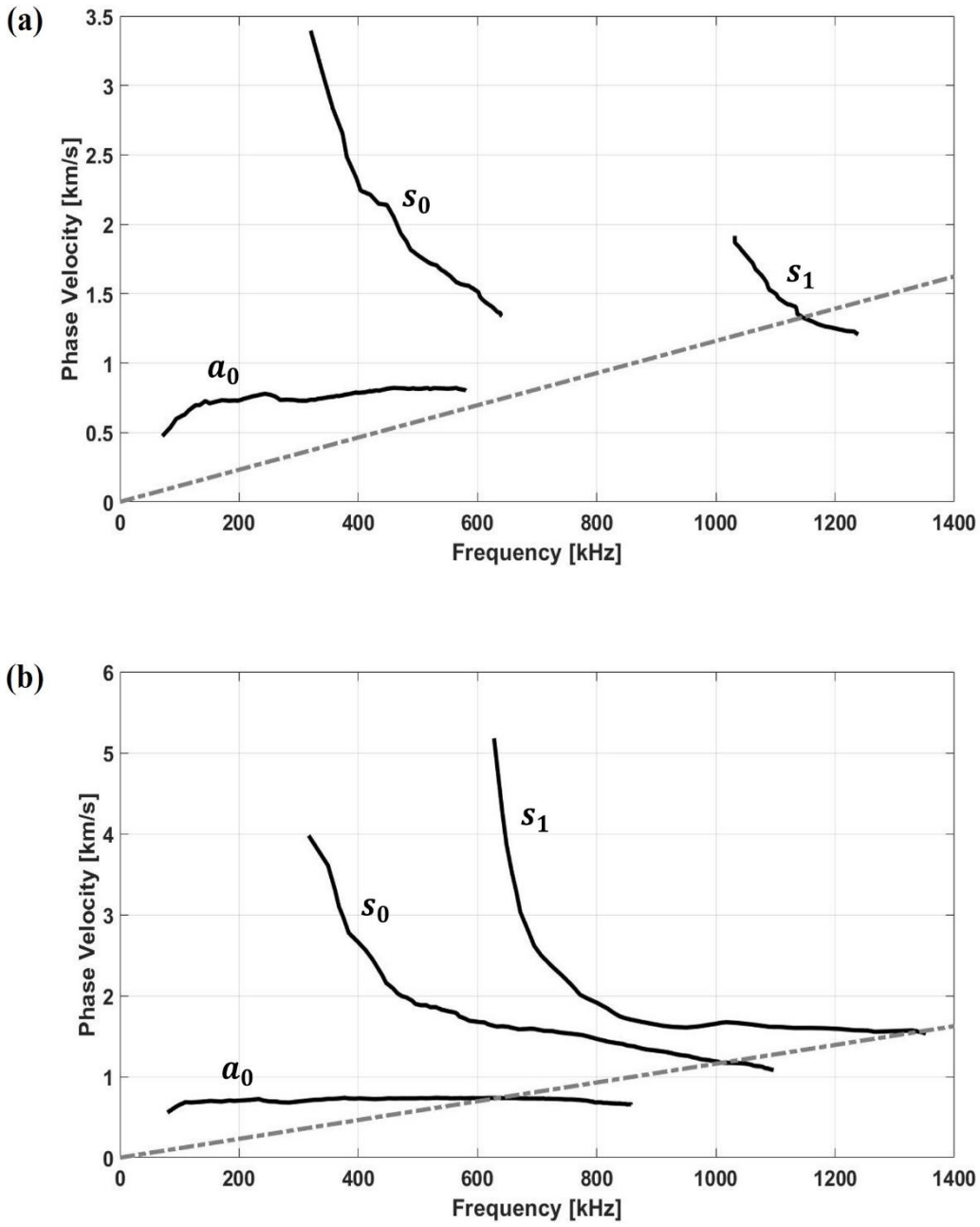

Figure 5-13: Dispersion characteristics of: (a) CS fractal array; (b) conventional linear array.

5.3.4. Matching and Backing Layer Design

A dual matching layer scheme was used to couple this array to a water load. The same design process as described in Section 3.2.2.3 was used and the same materials selected: CY221/HY956EN medium set polymer (Robnor Resin Ltd, UK) was used for Matching Layer I; and hard setting polymer (Robnor Resin Ltd, UK) filled with 3 μm alumina powder using 70 % weight fraction was used for Matching Layer II. According to the specification of the CS fractal and conventional array element design, the acoustic impedance calculated using the Smith-Auld approach [57] according to the ceramic volume fraction of the composite and constituent material properties is 16.8 MRayl and 14.4 MRayl for the CS fractal array and conventional array, respectively. As the result, the thickness of Matching Layer I and II was calculated as 344 μm / 521 μm for the CS array and 386 μm / 511 μm for the conventional 2-2 array. Moreover, according to the backing material design rule introduced in Section 2.2.1, a hard setting polymer filled with tungsten power, using a 24 % weight fraction, has the acoustic impedance of 8.61 MRayl, which is close to half of the acoustic impedance of the active layer. This backing material was incorporated at the rear face of both array designs, with a thickness of 30 mm, which can provide an attenuation around 30 dB at the back of the array transducer.

5.3.5. Pulse-Echo Response Modelling

At this stage, the design process of a CS fractal and a conventional 2-2 array is completed. The specifications of the design parameters for both arrays are summarized in Table 5-1.

Table 5-1: Design specifications of the CS fractal and conventional 2-2 array

<table>
<tr><th></th><th colspan="2">CS Fractal Array</th><th>Conventional Array</th></tr>
<tr><td>Active Layer Material</td><td colspan="3">PZT-5H Ceramic & Hardset Polymer</td></tr>
<tr><td rowspan="2">Pillar Width(s) (mm)</td><td>Level I</td><td>Level II</td><td rowspan="2">0.15 mm</td></tr>
<tr><td>0.47 mm</td><td>0.15 mm</td></tr>
<tr><td>Saw Width (mm)</td><td colspan="2">0.13 mm</td><td>0.15 mm</td></tr>
<tr><td>Thickness (mm)</td><td colspan="3">1.5 mm</td></tr>
<tr><td>VF (%)</td><td colspan="2">58.5 %</td><td>50 %</td></tr>
<tr><td rowspan="2">Matching Layer I</td><td colspan="3">Medium Set Polymer</td></tr>
<tr><td colspan="2">344 μm</td><td>386 μm</td></tr>
<tr><td rowspan="2">Matching Layer II</td><td colspan="3">Hardset polymer filled with 3 μm calcined alumina powder by 70 % weight fraction</td></tr>
<tr><td colspan="2">521 μm</td><td>511 μm</td></tr>
<tr><td rowspan="2">Backing Layer</td><td colspan="3">Hardset polymer filled with tungsten powder by 24 % weight fraction</td></tr>
<tr><td colspan="3">30 mm</td></tr>
</table>

The far-field pulse-echo response of an array element incorporating the matching and backing layers was simulated in a water load using PZFlex for both array designs. The results are shown in Figure 5-14 (a) and (b) and Table 5-2.

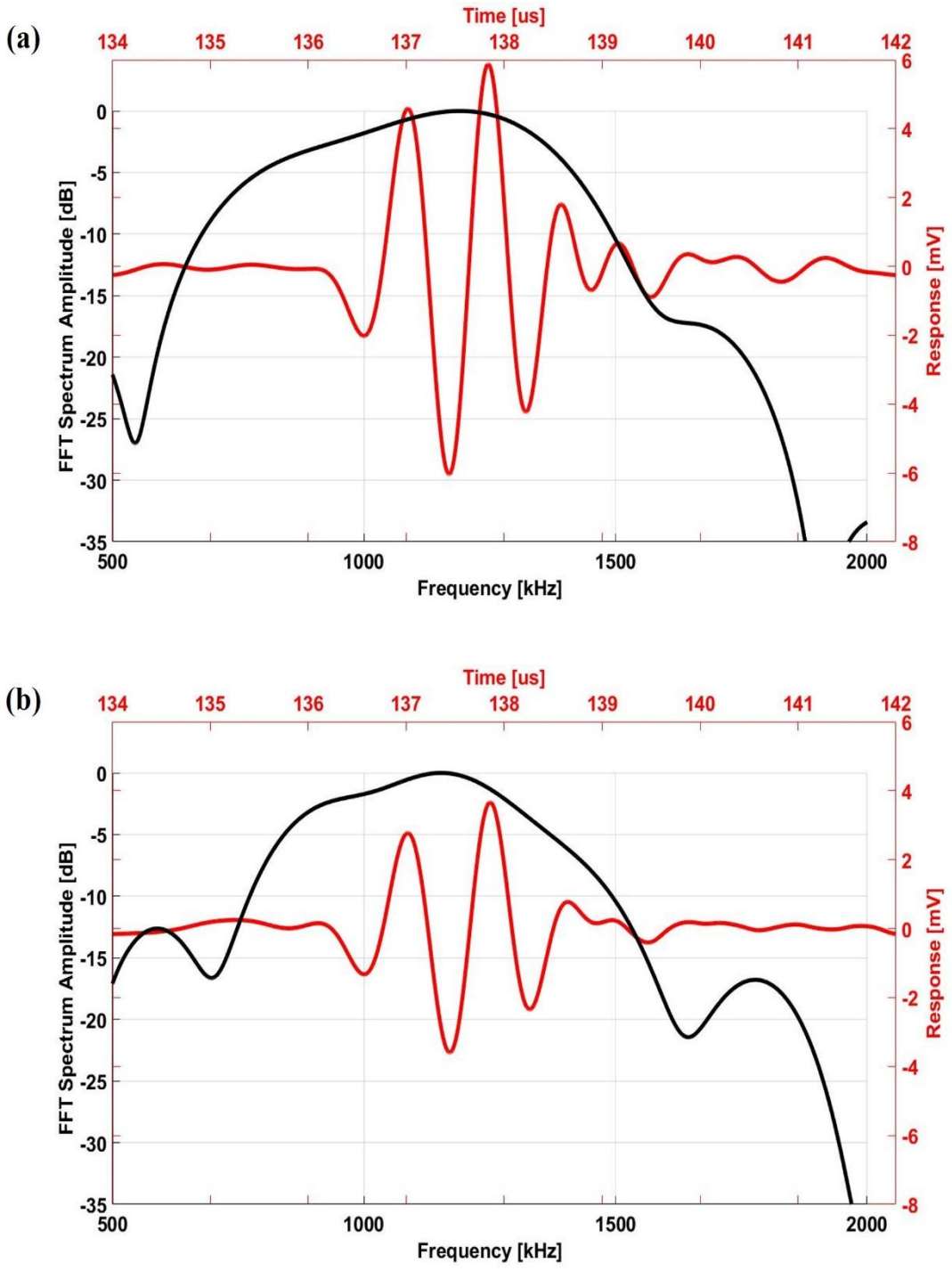

Figure 5-14: Simulated pulse-echo time-domain waveform and frequency spectrum: (a) CS fractal array (b) conventional linear array.

Table 5-2: Pulse-echo modelling results summary

	V_{p-p}	-6 dB Bandwidth
CS Fractal Array Element	11.9 mV	56.7 %
Conventional Array Element	7.3 mV	50.0 %

From Figure 5-14 and Table 5-2, a 13.4 % bandwidth improvement has been achieved by the CS fractal array element, with respect to the conventional 2-2 array element. As for the sensitivity, the peak-to-peak received voltage, V_{p-p}, of the CS fractal array element is 63.0 % higher than the conventional array element. Therefore, the figure of merit, sensitivity bandwidth product (SBP) defined as the product of peak-to-peak voltage and -6dB bandwidth is 8.0 kHz·V for the CS fractal array element against 4.2 kHz·V for the conventional 2-2 device, where an improvement of 90.5 % can be achieved by the CS fractal array element.

5.3.6. Beam Profile Modelling

The beam forming capability in a water load of each array, both with 24 elements, was evaluated and compared using an FE modelling approach. Figure 5-15 (a) and (b) display the simulated beam profiles of the CS fractal array transducer and the conventional array transducer, when both devices were focused on the central axis, at a distance of 15 mm away from the front face of the device. It can be seen from Figure 5-15 that the side lobe of the CS fractal and conventional array is -30 dB and -21 dB, respectively, where a 9 dB

side lobe reduction was achieved by this CS fractal array design, compared to its equivalent conventional 2-2 configuration. However, the focusing ability of the conventional 2-2 array is slightly better than the CS fractal array, where the -3 dB focal zone area is 11.76 mm × 1.52 mm for CS fractal array and 9.93 mm × 1.44 mm for conventional 2-2 array.

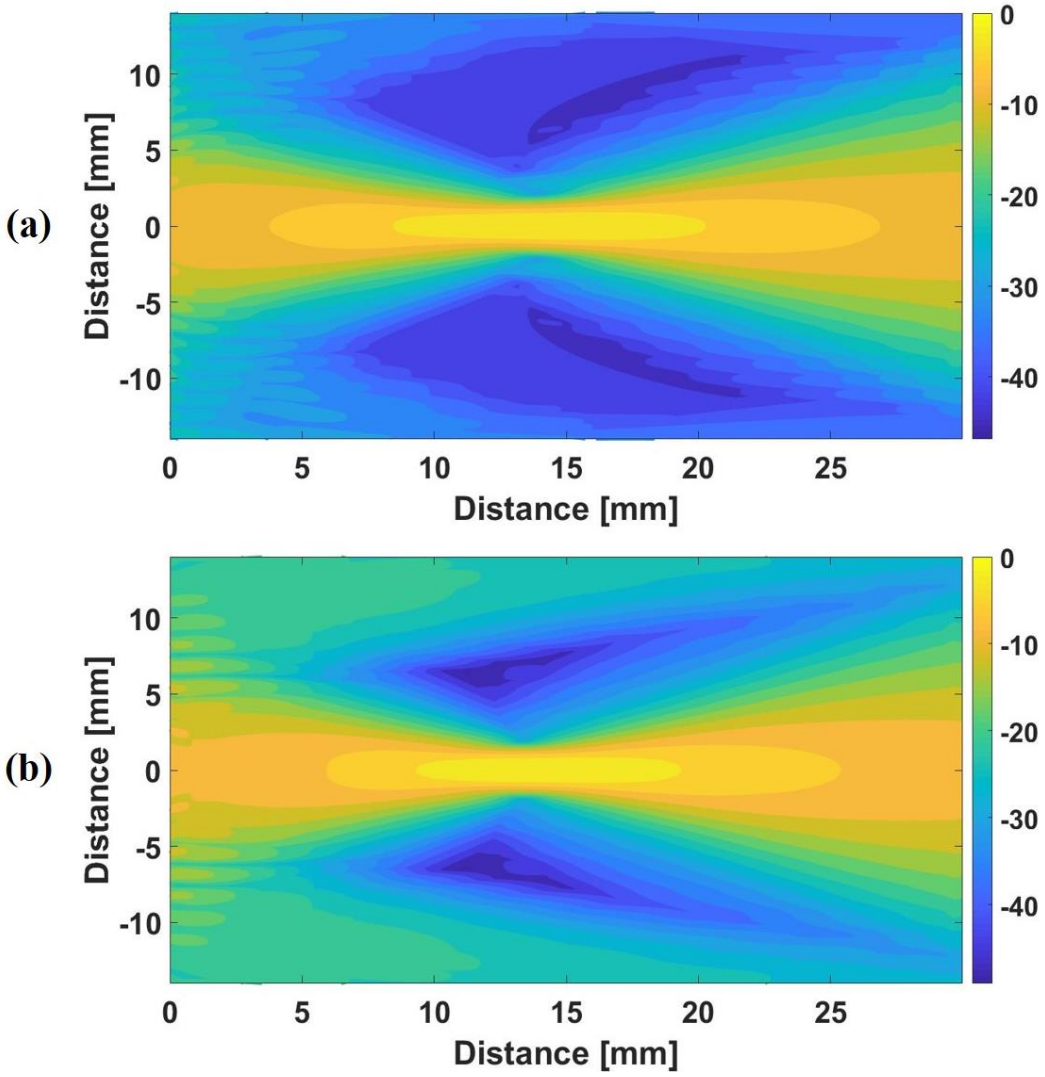

Figure 5-15: FE simulated beam profile, (a) CS fractal array (b): Conventional array (Focused at 15 mm)

5.4. Cantor Set Array Fabrication

5.4.1. CS Fractal Array Active Layer Manufacturing

The 2-2 composite active layers for both the CS fractal array and the conventional array design were fabricated using the traditional 'dice-and-fill' technique. However, because there are two different sizes of pillars in the CS fractal array composite active layer, three groups of cuts, represented by three different colours, as shown in Figure 5-16, were needed to fabricate this CS fractal composite substrate plate, with all three groups of cuts sharing the same pitch value, 1.22 mm.

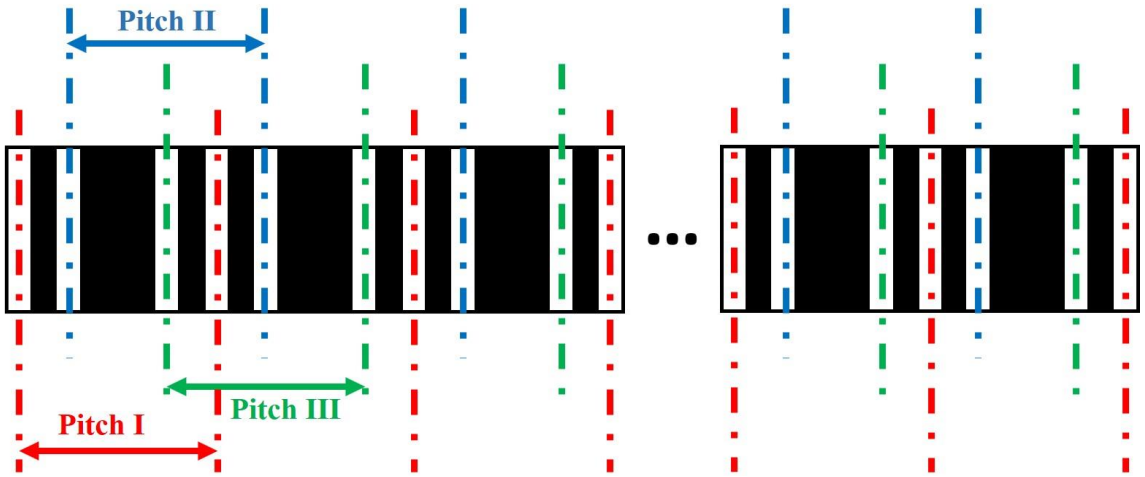

Figure 5-16: Schematic of fabricating CS fractal array composite active layer

5.4.2. CS Fractal Array Assembly

The electroded composite active layers of the CS fractal array and the conventional 2-2 array are shown in Figure 5-17 (a). The scratch dicing technique was utilised for element

electrical isolation, where 24 linear elements were defined for each array device and a flexible printed circuit board (PCB) was employed for electrical interconnection, also shown in Figure 5-17 (a). The schematic of the flexible PCB is attached in Appendix C of this thesis. In Figure 5-17 (b), a dual matching layer was cast onto the transducer front face via a two-pass process using an adjustable blade and then the damping material was added at the rear face of each device, as discussed in Section 5.3.4. The fabricated CS fractal and conventional linear array are shown in Figure 5-17 (c).

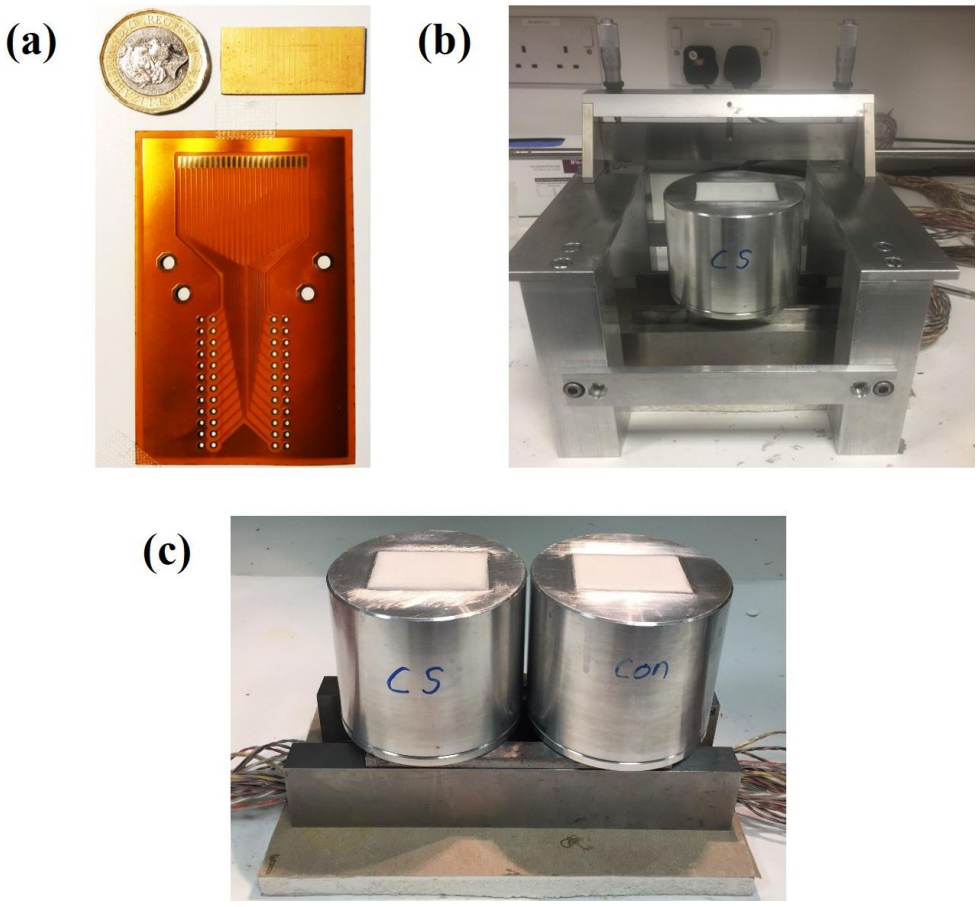

Figure 5-17: (a) Composite array active layer & Flexible PCB; (b) Casting matching layer using an adjustable blade; (c) Fully fabricated CS Fractal and conventional linear array

5.5. Experimental Validation of Cantor Set Array Transducer

5.5.1. Electrical Impedance of Active Layer

The electrical impedance profiles of the active layer for both array microstructures were measured and are shown in Figure 5-18.

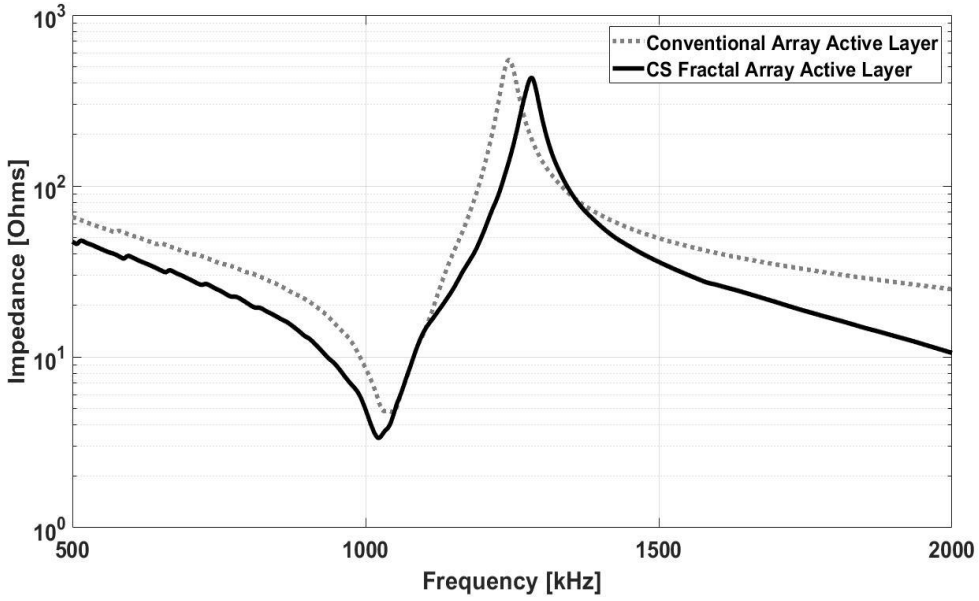

Figure 5-18: Measured electrical impedance magnitude spectrum of the CS array and conventional array composite active layer

It can be seen from Figure 5-18 that the electrical resonance frequency of the CS fractal array and conventional array active layer are located at 1022 kHz and 1047 kHz respectively. The electromechanical coupling coefficient, k_t, is 0.64 for the CS fractal

array active layer and 0.60 for the conventional array active layer. Therefore, a better energy conversion and improved bandwidth can be realised by the CS fractal design.

5.5.2. Active Layer Displacement Profile

The surface vibration behaviours of the active layers of both arrays was evaluated using a 3D scanning laser Doppler vibrometer (LDV) (Polytec Inc, Waldbronn, German). The experimental setup is shown in Figure 5-19. The front face of the device was positioned perpendicular to the laser source. Two broadband chirp signals generated by the internal source of the LDV with centre frequencies of 1022 kHz and 1047 kHz were employed to drive the CS fractal and conventional 2-2 device, respectively.

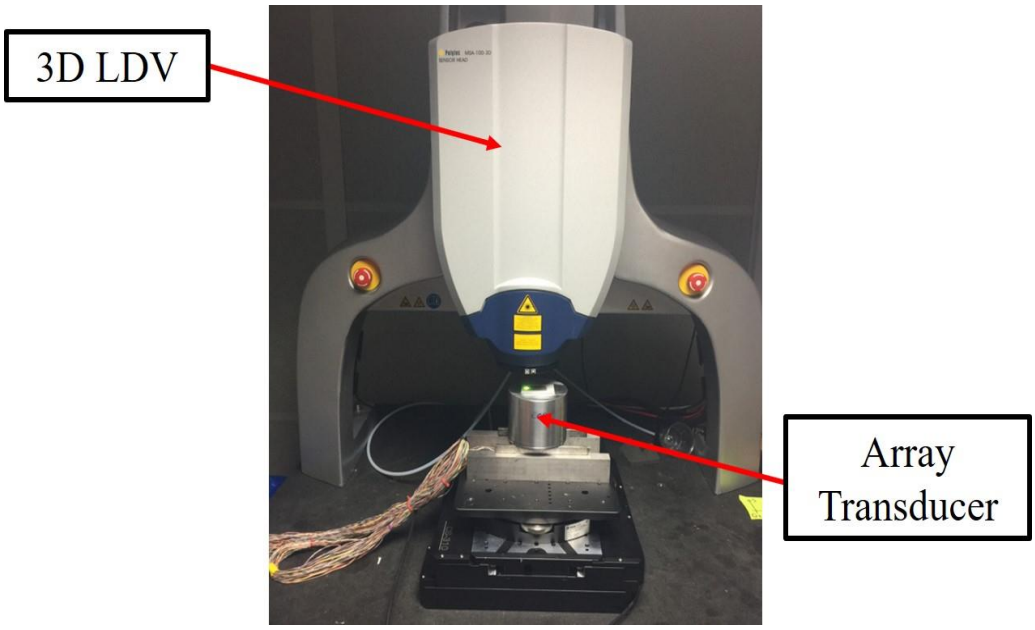

Figure 5-19: Experimental setup for 3D LDV measurement

The resulting average surface velocity frequency response for both devices is shown in Figure 5-20.

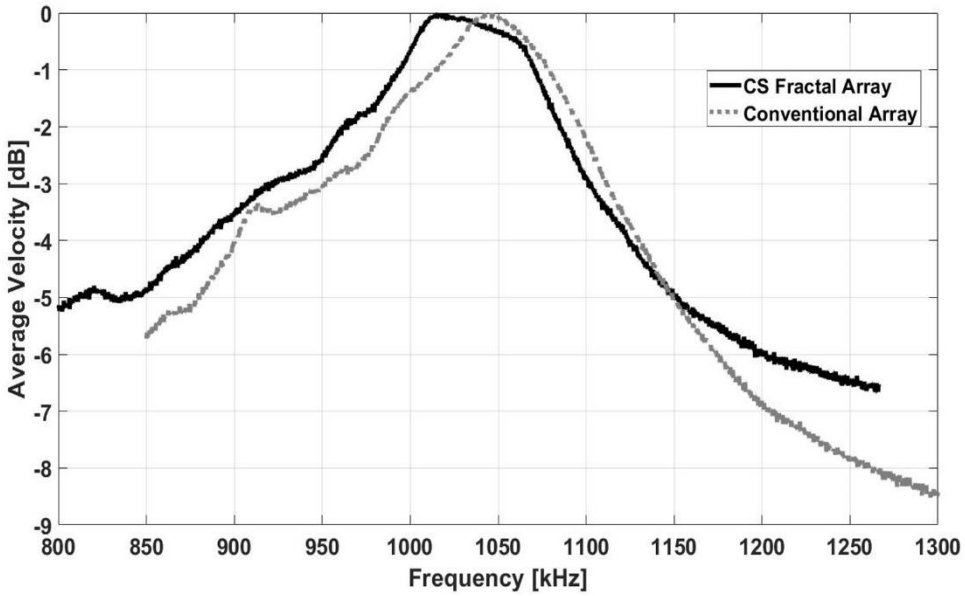

Figure 5-20: Measured average surface velocity for the CS fractal and the conventional array as a function of frequency

From Figure 5-20, the –6 dB bandwidth of the average surface velocity frequency response is 40.2 % for the CS fractal array and 31.9 % for the conventional design. Hence, a 32.0 % bandwidth improvement is suggested for the CS fractal array with respect to the conventional array.

5.5.3. Mechanical Crosstalk Measurement

The mechanical crosstalk of the fabricated CS fractal array and conventional linear array at their operating frequency was measured using the 3D LDV using the same experimental setup shown in Figure 5-19. Two sinusoidal tone burst signals, with frequencies of 1022 kHz and 1047 kHz from the internal source of the LDV, were employed to drive a single element of both the CS fractal and conventional 2-2 device, respectively, and the measured results are shown in Figure 5-21.

In Figure 5-21, the centre positions of the driven element and two adjacent elements at either side of the driven element are marked with vertical red dash lines. The crosstalk of the CS fractal array is at a similar level to the conventional array for the first adjacent elements, but 5 to 15 dB lower for the second adjacent elements. This result correlates well with what has been predicted in Section 5.3.3, using Lamb wave dispersion analysis. There are some inconsistencies in this measurement, with the conventional 2-2 array demonstrating lower mechanical cross-talk in the 0 – 5 mm region, for example. Hence, the main observation should be that there is a slight improvement in mechanical cross-talk for the CS fractal array configuration. Moreover, the asymmetry of the measured profiles may be indicative of issues generated through the fabrication process.

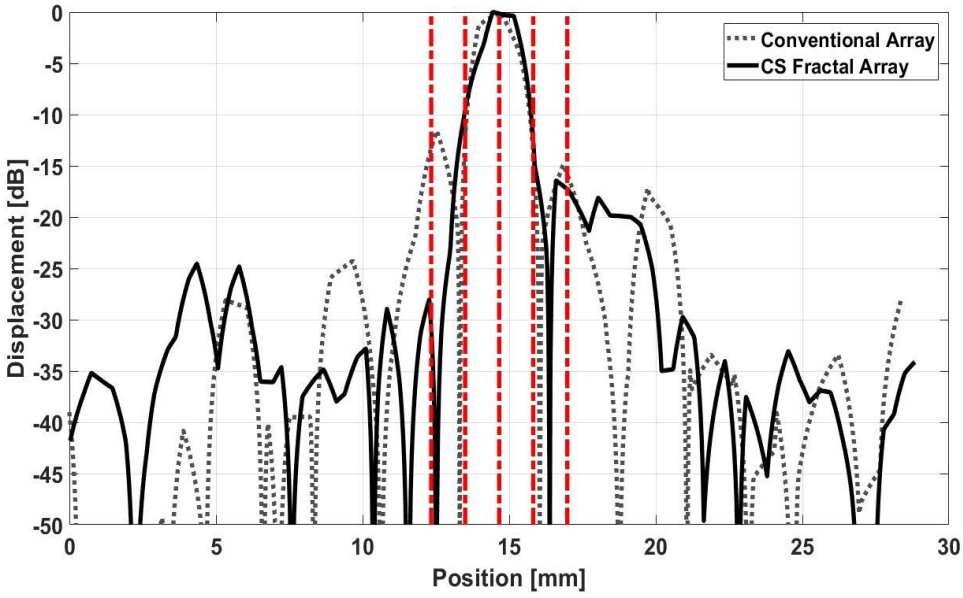

Figure 5-21: Measured crosstalk of CS fractal and conventional array

5.5.4. Pulse-Echo Response of Array Elements

The pulse-echo responses for each element of both array devices were measured using a multi-element array controller, FIToolbox (Diagnostic Sonar Ltd, UK), and compared with the FE simulated results, which is shown in the Figure 5-22 (a) and (b). It can be seen in the Figure 5-22 that all of the elements behaved as expected in each array and the experimental results correlate with the simulation data reasonably.

The bandwidth and the peak-to-peak voltage of each individual array element for both arrays is plotted in Figure 5-23 and Figure 5-24. The average value and standard deviation of the -6 dB bandwidth and peak-to-peak voltage for devices is summarized in Table 5-3.

Table 5-3: Pulse-echo experiment result summary

		CS Fractal Array	Conventional Array
-6 dB Bandwidth	Average (%)	60.1 %	57.5 %
	Standard Deviation	0.67	1.73
Peak-to-Peak Voltage	Average (mV)	9.6 mV	6.2 mV
	Standard Deviation	1.19	1.31

It can be observed that the average element -6 dB bandwidth and peak-to-peak voltage of the CS fractal array is better than the conventional 2-2 array as the result of introducing the varied pillar size scales within the CS fractal array design. The uniformity of the elements behaviour is slightly better for the fabricated CS fractal when compared to the conventional 2-2 array, which again indicates potential errors originating from the manufacturing process.

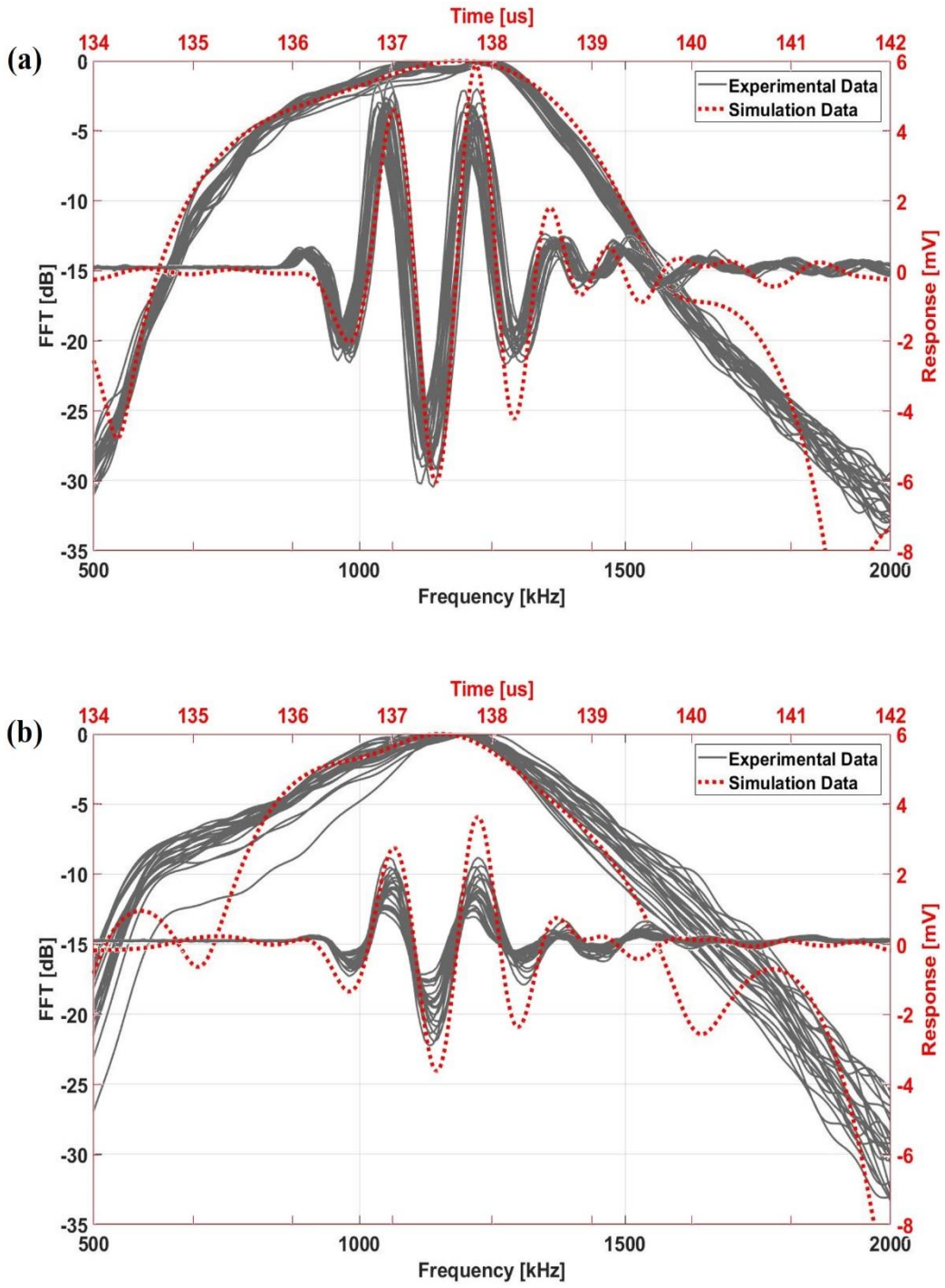

Figure 5-22: Measured and simulated pulse-echo time-domain waveform and frequency spectrum: (a) CS fractal array (b) conventional array

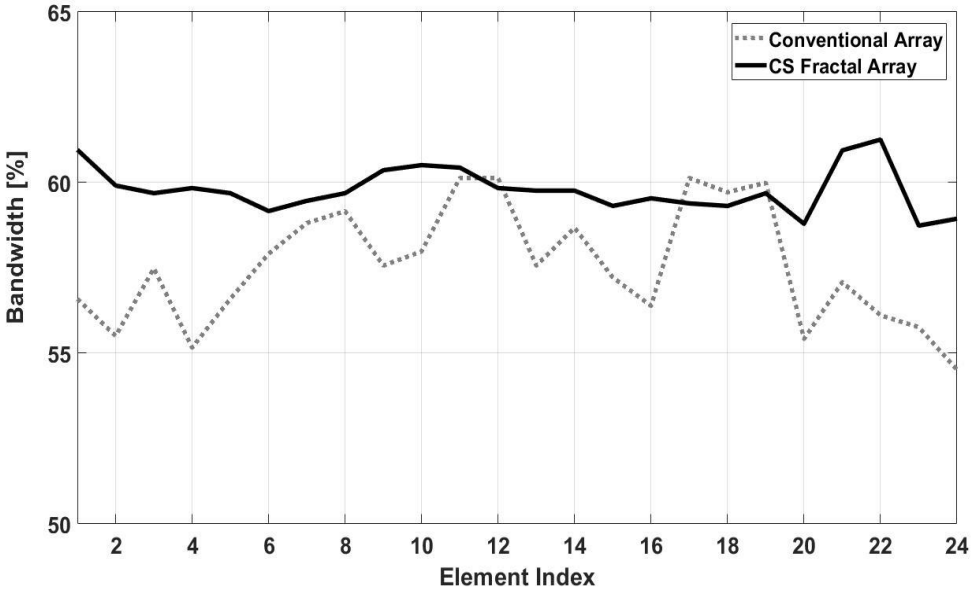

Figure 5-23: Measured array element -6 dB pulse echo response bandwidth for the CS fractal and conventional array transducer

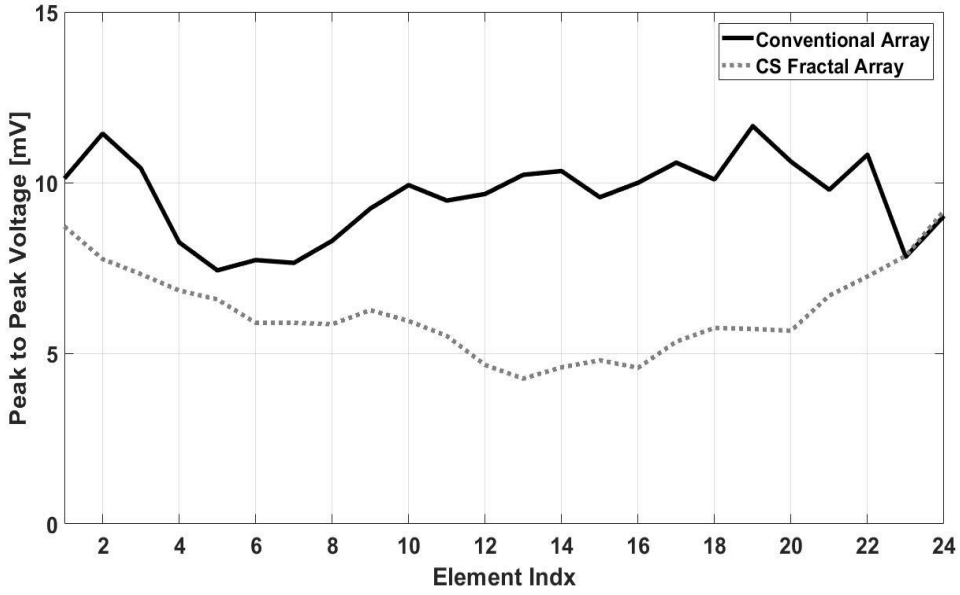

Figure 5-24: Measured array element peak-to-peak voltage for the CS fractal and conventional array transducer

5.5.5. Array Imaging Performance

In order to evaluate and compare the imaging and defect sizing capability of both fabricated arrays, a wire-water phantom was designed, and a graphic representation is shown in Figure 5-25. The diameters of the copper wires are 0.75 mm (~ 0.5 λ), 1.13 mm (~ 0.75 λ) and 1.60 mm (~ 1.0 λ), respectively. The FMC data was acquired, and images were produced using TFM, see Section 2.2.3.3 for details, for each array device. Figure 5-26 shows the fabricated wire-water phantom and the FMC/TFM experimental setup.

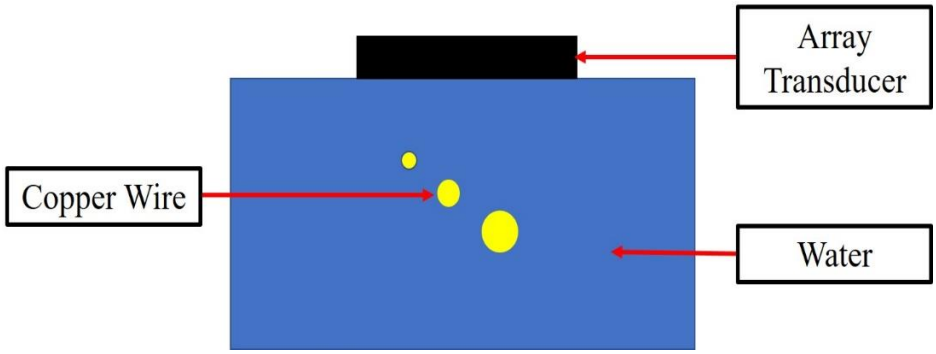

Figure 5-25: Wire-water imagining phantom schematic

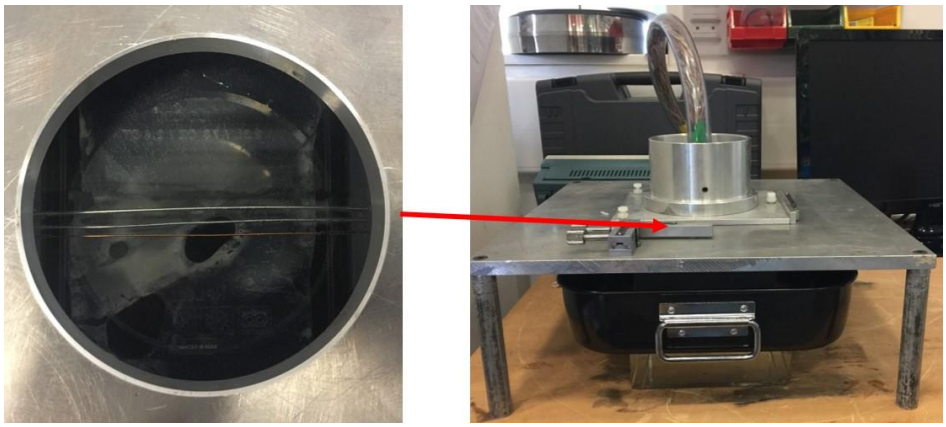

Figure 5-26: FMC/TFM experiment setup

Each element of both arrays was excited using a half cycle sine wave with a frequency of 1 MHz and controlled by the FIToolbox multi-element array controller. 16-bit resolution and a 25 MHz sampling frequency was used during the data acquiring process. The resulting FMC/TFM images [17] produced by the two arrays are shown in Figure 5-27. It can be seen that the CS array produced a higher resolution TFM image compared to the conventional array and importantly, the imaging artefacts associated with each wire are reduced for the CS array. Using the -3 dB sizing method, the accuracy of the CS fractal array for the wire with 0.5 λ, 0.75 λ and 1.0 λ diameter is 4.4 %, 20.5 % and 47.7 % better than the conventional linear array. The -3 dB sizing result of both arrays is summarized in Table 5-4. Moreover, the signal strength in the CS array image is 3.8 dB higher than that generated by the conventional array for the wire with 0.5 λ diameter.

Table 5-4: TFM image sizing result

	CS Fractal Array		**Conventional Array**	
Wire Diameter	**Measured Diameter**	**Sizing Error**	**Measured Diameter**	**Sizing Error**
0.5 λ (0.75 mm)	1.62 mm	116.0 %	1.66 mm	121.3 %
0.75 λ (1.13 mm)	1.52 mm	34.5 %	1.62 mm	43.4 %
1.0 λ (1.60 mm)	1.73 mm	8.1 %	1.85 mm	15.5 %

It can be seen from Table 5-4 that the CS fractal array has a more accurate sizing ability, when compared with the conventional linear array for all sizes of copper wire. Although, as expected, both arrays do not perform particularly well for sub-wavelength targets.

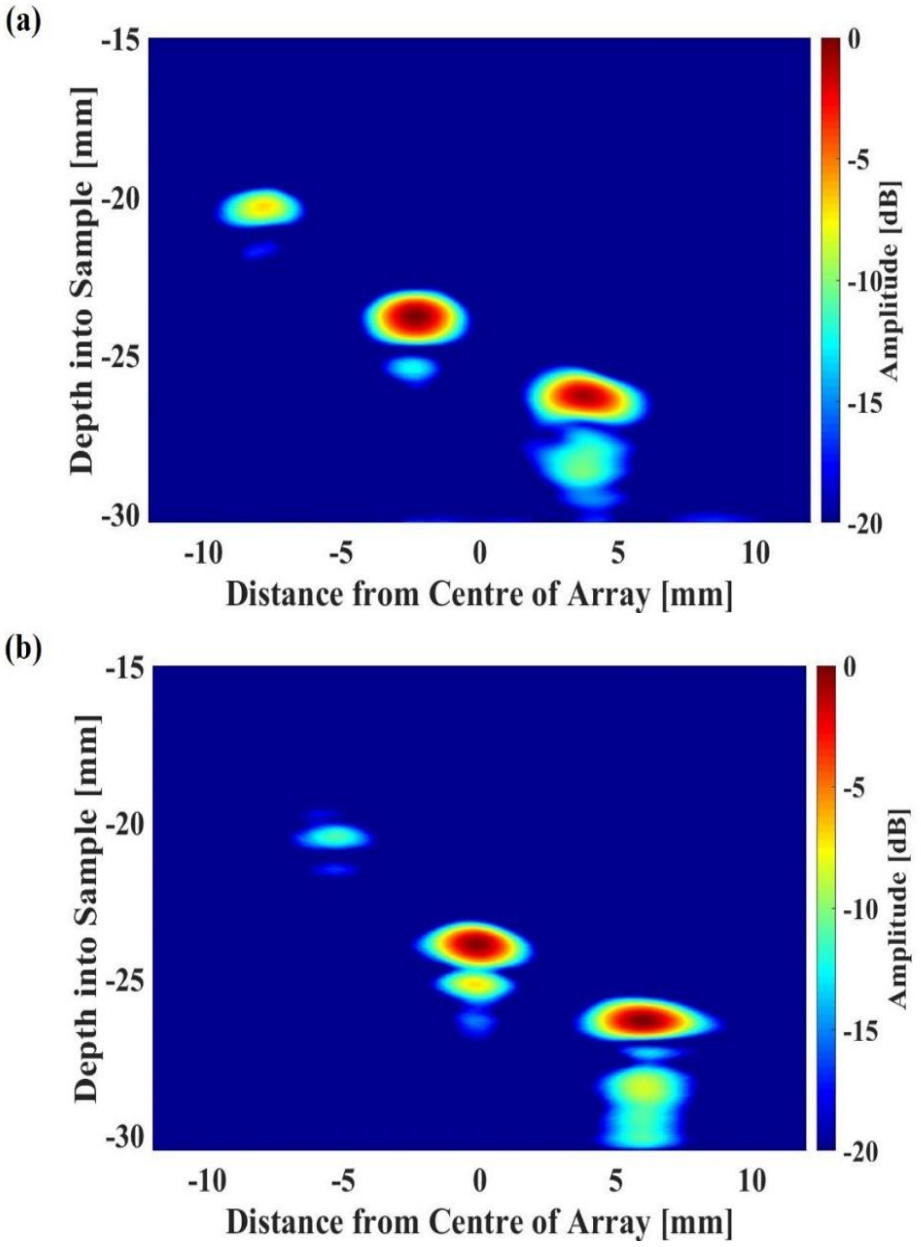

Figure 5-27: TFM imaging of the three wires in water phantom using: (a) CS fractal array; (b) conventional array

5.6. Chapter Summary

This Chapter describes the implementation of a CS fractal geometry as the structure of a linear ultrasonic array design. A mathematical algorithm was developed to define the geometrical features of the CS fractal geometry and a series of parameter sweep simulations were performed to optimize the design of both a CS fractal array and a conventional linear array element.

The FE models were used to study the vibration behaviour at the transducer resonant frequency and also investigate the Lamb wave dispersion characteristics for both array configurations. As there is more than one pillar size in the CS array design, two thickness modes were identified in the CS array design and the coupling between the thickness mode and Lamb mode is weaker when compared with the conventional array design. The FE simulation results also indicate that a good bandwidth and sensitivity performance was demonstrated in the CS fractal array designs. An approximately 13.4 % bandwidth improvement (56.7 % against 50.0 %) and 63.0 % sensitivity increase (11.9 mV against 7.3 mV peak-to-peak voltage) was achieved when compared to the conventional array configurations. Lastly, the FE model was used to simulate the beam profile when both arrays were focused at 15 mm. The simulation results showed that a 9 dB side lobe reduction was achieved by the CS fractal array design as compared to an equivalent conventional array design.

A CS fractal and conventional linear array with 24 elements were fabricated and characterised. First of all, the pulse-echo response of all elements behaved uniformly in

each array design and the experimental data matched well with the FE simulated results. The average -6dB bandwidth and peak-to-peak voltage of the CS fractal array are higher than the conventional 2-2 array. Secondly, the mechanical crosstalk of both array devices was measured and there was a slight enhancement for the CS fractal array design. Thirdly, images of a wire-water phantom produced by the two arrays using the total focusing method and full matrix capture techniques shows that the CS fractal array outperforms the conventional 2-2 array in terms of image resolution, sizing accuracy and signal strength.

CHAPTER VI

ADVANCED CANTOR TARTAN FRACTAL ARRAY CONFIGURATION

In Chapter V, an ultrasonic array using Cantor Set (CS) fractal geometry was developed and characterised. This CS fractal array delivered improved bandwidth and sensitivity when compared with a conventional linear array with 2-2 microstructure. In order to introduce additional varied length scales and achieved a further bandwidth improvement, an advanced fractal geometry comprising orthogonal CS fractal geometries, known as the Cantor Tartan (CT), is explored in this Chapter.

A CT fractal array element is built and optimized using the parameter sweep simulation approach. The behaviour of the optimized CT fractal array element is investigated using FE modelling method and compared with the CS fractal array element and conventional linear array element designed in Chapter V.

6.1. Cantor Tartan Fractal Array Element Design

The FE model of a CT fractal array element was implemented and is shown in Figure 6-1. In order to increase the number of different length scales by a factor of 4 when compared with the CS fractal array element designed in Chapter V, this CT array element comprises a combination of a Level II CS fractal geometry in azimuth and a Level IV CS fractal geometry in elevation.

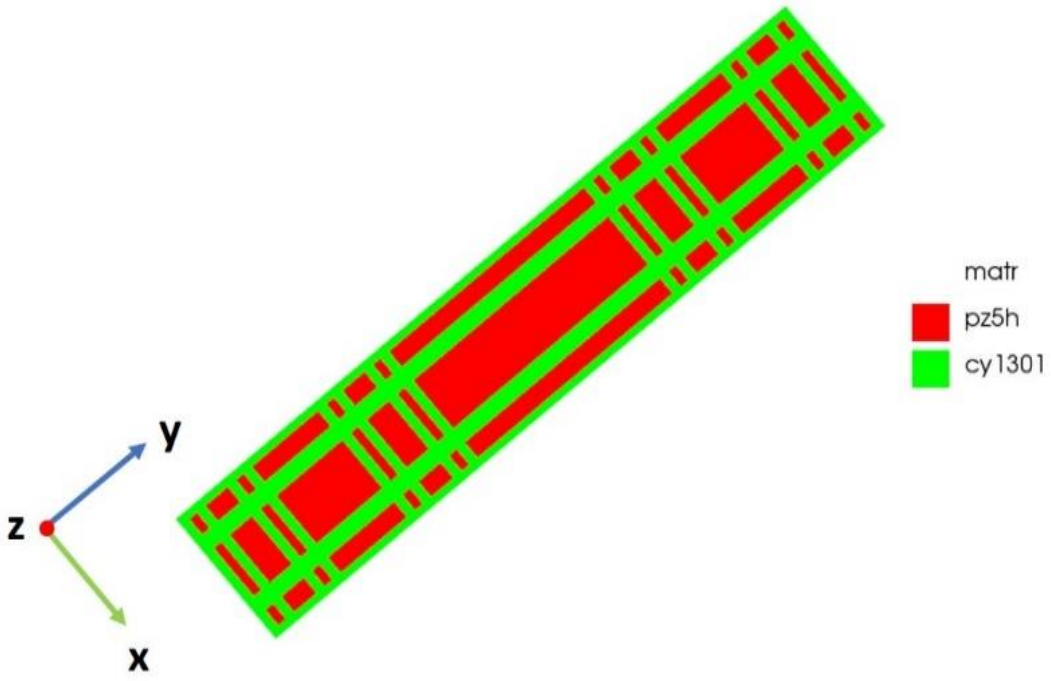

Figure 6-1: Advanced orthogonal CT fractal array element

6.2. Cantor Tartan Fractal Array Element Optimization

In order to optimize the bandwidth performance of the CT fractal array element, the FE sweep simulation approach was employed. First of all, the Level II CS fractal geometry design in Section 5.2 was used in x-dimension. In y-dimension, the pillar length at fractal generation Level IV of the CT fractal geometry, L_{y-4}, was varied from 0.1 mm to 1.0 mm with a step size of 0.05 mm.

According to the resulting conductance spectrum, shown in Figure 6-2, and the calculated Q-factor, shown in Figure 6-3, the optimal value of $L_{y-4}$was determined as 0.25 mm.

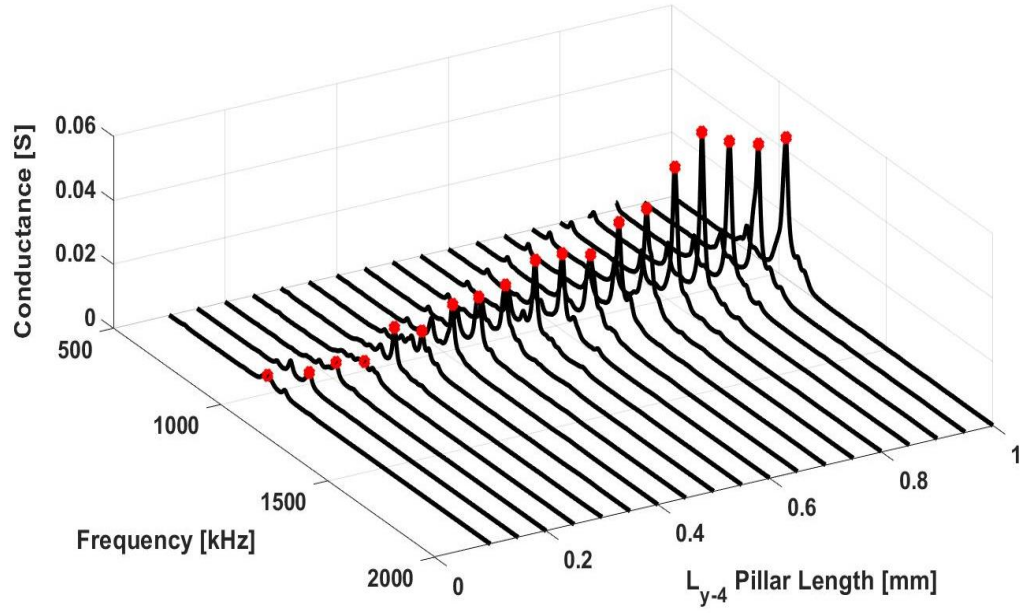

Figure 6-2: FE derived conductance spectrum for different values of L_{y-4} in the CT fractal array design

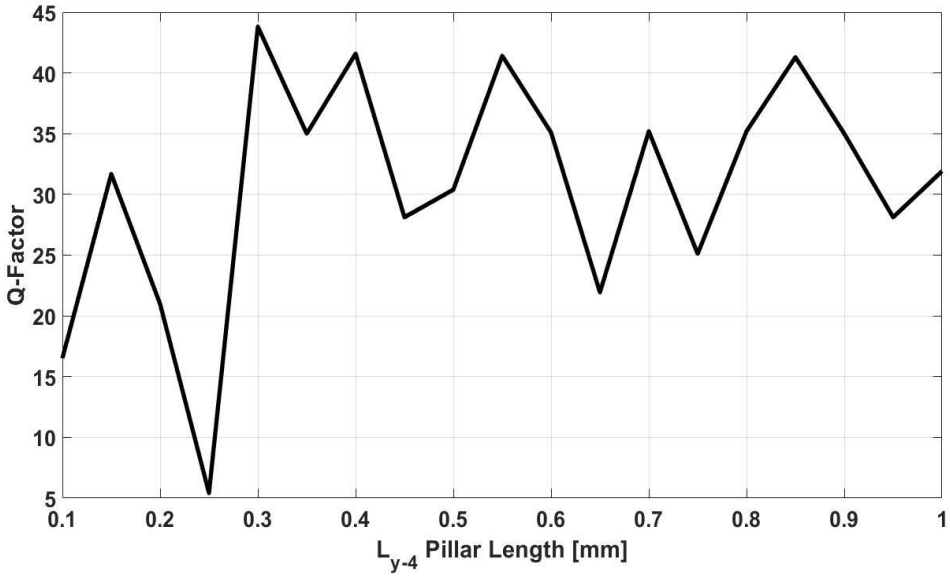

Figure 6-3: Q-factor for different values of L_{y-4} in the CT fractal array design

Secondly, the scaling factor, k_y, was varied from 0.2 to 0.4 with a step size of 0.01 and chosen to be 0.34 according to the resulting conductance spectrum, shown in Figure 6-4, and the calculated Q-factor, shown in Figure 6-5.

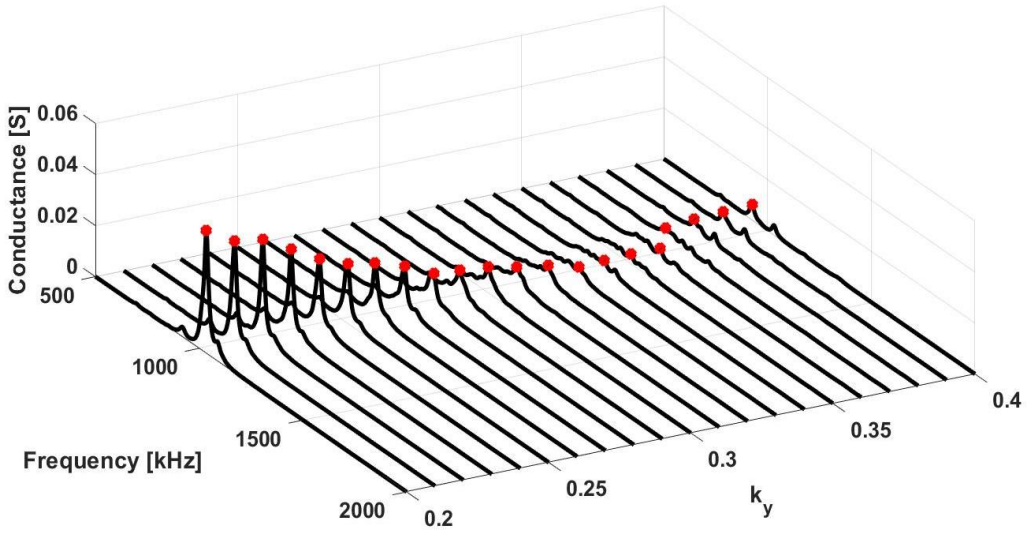

Figure 6-4: FE derived conductance spectrum for different values of k_y in the CT fractal array design

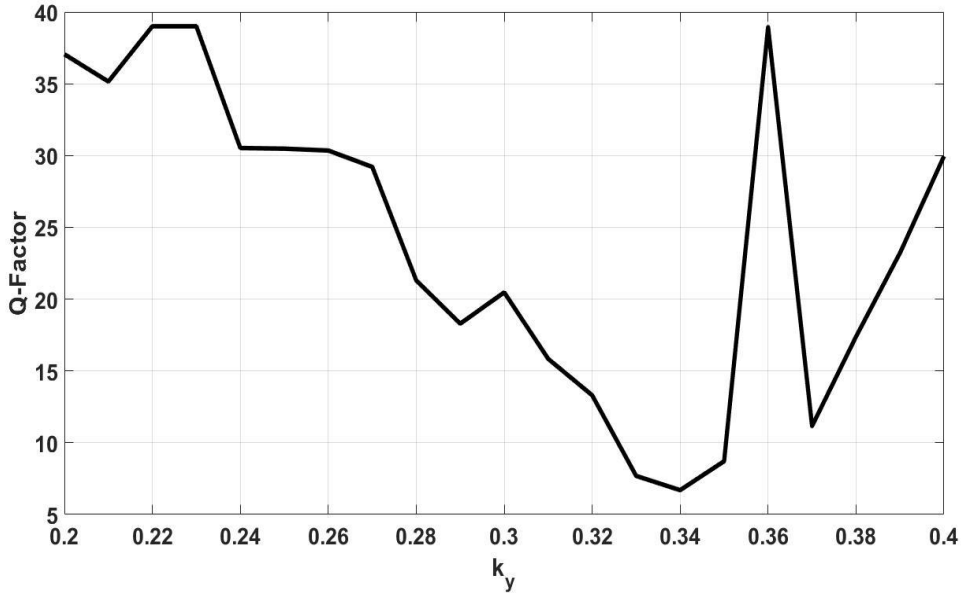

Figure 6-5: Q-factor for different values of k_y in the CT fractal array design

The pillar length from fractal generation Level III, L_{y-3}, to Level I, L_{y-1}, and the saw width in elevation direction, S_y, of the CT fractal geometry can then be calculated using Equations (5-1) and (5-2). The same dual matching layer scheme and a backing layer material were added to optimize the performance of the array. The specification of this CT fractal array design is listed in Table 6-1 and material properties can be found in Section 5.3.4 in Chapter V.

Table 6-1: Design Specification of CT fractal array

<table>
<tr><td rowspan="2">Pillar Width</td><td colspan="2">Level I, L_1</td><td colspan="2">Level II, L_2</td></tr>
<tr><td colspan="2">0.47 mm</td><td colspan="2">0.15 mm</td></tr>
<tr><td rowspan="2">Pillar Length</td><td>Level I, L_{y-1}</td><td>Level II, L_{y-2}</td><td>Level III, L_{y-3}</td><td>Level IV, L_{y-4}</td></tr>
<tr><td>6.36 mm</td><td>2.16 mm</td><td>0.74 mm</td><td>0.25</td></tr>
<tr><td rowspan="2">Saw Width</td><td colspan="2">Azimuth, S_x</td><td colspan="2">Elevation, S_y</td></tr>
<tr><td colspan="2">0.13 mm</td><td colspan="2">0.27 mm</td></tr>
<tr><td>Active Layer Material</td><td colspan="4">PZT-5H Ceramic & Hardset Polymer</td></tr>
<tr><td>Thickness</td><td colspan="4">1.5 mm</td></tr>
<tr><td>VF</td><td colspan="4">51.7 %</td></tr>
<tr><td rowspan="2">Matching Layer I</td><td colspan="4">Medium Set Polymer</td></tr>
<tr><td colspan="4">267 μm</td></tr>
<tr><td rowspan="2">Matching Layer II</td><td colspan="4">Hardset polymer filled with 3 μm calcined alumina powder by 70 % weight fraction</td></tr>
<tr><td colspan="4">640 μm</td></tr>
<tr><td rowspan="2">Backing Layer</td><td colspan="4">Hardset polymer filled with tungsten powder by 24 % weight fraction</td></tr>
<tr><td colspan="4">30 mm</td></tr>
</table>

6.3. Array Element Pulse-Echo Response

The far-field pulse-echo response of this CT fractal array element was investigated using PZFlex. Figure 6-6 displays the predicted pulse-echo response of CT array element when compared with the CS array and conventional array element described in Chapter V.

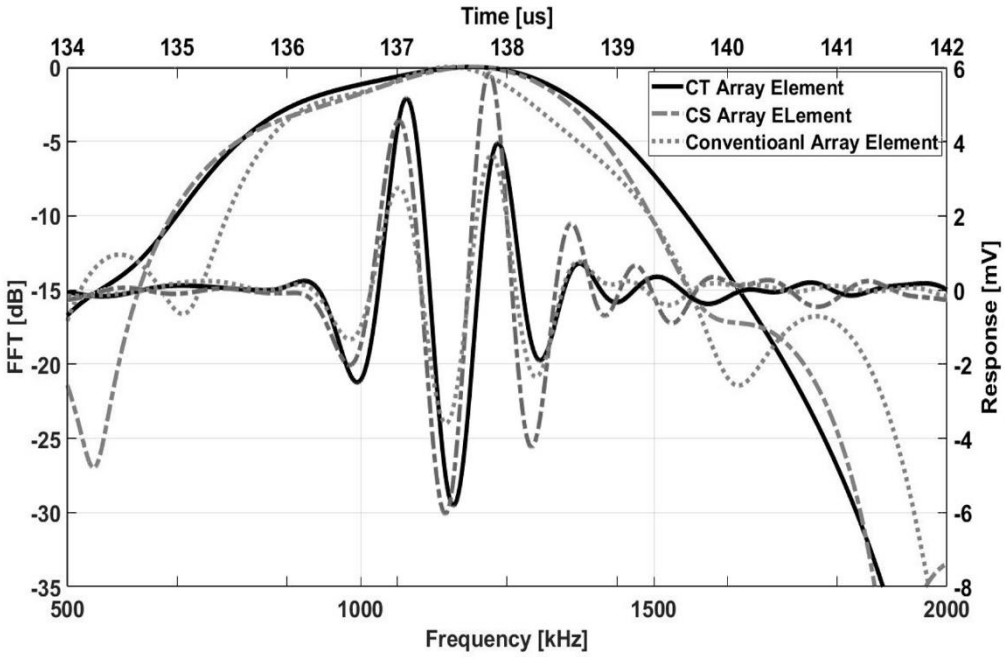

Figure 6-6: FE simulated pulse-echo response of CT fractal array element

It can be measured from Figure 6-6 that the CT fractal array element has predicted a -6 dB bandwidth of 61.8 % and peak-to-peak received voltage, V_{p-p}, of 11.0 mV. When compared to the CS fractal and conventional linear array element, see Table 5-2, this CT fractal design has the best bandwidth performance, as a result of the introduction of a high fractal generation level. The CT simulation results indicate that the sensitivity is lower than the CS configuration, but comparable with the conventional 2-2 design.

6.4. Beam Forming

The beam profile of the 24-element CT fractal array focused on the central axis, at distance of 15 mm from device front face, is simulated using PZFlex and is shown in Figure 6-7.

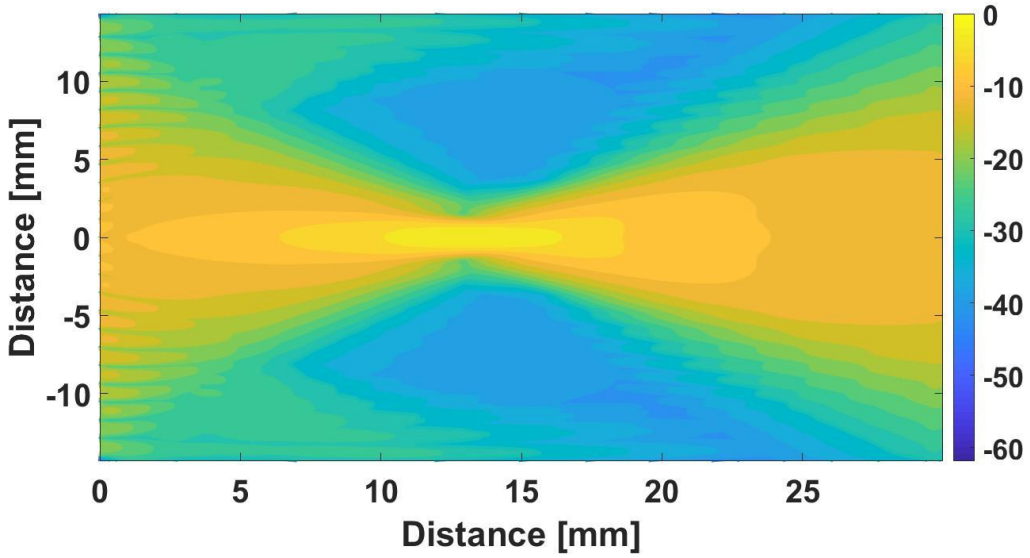

Figure 6-7: FE simulated beam profile of CT fractal array

The comparison in terms of side lobe level and -3 dB focal zone area between the CT fractal array, CS fractal array and conventional linear array is summarised in Table 6-2.

Table 6-2: Side lobe and focal zone area of CT, CS and conventional array when focused at 15 mm

	Conventional Array	**CS Array**	**CT Array**
Focal Area	9.93 mm × 1.44 mm	11.76 mm × 1.52 mm	6.28 mm × 1.06 mm
Side Lobe	-21 dB	-30 dB	-27 dB

It can be seen that the side lobe of the CT array is 6 dB lower than the conventional array design. At the same time, the best focusing ability is predicted to be achieved by the CT array design, as a direct consequence of the multiple pillar sizes in both azimuth and elevation dimensions.

6.5. Chapter Summary

In order to further enhance the bandwidth performance of the array, another advanced fractal geometry comprising orthogonal CS fractal geometries, known as the CT was investigated using an FE modelling approach. A -6 dB pulse-echo bandwidth of 61.8 % can be predicted using FE modelling, which is 9.0 % and 23.6 % higher with respect to the CS fractal array design and conventional array design, respectively. At the same time, due to the fact that the CT array element contains varying pillar sizes in both azimuth and elevation dimensions, the CT array demonstrated a better focusing ability when compared to the CS fractal and conventional array.

In the future, the CT fractal array will be fabricated and fully characterised regarding its pulse-echo response, crosstalk and imaging performance.

Chapter VII

CONCLUSION AND FUTURE WORK

7.1. Thesis Synopsis

This thesis described the development of piezoelectric composite ultrasound transducers incorporating a fractal geometry to enhance operational bandwidth. The fractal design approach introduced multiple length scales into the transducer microstructure which results in multiple resonances within a single transducer structure. If appropriately configured, the operational bandwidth of the transducer can be extended through coupling of the resonant modes within the fractal structure. Four different fractal geometries, Sierpinski Gasket (SG), Sierpinski Carpet (SC), Cantor Set (CS) and Cantor Tartan (CT) were investigated to design piezoelectric composites with different microstructural configurations.

The behaviour of these fractal composite designs was explored using a combined FE modelling approach, supported by experimental verification. The FE simulation results demonstrated the potential for performance enhancement, particularly a bandwidth extension, by using a fractal composite design when compared to equivalent conventional composite designs. Two fractal geometries, SG and CS, were fabricated into a single element device and an array ultrasound transducer. Both devices were experimentally

characterised and compared to equivalent conventional composite transducer designs. Importantly, the SG fractal single element and the CS fractal array transducers outperformed the conventional designs and demonstrated a good correlation with the FE simulation results.

This research has fabricated the world's first fractal composite transducer and transducer array. The results generated by these transducers is extremely encouraging. The key challenge to commercial implementation of fractal composite devices is the additional complexity within the fabrication stage. It is considered that the current improvements in bandwidth and sensitivity described in this thesis would not justify the additional fabrication costs. Although, as new fabrication techniques become mainstream, for example 3D printing of piezoelectric materials, then the realisation of fractal composite transducer configurations will become an economically viable proposition, where the ultrasound imaging applications in the industrial or medical field could benefit from the broadband and high sensitivity fractal ultrasound transducer designs to achieve a better imaging quality mainly in terms of the high image resolution and signal-to-noise ratio.

7.1.1. Singe Element Fractal Ultrasound Transducer Design

In order to improve the transducer operational bandwidth, two fractal geometries, SG and SC, were implemented as the microstructure of a single element composite design, respectively. An FE analysis simulation tool was used to investigate each fractal composite configuration. For both fractal composite configurations, simulation results show that when applying the SG or SC geometry at fractal generation levels greater than

Level III, a wider bandwidth can be achieved in both transmission and reception mode compared to an equivalent conventional design.

Both SG and SC fractal composites demonstrated a multi-modal characteristic in their electrical impedance spectrum, corresponding to the resonance of pillars at different length scales within each fractal composite configuration. The TVR, OCV and pulse-echo response of both single element fractal composites were evaluated theoretically and compared to corresponded equivalent conventional 1-3 composite designs via 3D FE models. Consistent simulation results were achieved in both cases. Firstly, in transmission mode, when compared to their equivalent conventional 1-3 composites, 8.8 % and 10.0% bandwidth improvements, and 4.2 dB and 3.5dB sensitivity increases were predicted for the SG and SC fractal composites, respectively. Secondly, in reception mode, by using the SG and SC fractal geometries, the bandwidth is 5.4 % and 10.4 % higher than their equivalent designs, respectively, but the sensitivity is approximately at the same level as the corresponding equivalent conventional design. Lastly, in the pulse-echo response, both fractal designs showed an encouraging improvement with regards to bandwidth and signal strength, where a bandwidth extension of 12.1 % / 10.4 % and sensitivity enhancement of 10.7 % / 15.0 % were achieved by the SG and SC fractal composite, respectively.

It has also been shown in order to realise these performance enhancements, the 1-3 composite microstructure must take the form of the fractal design, rather than using a fractal electrode with a conventional periodic parallelepiped shaped pillar structure. This has implications for the fabrication of fractal transducers and confirms that the key

limitation on the uptake of this technology by commercial transducer manufacturers will be based around advanced fabrication techniques.

However, one difference with the SC fractal composite was that the beam profile predicted using Huygens-Fresnel principle showed no improvement regarding the side lobe reduction when compared to the conventional 1-3 composite, whereas the side lobe of the SG composite is 5dB lower than the conventional 1-3 composite. As the result, it can be said that the beam profile of a fractal composite is dependent on its geometry and there is no guarantee that a decreased side lobe level can be achieved by implementing a fractal geometry on a piezoelectric composite design. Overall, it can be concluded that the field profile from fractal and conventional 1-3 devices show a high degree of similarity and will not be a deterrent on the future potential transducer opportunities for fractal designs.

The decision was taken to manufacture a prototype SG fractal composite transducer at Level IV using the pillar placement method. An equivalent conventional composite device was manufactured using the traditional ‘dice-and-fill’ technique for the purpose of comparison. There are two main challenges in fabricating this SG fractal device due to the limitation of the 3D printing and ceramic dicing technique, which would have an effect on the composite performance. First of all, the mould needs to be designed carefully and 3D printed precisely in order to make sure the individual pillars can be placed accurately into the mould and importantly, they must also stay in a vertical position during the remainder of the fabrication process. Secondly, it is difficult to cut triangular pillars in small sizes and time consuming to manually place small sized pillars into the mould. However, one reason that the self-similar fractal geometry would still be a valuable choice

compared with a random distributed geometry is that the fractal geometry can be generated by following a simple algebraic rule, which facilitates analyses of the transducer performance within the design space.

The TVR, OCV and pulse-echo response of the fabricated SG fractal transducer were all characterized experimentally and compared with the fabricated conventional composite transducer and a commercial Panametrics transducer. It has been indicated that a 27.2 % and 105.1 % transmission bandwidth improvement can be achieved by the SG fractal composite when compared with the conventional 1-3 composite and commercial Panametrics transducer, respectively. In the reception mode, the bandwidth of the SG fractal composite is 32.9 % higher than the commercial Panametrics transducer. Moreover, the pulse-echo response of the SG fractal composite demonstrated a 70.0 % bandwidth enhancement and a 22.1 % sensitivity improved with respect to the commercial Panametrics transducer.

7.1.2. Linear Fractal Ultrasound Array Development

As the fabrication process of a single element SG fractal composite is challenging and time consuming, assembling multiple single element SG fractal composites to produce an ultrasound array device would be prohibitive. Therefore, in order to explore the potential of developing an ultrasound array using fractal geometry, a linear ultrasound array with 2-2 connectivity and elements incorporating a CS fractal geometry was developed in Chapter V.

The features of a Level II CS fractal geometry were defined by a mathematical algorithm and an FE simulation tool used to perform a series of parameter sweep simulations based on the CS fractal microstructure and a conventional 2-2 composite with optimized performance. A multi-modal characteristic was discovered in the CS fractal composite and the thickness displacement profile of the CS fractal composite demonstrated that each resonance frequency corresponds to the resonance behaviour of the ceramic pillars at each pillar width scale. The initial FE models of an array element were then extended to form a 24-element ultrasound array configuration. The predicted bandwidth and sensitivity of an array element showed a 13.4 % bandwidth improvement and 63.0 % sensitivity increase for the CS fractal array design, when compared to the conventional array configuration. Moreover, using the predicted FE beam profile of both arrays, axially focused at 15 mm, a 9 dB side lobe reduction was shown for the CS fractal array design.

24-element CS fractal and conventional 2-2 linear arrays were fabricated using the standard ‘dice-and-fill’ technique, which is the industry standard manufacture technique for piezoelectric composite structures. The experimental pulse-echo data indicated that all elements behaved uniformly in each array design and a good correlation was shown when compared to the FE simulated results. Moreover, the imaging capability of this CS fractal array was assessed using a copper wire-water phantom. The key CS array performance characteristics, when compared to the conventional array, can be summarised as:

(a) The measured crosstalk of the second adjacent elements in CS fractal array device is 5 to 15 dB lower than the conventional array;

(b) Better imaging resolution was possessed by the CS fractal array device. The signal strength of the CS fractal array is 3.8 dB higher than the conventional array for the wire with 0.5 λ diameter.

(c) The sizing accuracy of the CS fractal array for the wire with 0.5 λ, 0.75 λ and 1.0 λ diameter is 4.4 %, 20.5 % and 47.7 % better than the conventional linear array.

Following this successful implementation of a fractal linear array in Chapter V, a new simulation programme was undertaken to introduce a higher fractal generation level configuration in Chapter VI. An advanced Cantor Tartan fractal array element was designed with orthogonal fractal geometries. This CT array element is a combination of a Level II CS fractal geometry in azimuth and a Level IV CS fractal geometry in elevation. Compared to the Level II CS fractal array element, this CT array element design is predicted to have a further 9% bandwidth improvement as the result of introducing additional length scales into the microstructure. Although the predicted sensitivity of the CT fractal array element is lower than the CS fractal array element, it is still comparable to the conventional array element design. Moreover, as the result of having varying length scales in both elevation and azimuth direction for CT fractal array element design, the CT fractal array is predicted to have a better focusing performance when compared to both the CS fractal and conventional 2-2 array designs.

7.2. Future Work

7.2.1. Modification of Fractal Composite Fabrication Technique

In Chapter III, a SG fractal composite at generation Level IV was manufactured by preparing the triangular pillars in different sizes and individually placing them manually into a 3D printed mould. It will therefore be very difficult and time consuming to fabricate a SG fractal device in a higher fractal generation level or at a higher operating frequency range (above 1 MHz) using this fabrication technique. As a result, in order to manufacture a fractal composite with a more complex geometry, an advanced manufacturing technique, like 3D printing method, is necessary. The potential fabrication process of 3D printing a fractal composite can be described simply in 4 steps:

(a) Unpolarized piezoelectric particles in the nanometer scale would be mixed with a carefully chosen UV curable polymer.
(b) The active phase microstructure of a fractal composite would be 3D printed using the material prepared in the first step.
(c) The 3D printed active phase microstructure could be poled in silicon oil; the silicon oil could be heated up to speed up the poling process.
(d) The polarized 3D printed active phase microstructure could have the void filled with epoxy polymer and then the composite could be lapped to its desired thickness.

By using this fabrication process, a fractal geometry in a higher generation level or finer scale could be manufactured efficiently and accurately. The SC fractal composite reported in Chapter IV could also be fabricated using this method.

7.2.2. Characterization and Manufacturing of Cantor Tartan Fractal Array

At Chapter VI, another advanced fractal geometry comprising orthogonal CS fractal geometries, known as the CT was studied using an FE modelling approach for the purpose of evaluating the possibility of further enhancing the bandwidth performance of an ultrasound array with a more complex structure. 9.0 % and 23.6 % bandwidth improvements were predicted in this CT fractal array design, when compared to the CS fractal array and conventional array design, respectively. In order to validate the simulation work, a 24-element CT array at 1MHz could be manufactured in the future. The element pulse-echo response, imaging ability and beam forming capability of this CT array could be characterised experimentally and compared with the results of the fabricated CS and conventional 2-2 array.

7.2.3. 2D Ultrasound Array Incorporating a Fractal Geometry

In this thesis, due to the limitation of the fabrication technique, only a 1D linear ultrasound array using the CS fractal geometry was manufactured and characterised. However, 3D volume imaging with better resolution and sizing accuracy could be produced by a 2D fractal ultrasound array. A potential approach to produce this 2D fractal array would be to

utilise six triangular composites with a SG fractal geometry to form an element in a hexagonal shape, where a 2D array could be realised by placing each hexagon element with a reasonable kerf width. One hexagonal element comprised of six, generation Level IV, SG fractal composites is shown in Figure 7-1 (a) and the array element layout configuration of the SG fractal 2D array is shown in Figure 7-1 (b).

It has been reported by Dziewierz *et al.* [125] that a 2D array with hexagonal-shaped elements can produce a lower level of mechanical crosstalk when compared to a conventional 2D array with a square element shape. With an advanced fabrication technique developed in the future, the fabrication of a 2D array incorporating a SG fractal geometry could therefore be achieved.

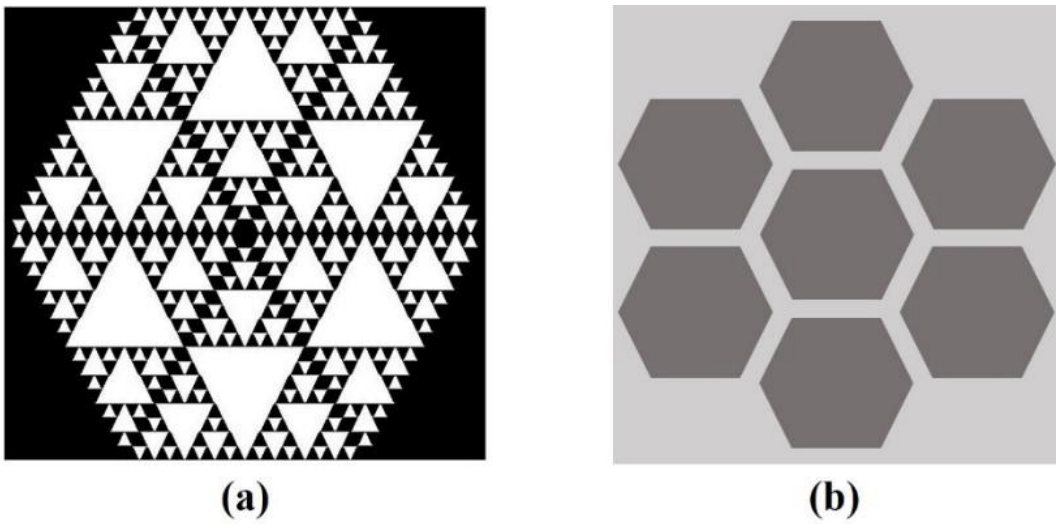

Figure 7-1: (a) One hexagonal element; (b) Element layout configuration of the SG fractal 2D array

References

[1] W. Rössler, “Postembryonic development of the complex tibial organ in the foreleg of the bushcricket *Ephippiger ephippiger* (Orthoptera, Tettigoniidae),” *Cell Tissue Res*, vol. 269, pp. 505–514, 1992.

[2] W. Rössler, “Functional morphology and development of tibial organs in the legs I, II and III of the bushcricket Ephippiger ephippiger (Insecta, Ensifera),” *Zoomorphology*, vol. 112, no. 3, pp. 181–188, 1992.

[3] W. Rössler, A. Hübschen, J. Schul, and K. Kalmring, “Functional morphology of bushcricket ears: comparison between two species belonging to the Phaneropterinae and Decticinae (Insecta, Ensifera),” *Zoomorphology*, vol. 114, no. 1, pp. 39–46, 1994.

[4] E. A. Algehyne and A. J. Mulholland, “A finite element approach to modelling fractal ultrasonic transducers,” *IMA J. Appl. Math.*, vol. 80, no. 6, pp. 1684–1702, Dec. 2015.

[5] L. Orr, A. J. Mulholland, R. L. O’Leary, and G. Hayward, “Analysis of ultrasonic transducers with fractal architecture,” *Fractals*, vol. 16, no. 4, pp. 333–349, 2008.

[6] A. J. Mulholland and A. J. Walker, “Piezoelectric Ultrasonic Transducers With Fractal Geometry,” *Fractals*, vol. 19, no. 04, pp. 469–479, 2011.

[7] T. D. Le Cras and M. Rabinovitch, “Pulmonary Vascular Development,” in *Fetal and Neonatal Lung Development*, A. Jobe, J. Whitsett, and S. Abman, Eds. Cambridge: Cambridge University Press, 2016, pp. 34–57.

[8] I. Md Rian and M. Sassone, “Tree-inspired dendriforms and fractal-like branching structures in architecture: A brief historical overview,” *Front. Archit. Res.*, vol. 3, no. 3, pp. 298–323, Sep. 2014.

[9] H. K. Hahn, M. Georg, and H.-O. Peitgen, “Fractal Aspects of Three-Dimensional Vascular Constructive Optimization,” in *Fractals in Biology and Medicine*, Basel: Birkhäuser-Verlag, 2005, pp. 55–66.

[10] J. T. Bennett, “Development of a Finite Element Modelling System for Piezocomposite Transducer,” PhD Thesis, University of Strathclyde, 1995.

[11] H. Allik and T. J. R. Hughes, “Finite element method for piezoelectric vibration,” *Int. J. Numer. Methods Eng.*, vol. 2, no. 2, pp. 151–157, 1970.

[12] J. A. Hossack, “Modelling Techniques for 1-3 Composite Transducer,” PhD Thesis, University of Strathclyde, 1990.

[13] S. Cochran, M. Parker, and P. Marin-Franch, “Ultrabroadband single crystal composite transducers for underwater ultrasound,” in *IEEE Ultrasonics Symposium*, 2005, pp. 231–234.

[14] P. Marin-Franch, I. Pettigrew, M. Parker, K. J. Kirk, and S. Cochran, “Piezocrystal-polymer composites: New materials for transducers for ultrasonic NDT,” *Insight Non-Destructive Test. Cond. Monit.*, vol. 46, no. 11, pp. 653–657, 2004.

[15] E. S. Ebbini, C. Simon, H. Lee, and Wonjoon Choi, “Self-guided ultrasound phased arrays for noninvasive surgery,” in *IEEE Ultrasonics Symposium*, 1999, vol. 2, pp. 1427–1430.

[16] W. Hackenberger, X. Jiang, P. Rehrig, Xuecang Geng, A. Winder, and F. Forsberg, “Broad band single crystal transducer for contrast agent harmonic imaging,” in *IEEE Symposium on Ultrasonics*, 2003, pp. 778–781.

[17] C. Holmes, B. W. Drinkwater, and P. D. Wilcox, “Post-processing of the full matrix of ultrasonic transmit–receive array data for non-destructive evaluation,” *NDT E Int.*, vol. 38, no. 8, pp. 701–711, Dec. 2005.

[18] A. Rodriguez, A. Salazar, L. Vergara, F. J. Gimeno-Blanes, L. Svilainis, V. Dumbrava, S. Kitov, and A. Chaziachmetovas, “Split Spectrum processing applications for new composite materials imaging,” in *IEEE Ultrasonics Symposium*, 2012, pp. 1473–1476.

[19] J. Saniie, E. Oruklu, and Sungjoon Yoon, “System-on-chip design for ultrasonic target detection using split-spectrum processing and neural networks,” *IEEE Trans. Ultrason. Ferroelectr. Freq. Control*, vol. 59, no. 7, pp. 1354–1368, Jul. 2012.

[20] T. G. Leighton, “What is ultrasound?,” *Prog. Biophys. Mol. Biol.*, vol. 93, no. 1–3, pp. 3–83, 2007.

[21] R. T. Beyer and S. V. Letcher, *Physical Ultrasonics*. New York: Academic Press, 1969.

[22] J. Woo, “A short history of the development of ultrasound in obstetrics and gynecology,” 2008. [Online]. Available: http://www.cfef.org/archives/bricabrac/histoiredesultrasons.pdf. [Accessed: 25-Nov-2018].

[23] A. Elfes, “Sonar-Based Real-World Mapping and Navigation,” *IEEE J. Robot. Autom.*, vol. 3, no. 3, pp. 249–265, 1987.

[24] A. A. Winder, “II. Sonar System Technology,” *IEEE Trans. Sonics Ultrason.*, vol. 22, no. 5, pp. 291–332, 1975.

[25] M. A. Drewry and G. A. Georgiou, “A review of NDT techniques for wind turbines,” *Insight Non-Destructive Test. Cond. Monit.*, vol. 49, no. 3, pp. 137–141, 2007.

[26] S. Chatillon, G. Cattiaux, M. Serre, and O. Roy, “Ultrasonic non-destructive testing of pieces of complex geometry with a flexible phased array transducer,” *Ultrasonics*, vol. 38, no. 1, pp. 131–134, 2000.

[27] N. J. Hangiandreou, “Topics in US B-mode US: Basic Concepts and New Technology,” *RadioGraphics*, vol. 23, pp. 1019–1033, 2003.

[28] R. Badea and S. Ioanitescu, “Ultrasound Imaging of Liver Tumors – Current Clinical Applications,” in *Liver Tumors*, Manhattan, NY, USA: InTech, 2012, pp. 75–102.

[29] P. W. Cains, P. D. Martin, and C. J. Price, “The use of ultrasound in industrial chemical synthesis and crystallization. 1. Applications to synthetic chemistry,” *Org. Process Res. Dev.*, vol. 2, no. 1, pp. 34–48, 1998.

[30] J. Jordens, A. Honings, J. Degrève, L. Braeken, and T. Van Gerven, “Investigation of design parameters in ultrasound reactors with confined channels,” *Ultrason. Sonochem.*, vol. 20, no. 6, pp. 1345–1352, 2013.

[31] K. F. Graff, “A History of Ultrasonics,” in *Physical Acoustics*, vol. 15, New York, USA: Academic Press, 1981.

[32] Antonio Arnau, *Piezoelectric transducers and applications*, 2nd ed. New York: Springer Berlin Heidelberg, 2008.

[33] J. Yang, “The Mechanics of Piezoelectric Structures,” World Scientific Publishing, 2006, pp. 1–24.

[34] S. Cochran, “Piezoelectricity and basic configurations for piezoelectric ultrasonic transducers,” in *Ultrasonic Transducers*, K. Nakamura, Ed. Cambridge, UK: Woodhead Publishing Limited, 2012, pp. 3–35.

[35] *IEEE standard on piezoelectricity*. 176-1987, ANSI/IEEE Standard, 1987.

[36] K. H. J. Buschow, *Encyclopedia of Materials: Science and Technology*. Elsevier, 2001.

[37] H. Jaffe and D. A. Berlincourt, “Piezoelectric Transducer Materials,” *Proc. IEEE*, vol. 53, no. 10, pp. 1372–1386, 1965.

[38] C. G. Oakley and M. J. Zipparo, “Single crystal piezoelectrics: a revolutionary development for transducers,” *IEEE Ultrason. Symp.*, vol. 2, pp. 1157–1167, 2000.

[39] T. R. Shrout, Z. P. Chang, N. Kim, and S. Markgraf, “Dielectric behavior of single crystals near the (1−X) Pb(Mg 1/3 Nb 2/3)O 3 -(x) PbTiO 3 morphotropic phase boundary,” *Ferroelectr. Lett. Sect.*, vol. 12, no. 3, pp. 63–69, 1990.

[40] S. Saitoh, T. Kobayashi, K. Harada, S. Shimanuki, and Y. Yamashita, “Phased

array ultrasonic probe using Pb(Zn1/3Nb2/3)O3-PbTiO3 single crystal," in *Proceedings of SPIE 3341*, 1998, pp. 264–271.

[41] Z. Qiu, "Development of MRI-compatible Transducer Array for Focused Ultrasound Surgery : Development of MRI-compatible Transducer Arrays for Focused Ultrasound Surgery : The Use of Relaxor-based Piezocrystals," PhD Thesis, University of Dundee, 2014.

[42] T. R. Gururaja, W. A. Schulze, L. E. Cross, R. E. Newnham, B. A. Auld, and Y. J. Wang, "Piezoelectric Composite Materials for Ultrasonic Transducer Applications. Part I: Resonant Modes of Vibration of PZT Rod-Polymer Composites," *IEEE Trans. Sonics Ultrason.*, vol. 32, no. 4, pp. 481–498, Jul. 1985.

[43] G. Hayward, "The radiation field characteristics of piezoelectric polymer membrane transducers when operating into air," *IEEE Trans. Ultrason. Ferroelectr. Freq. Control*, vol. 47, no. 6, pp. 1438–1447, 2000.

[44] S. Zhang, S. Lee, D. Kim, H. Lee, and T. R. Shrout, "Elastic, Piezoelectric, and Dielectric Properties of 0.71 Pb (Mg1/3Nb2/3) O3–0.29 PbTiO3 Crystals Obtained by Solid-State Crystal Growth," *J. Am. Ceram. Soc.*, vol. 91, no. 2, pp. 683–686, 2008.

[45] T. R. Gururaja, R. E. Newnham, K. A. Klicker, S. Y. Lynn, W. A. Schulze, T. R. Shrout, and L. J. Bowen, "Composite Piezoelectric Transducers," in *IEEE Ultrasonics Symposium*, 1980, vol. 53, no. 9, pp. 576–581.

[46] J. Bennett and G. Hayward, "Design of 1-3 piezocomposite hydrophones using finite element analysis," *IEEE Trans. Ultrason. Ferroelectr. Freq. Control*, vol. 44, no. 3, pp. 565–574, 1997.

[47] K. C. Benjamin, "Recent Advances in 1-3 Piezoelectric Polymer Composite Transducer Technology for AUV / UUV Acoustic Imaging Applications," *J. Electroceramics*, vol. 8, no. 2, pp. 145–154, 2002.

[48] R. E. Newnham, D. P. Skinner, and L. E. Cross, "Connectivity and piezoelectric-pyroelectric composites," *Materials Research Bulletin*, vol. 13, no. 5. pp. 525–536, 1978.

[49] R. Y. Ting, "A review on the development of piezoelectric composites for underwater acoustic transducer applications," in *IEEE Instrumentation and Measurement Technology Conference*, 1991, pp. 410–413.

[50] C. S. Desilets, J. D. Fraser, and G. S. Kino, "The design of efficient broad-band piezoelectric transducers," *IEEE Trans. Sonics Ultrason.*, vol. 25, no. 3, pp. 115–125, 1978.

[51] D. M. Mills and S. W. Smith, "Finite element analysis of multi-layer composite hybrid and single crystal medical ultrasound transducers," in *IEEE Ultrasonics*

Symposium, 1999, vol. 2, pp. 1195–1198.

[52] G. Kossoff, "The Effects of Backing and Matching on the Performance of Piezoelectric Ceramic Transducers," *IEEE Trans. Sonics Ultrason.*, vol. 13, no. 1, pp. 20–30, Mar. 1966.

[53] S. N. Ramadas, R. L. O'Leary, A. Gachagan, G. Hayward, and R. Banks, "A wideband annular piezoelectric composite transducer configuration with a graded active layer profile," *IEEE Ultrason. Symp.*, pp. 2742–2745, 2009.

[54] David D. N. Hall, "The modelling and design of two-dimensional composite matrix arrays for underwater imaging applications," PhD Thesis, University of Strathclyde, 1994.

[55] S. Sherrit, H. D. Wiederick, B. K. Mukherjee, and M. Sayer, "An accurate equivalent circuit for the unloaded piezoelectric vibrator in the thickness mode," *J. Phys. D. Appl. Phys.*, vol. 30, no. 16, pp. 2354–2363, 1997.

[56] M. Garcia-Rodriguez, J. Garcia-Alvarez, Y. Yañez, M. J. Garcia-Hernandez, J. Salazar, A. Turo, and J. A. Chavez, "Low cost matching network for ultrasonic transducers," *Phys. Procedia*, vol. 3, no. 1, pp. 1025–1031, 2010.

[57] W. A. Smith and B. A. Auld, "Modeling 1-3 composite piezoelectrics: thickness-mode oscillations," *IEEE Trans. Ultrason. Ferroelectr. Freq. Control*, vol. 38, no. 1, pp. 40–47, Jan. 1991.

[58] G. Hayward, "A theoretical study on the influence of some constituent material properties on the behavior of 1-3 connectivity composite transducers," *J. Acoust. Soc. Am.*, vol. 98, no. 4, p. 2187, 1995.

[59] P. Reynolds, J. Hyslop, and G. Hayward, "Analysis of spurious resonances in single and multi-elfment piezocomposite ultrasonic transducers," *IEEE Symp. Ultrason.*, vol. 2, pp. 1650–1653, 2003.

[60] H. C. Yang, J. Cannata, J. Williams, and K. Shung, "Crosstalk reduction for high-frequency linear-array ultrasound transducers using 1-3 piezocomposites with pseudo-random pillars," *IEEE Trans. Ultrason. Ferroelectr. Freq. Control*, vol. 59, no. 10, pp. 2312–2321, 2012.

[61] W. A. Smith, A. Shaulov, and B. a. Auld, "Tailoring the Properties of Composite Piezoelectric Materials for Medical Ultrasonic Transducers," *IEEE Ultrason. Symp.*, pp. 642–647, 1985.

[62] F. Craciun, L. Sorba, E. Molinari, and M. Pappalardo, "Coupled-mode theory for periodic piezoelectric composites," *IEEE Trans. Ultrason. Ferroelectr. Freq. Control*, vol. 36, no. 1, pp. 50–56, 1989.

[63] J. A. Hossack and G. Hayward, "Finite-element analysis of 1-3 composite

transducers," *IEEE Trans. Ultrason. Ferroelectr. Freq. Control*, vol. 38, no. 6, pp. 618–629, 1991.

[64] J. A. Brown, E. Chérin, J. Yin, and F. Stuart Foster, "Fabrication and performance of high-frequency composite transducers with triangular-pillar geometry," *IEEE Trans. Ultrason. Ferroelectr. Freq. Control*, vol. 56, no. 4, pp. 827–836, 2009.

[65] H. P. Savakus, K. A. Klicker, and R. E. Newnham, "PZT-epoxy piezoelectric transducers: A simplified fabrication procedure," *Mater. Res. Bull.*, vol. 16, no. 6, pp. 677–680, Jun. 1981.

[66] A. McNab and M. J. Campbell, "Ultrasonic phased arrays for nondestructive testing," *NDT Int.*, vol. 20, no. 6, pp. 333–337, 1987.

[67] O. T. Von Ramm and S. W. Smith, "Beam Steering with Linear Arrays," *IEEE Trans. Biomed. Eng.*, vol. BME-30, no. 8, pp. 438–452, 1983.

[68] L. Zhang, X. Xu, C. Hu, L. Sun, J. T. Yen, J. M. Cannata, and K. K. Shung, "A high-frequency, high frame rate duplex ultrasound linear array imaging system for small animal imaging," *Ultrason. Ferroelectr. Freq. Control. IEEE Trans.*, vol. 57, no. 7, pp. 1548–1557, 2010.

[69] E. B. Hutchinson, "Intracavitary ultrasound phased arrays for noninvasive prostate surgery," *IEEE Trans. Ultrason. Ferroelectr. Freq. Control*, vol. 43, no. 6, pp. 1032–1042, 1996.

[70] S. Mahaut, O. Roy, C. Beroni, and B. Rotter, "Development of phased array techniques to improve characterisation of defect located in a component of complex geometry," *Ultrasonics*, vol. 40, no. 1–8, pp. 165–169, 2002.

[71] M. Li and G. Hayward, "Ultrasound nondestructive evaluation (NDE) imaging with transducer arrays and adaptive processing," *Sensors*, vol. 12, no. 1, pp. 42–54, 2012.

[72] T. R. Gururaja and R. K. Panda, "Current status and future trends in ultrasonic transducers for medical imaging applications," *IEEE Int. Symp. Appl. Ferroelectr.*, pp. 223–228, 1998.

[73] S. I. Nikolov and J. A. Jensen, "Application of different spatial sampling patterns for sparse array transducer design," *Ultrasonics*, vol. 37, no. 10, pp. 667–671, 2000.

[74] P. Y. Barthez, R. Léveillé, and P. V Scrivani, "Side lobes and grating lobes artifacts in ultrasound imaging," *Vet. Radiol. Ultrasound*, vol. 38, no. 5, pp. 387–93, 1996.

[75] D. G. Wildes, R. Y. Chiao, C. M. W. Daft, K. W. Rigby, L. S. Smith, and K. E. Thomenius, "Elevation performance of 1.25D and 1.5D transducer arrays," *IEEE Trans. Ultrason. Ferroelectr. Freq. Control*, vol. 44, no. 5, pp. 1027–1037, Sep. 1997.

[76] B. W. Drinkwater and P. D. Wilcox, “Ultrasonic arrays for non-destructive evaluation: A review,” *NDT E Int.*, vol. 39, no. 7, pp. 525–541, 2006.

[77] R. Y. Chiao and L. J. Thomas, “Analytic Evaluation of Sampled Aperture Ultrasonic Imaging Techniques for NDE,” *IEEE Trans. Ultrason. Ferroelectr. Freq. Control*, vol. 41, no. 4, pp. 484–493, 1994.

[78] J. A. Hossack, B. A. Auld, and H. D. Batha, “Techniques for suppressing spurious resonant modes in 1:3 composite transducers,” *IEEE 1991 Ultrason. Symp.*, pp. 651–656, 1991.

[79] J. R. Yuan, P. Marsh, K. Liang, and H. Kunkel, “The dynamic characteristics of composites with periodic and randomstructure,” *1996 IEEE Ultrason. Symp. Proc.*, vol. 2, pp. 949–954, 1996.

[80] G. Harvey, A. Gachagan, J. W. Mackersie, and R. Banks, “Exploring the advantages of a random 1-3 connectivity piezocomposite structure incorporating piezoelectric fibres as the active element,” *IEEE Ultrason. Symp.*, vol. 1, pp. 1903–1906, 2006.

[81] G. Harvey, A. Gachagan, J. W. MacKersie, T. McCunnie, and R. Banks, “Flexible Ultrasonic Transducers Incorporating Piezoelectric Fibres,” *IEEE Trans. Ultrason. Ferroelectr. Freq. Control*, vol. 56, no. 9, pp. 1999–2009, 2009.

[82] H. C. Yang, J. Cannata, J. Williams, and K. K. Shung, “A study of 1-3 pseudo-random pillar piezocomposites for ultrasound transducers,” *IEEE Ultrason. Symp.*, pp. 1743–1746, 2011.

[83] J. Yin, M. Lee, J. Brown, E. Cherin, and F. S. Foster, “Effect of triangular pillar geometry on high-frequency piezocomposite transducers,” *IEEE Trans. Ultrason. Ferroelectr. Freq. Control*, vol. 57, no. 4, pp. 957–968, 2010.

[84] R. Hamilton and G. Hayward, “The design of low volume fraction 1-3 connectivity composite transducers using finite element modelling techniques,” *IEEE Ultrason. Symp.*, pp. 531–534, 1992.

[85] R. Banks, R. L. O’Leary, and G. Hayward, “Enhancing the bandwidth of piezoelectric composite transducers for air-coupled non-destructive evaluation,” *Ultrasonics*, vol. 75, pp. 132–144, 2017.

[86] F. M. De Espinosa, O. Martíez, L. E. Segura, and L. Gómez-Ullate, “Double frequency piezoelectric transducer design for harmonic imaging purposes in NDT,” *IEEE Trans. Ultrason. Ferroelectr. Freq. Control*, vol. 52, no. 6, pp. 980–986, 2005.

[87] K. Yamada, D. Yamazaki, and K. Nakamura, “Broadband ultrasound transducers using a plate with a graded piezoelectric constant formed by an internal temperature gradient,” *IEEE Ultrason. Symp.*, pp. 1017–1020, 2000.

[88] K. Yamada, J. I. Sakamura, and K. Nakamura, “Broadband transducers using effectively graded piezoelectric plates for generation of short-pulse ultrasound,” *Japanese J. Appl. Physics, Part 1 Regul. Pap. Short Notes Rev. Pap.*, vol. 38, no. 5 B, pp. 3204–3207, 1999.

[89] Hongkai Guo, J. M. Cannata, Qifa Zhou, and K. K. Shung, “Fabrication and modeling of broadband ultrasonic transducers using partial composites,” in *IEEE Ultrasonics Symposium*, 2004, vol. 3, pp. 1674–1677.

[90] H. Guo, J. M. Cannata, Q. Zhou, and K. K. Shung, “Design and fabrication of broadband graded ultrasonic transducers with rectangular kerfs,” *IEEE Trans. Ultrason. Ferroelectr. Freq. Control*, vol. 52, no. 11, pp. 2096–2102, 2005.

[91] K. C. Cheng, H. L. W. Chan, C. L. Choy, Q. Yin, H. Luo, and Z. Yin, “Single crystal PMN-0.33PT/epoxy 1-3 composites for ultrasonic transducer applications,” *IEEE Trans. Ultrason. Ferroelectr. Freq. Control*, vol. 50, no. 9, pp. 1177–1183, 2003.

[92] T. Ritter, X. Geng, K. K. Shung, P. D. Lopath, S. Park, T. R. Shrout, and A. Single, “Single Crystal PZN / PT-Polymer Composites for Ultrasound Transducer Applications,” vol. 47, no. 4, pp. 792–800, 2000.

[93] C. M. Wong, Y. Chen, H. Luo, J. Dai, K. H. Lam, and H. L. wa Chan, “Development of a 20-MHz wide-bandwidth PMN-PT single crystal phased-array ultrasound transducer,” *Ultrasonics*, vol. 73, pp. 181–186, 2017.

[94] Z. Qiu, Y. Qiu, C. E. M. Demore, and S. Cochran, “Implementation of a PMN-PT Piezocrystal-based Focused Array with Geodesic Faceted Structure,” *Ultrasonics*, vol. 69, pp. 137–143, 2016.

[95] S. Li, W. Huang, X. Jiang, X. Jian, and Y. Cui, “A dual-layer micromachined PMN-PT 1-3 composite transducer for broadband ultrasound imaging,” *IEEE Ultrason. Symp.*, pp. 781–784, 2013.

[96] S. Li, X. Jiang, J. Tian, and P. Han, “Development of dual-layer micromachined composite transducers for broadband ultrasound imaging,” *IEEE Ultrason. Symp.*, pp. 667–670, 2014.

[97] J. A. Hossack and B. A. Auld, “Multiple layer transducers for broadband applications,” in *IEEE Ultrasonics Symposium*, 1991, pp. 605–610.

[98] J. Dziewierz and A. Gachagan, “Enhancing 2D phased array sensitivity and bandwidth using in-probe electronics,” *IEEE Ultrason. Symp.*, pp. 2400–2403, 2012.

[99] B. Mandelbrot, *The fractal geometry of nature*. San Francisco: W. H. Freeman and Co., 1977.

[100] L. Debnath, “A brief historical introduction to fractals and fractal geometry,” *Int. J. Math. Educ. Sci. Technol.*, vol. 37, no. 1, pp. 29–50, 2006.

[101] K. M. Iftekharuddin, W. Jia, and R. Marsh, “Fractal analysis of tumor in brain MR images,” *Mach. Vis. Appl.*, vol. 13, no. 5–6, pp. 352–362, 2003.

[102] K. M. Iftekharuddin, J. Zheng, M. A. Islam, and R. J. Ogg, “Fractal-based brain tumor detection in multimodal MRI,” *Appl. Math. Comput.*, vol. 207, no. 1, pp. 23–41, 2009.

[103] N. Azzaz, “Classification of radar echoes using fractal geometry,” *Chaos, Solitons and Fractals*, vol. 98, pp. 130–144, 2017.

[104] C. Puente-Baliarda and R. Pous, “Fractal design of multiband and low side-lobe arrays,” *IEEE Trans. Antennas Propag.*, vol. 44, no. 5, pp. 730–739, 1996.

[105] D. L. Jaggard and A. D. Jaggard, “Fractal ring arrays,” *Wave Motion*, vol. 34, no. 3, pp. 281–299, 2001.

[106] I. Rian, M. Sassone, and S. Asayama, “From fractal geometry to architecture : Designing a grid-shell-like structure using the Takagi – Landsberg surface,” *Comput. Des.*, vol. 100, p. 68, 2018.

[107] I. M. Rian and S. Asayama, “Computational Design of a nature-inspired architectural structure using the concepts of self-similar and random fractals,” *Autom. Constr.*, vol. 66, pp. 43–58, 2016.

[108] S. K. Chen, T. Oviir, C. H. Lin, L. J. Leu, B. H. Cho, and L. Hollender, “Digital imaging analysis with mathematical morphology and fractal dimension for evaluation of periapical lesions following endodontic treatment,” *Oral Surgery, Oral Med. Oral Pathol. Oral Radiol. Endodontology*, vol. 100, no. 4, pp. 467–472, 2005.

[109] A. Biswas, S. Karmakar, S. Sharma, and M. Kumar, “Performance of Fractal Image Compression for Medical Images: A Comprehensive Literature Review,” *Researchgate.Net*, vol. 8, no. 4, pp. 14–24, 2015.

[110] A. Alippi, A. Bettucci, F. Craciun, F. Farrelly, E. Molinari, and A. Petri, “Acoustic modes in 2-dimensional self-similar composite plates,” *IEEE Ultrason. Symp.*, pp. 533–536, 1993.

[111] A. J. Mulholland, J. W. Mackersie, R. L. O’Leary, A. Gachagan, A. J. Walker, and N. Ramadas, “The use of fractal geometry in the design of piezoelectric ultrasonic transducers,” in *IEEE Ultrasonics Symposium*, 2011, pp. 1559–1562.

[112] E. A. Algehyne and A. J. Mulholland, “Renormalization analysis of a composite ultrasonic transducer with a fractal architecture,” *Fractals*, vol. 25, no. 02, p. 1750015, Apr. 2017.

[113] S. Canning, A. J. Walker, and P. A. Roach, “The Effectiveness of a Sierpinski Carpet-Inspired Transucer,” *Fractals*, vol. 25, no. 5, pp. 1–15, 2017.

[114] G. Chen, W. Zhang, and W. Pang, “Koch curve fractal geometry excitation probe for eddy current non-destructive testing,” *Meas. J. Int. Meas. Confed.*, vol. 124, no. April, pp. 470–478, 2018.

[115] H. Fang, Z. Qiu, R. L. O’Leary, A. Gachagan, and A. J. Mulholland, “Improving the operational bandwidth of a 1–3 piezoelectric composite transducer using Sierpinski Gasket fractal geometry,” in *2016 IEEE International Ultrasonics Symposium*, 2016, pp. 1–4.

[116] H. Fang, Z. Qiu, A. J. Mulholland, R. L. O’Leary, and A. Gachagan, “Broadband 1–3 Piezoelectric Composite Transducer Design Using Sierpinski Gasket Fractal Geometry,” *IEEE Trans. Ultrason. Ferroelectr. Freq. Control*, vol. 65, no. 12, pp. 2429–2439, Dec. 2018.

[117] G. Hayward and J. Bennett, “Assessing the influence of pillar aspect ratio on the behavior of 1-3 connectivity composite transducers,” *IEEE Trans. Ultrason. Ferroelectr. Freq. Control*, vol. 43, no. 1, pp. 98–108, 1996.

[118] Q. Zhou, K. Ho, H. Zheng, W. Qiu, and K. K. Shung, “Piezoelectric single crystal ultrasonic transducers for biomedical applications,” *J. Prog. Mater. Sci.*, vol. 66, pp. 87–111, 2014.

[119] R. L. O ’Leary, G. Hayward, G. Smillie, and A. C. S. Parr, “CUE Materials Database,” Version 1., 2005.

[120] D. Callens, C. Bruneel, and J. Assaad, “Matching ultrasonic transducer using two matching layers where one of them is glue,” *NDT E Int.*, vol. 37, no. 8, pp. 591–596, 2004.

[121] W. Galbraith, “The Development of a PVDF Membrane Hydrophone for Use in Air Coupled Transducer Calibration,” PhD Thesis, University of Strathclyde, 1997.

[122] H. Fang, Z. Qiu, R. L. O’Leary, A. Gachagan, and A. J. Mulholland, “Linear ultrasonic array incorporating a Cantor Set fractal element configuration,” in *2017 IEEE International Ultrasonics Symposium (IUS)*, 2017, pp. 1–4.

[123] H. Fang, Z. Qiu, R. L. O’Leary, A. Gachagan, and A. J. Mulholland, “Linear Ultrasonic Array Development Incorporating Cantor Set Fractal Geometry,” in *2018 IEEE International Ultrasonics Symposium*, 2018, pp. 1–4.

[124] G. Hayward and J. Hyslop, “Determination of Lamb wave dispersion data in lossy anisotropic plates using time domain finite element analysis. Part II: Application to 2-2 and 1-3 piezoelectric composite transducer arrays,” *IEEE Trans. Ultrason. Ferroelectr. Freq. Control*, vol. 53, no. 2, pp. 449–455, 2006.

[125] J. Dziewierz, S. N. Ramadas, A. Gachagan, R. L. O'Leary, and G. Hayward, "A 2D ultrasonic array design incorporating hexagonal-shaped elements and triangular-cut piezocomposite substructure for NDE applications," *IEEE Ultrason. Symp.*, vol. 3, pp. 422–425, 2009.

Appendices

Appendix A: Constitutive Equations for Piezoelectric Effect

In Chapter II, Section 2.1.1, the direct and converse of piezoelectric effect is defined by Equations (2-1) and (2-2). Another three alternative equation pairs are given below which is also used frequently for describing the direct and converse of piezoelectric effect.

$$D = \varepsilon^S E + eS \text{ and } T = c^E S - eE$$

$$E = -gT + \frac{D}{\varepsilon^T} \text{ and } S = s^D T + gD$$

$$E = -hS + \frac{D}{\varepsilon^S} \text{ and } T = c^D S - hD$$

** The definition of each character can be found in the symbol definition table at the beginning of this thesis on Page xviii.*

Appendix B: The Derivative of the Mathematical Equations for CS Fractal Geometry Definition

The CS fractal geometry from generation Level 0 to III is shown in the figure below.

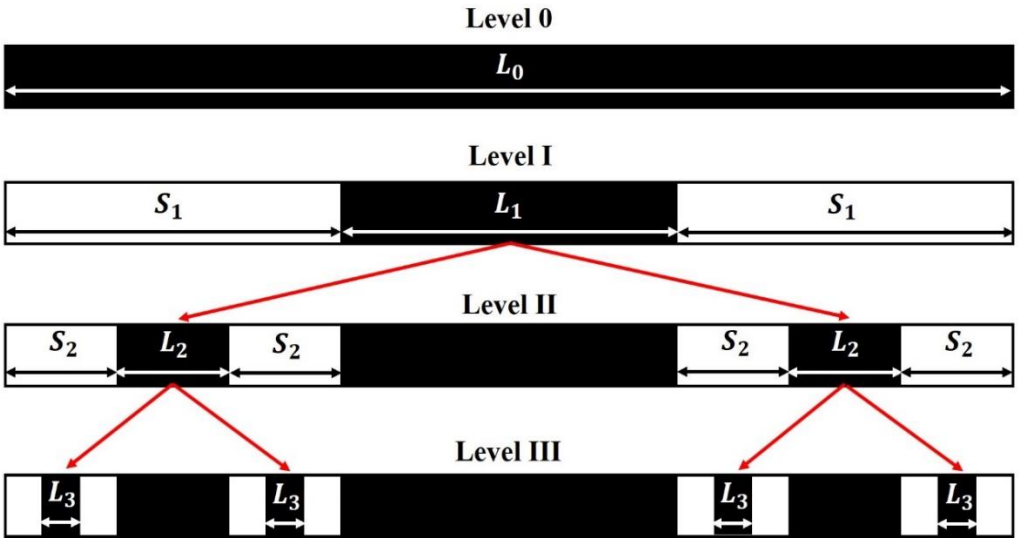

In Level I,

$$L_1 = \frac{L_0}{m}$$

$$S_1 = L_0 \cdot (\frac{m-1}{m} \cdot \frac{1}{2})$$

where $m < 1$.

In Level II,

$$L_2 = \frac{S_1}{m} = L_0 \cdot (\frac{m-1}{m} \cdot \frac{1}{2}) \cdot \frac{1}{m}$$

$$S_2 = S_1 \cdot \frac{m-1}{m} \cdot \frac{1}{2} = L_0 \cdot \left(\frac{m-1}{m} \cdot \frac{1}{2}\right) \cdot \left(\frac{m-1}{m} \cdot \frac{1}{2}\right)$$

$$= L_0 \cdot (\frac{m-1}{m} \cdot \frac{1}{2})^2$$

In Level III,

$$L_3 = \frac{S_2}{m} = L_0 \cdot \left(\frac{m-1}{m} \cdot \frac{1}{2}\right) \cdot \left(\frac{m-1}{m} \cdot \frac{1}{2}\right) \cdot \frac{1}{m}$$

$$= L_0 \cdot \left(\frac{m-1}{m} \cdot \frac{1}{2}\right)^2 \cdot \frac{1}{m}$$

$$S_3 = S_2 \cdot \frac{m-1}{m} \cdot \frac{1}{2} = L_0 \cdot \left(\frac{m-1}{m} \cdot \frac{1}{2}\right) \cdot \left(\frac{m-1}{m} \cdot \frac{1}{2}\right) \cdot \left(\frac{m-1}{m} \cdot \frac{1}{2}\right)$$

$$= L_0 \cdot \left(\frac{m-1}{m} \cdot \frac{1}{2}\right)^3$$

At Level N,

$$L_n = L_0 \cdot \left(\frac{m-1}{m} \cdot \frac{1}{2}\right)^{n-1} \cdot \frac{1}{m}$$

$$S_n = L_0 \cdot \left(\frac{m-1}{m} \cdot \frac{1}{2}\right)^n$$

As the result, by taking $\left(\frac{m-1}{m} \cdot \frac{1}{2}\right) = k, \left(0 < k < \frac{1}{2}\right)$, the following equations can be achieved:

$$L_n = L_0 \cdot k^{n-1} \cdot \frac{1}{m}$$

$$S_n = L_0 \cdot k^n$$

$$L_n = L_{n-1} \cdot k^n$$

Appendix C: Flexible Printed Circuit Board Design

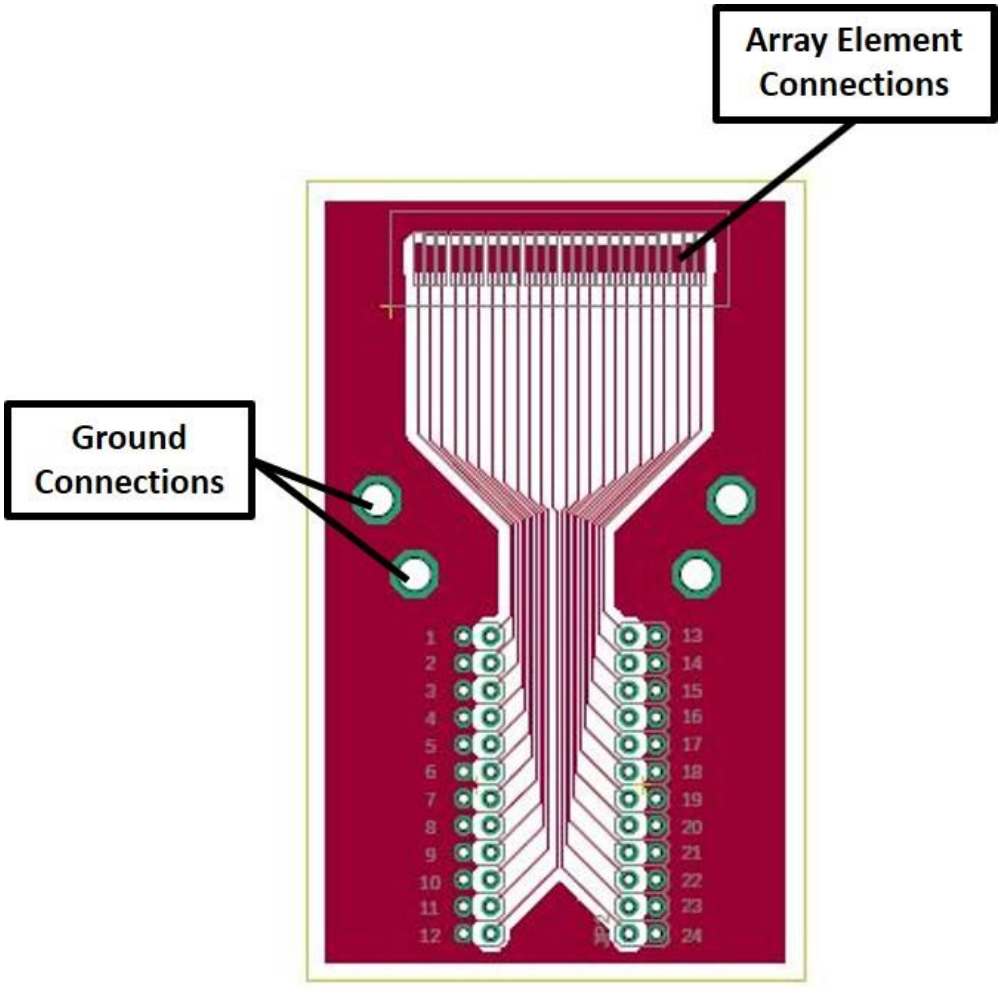

Appendix D: Full elasto-electric matrix for PZT-5H ceramic

PZT-5H Ceramic					
General properties, density, ρ (kg/m^3) and longitudinal velocity, V_l (m/s)					
$\boldsymbol{\rho}$			$\boldsymbol{V_l}$		
7450			4200		
Elastic compliance constant, s $(10^{-12}m^2/N)$; Elastic stiffness constant c $(10^{10}N/m^2)$					
$\boldsymbol{s_{11}^E}$	$\boldsymbol{s_{12}^E}$	$\boldsymbol{s_{13}^E}$	$\boldsymbol{s_{33}^E}$	$\boldsymbol{s_{55}^E}$	$\boldsymbol{s_{66}^E}$
17.00	-57.80	-8.79	22.90	54.10	45.60
$\boldsymbol{s_{11}^D}$	$\boldsymbol{s_{12}^D}$	$\boldsymbol{s_{13}^D}$	$\boldsymbol{s_{33}^D}$	$\boldsymbol{s_{55}^D}$	$\boldsymbol{s_{66}^D}$
14.70	-8.10	-3.30	9.94	29.80	45.60
$\boldsymbol{c_{11}^E}$	$\boldsymbol{c_{12}^E}$	$\boldsymbol{c_{13}^E}$	$\boldsymbol{c_{33}^E}$	$\boldsymbol{c_{55}^E}$	$\boldsymbol{c_{66}^E}$
13.40	8.97	8.57	10.90	1.85	2.20
$\boldsymbol{c_{11}^D}$	$\boldsymbol{c_{12}^D}$	$\boldsymbol{c_{13}^D}$	$\boldsymbol{c_{33}^D}$	$\boldsymbol{c_{55}^D}$	$\boldsymbol{c_{66}^D}$
13.60	9.21	7.58	15.10	3.36	2.20
Piezoelectric charge constant, d $(10^{-10}\mathrm{C/N})$; Piezoelectric stress constant, e (C/m^2); Piezoelectric voltage constant, g $(10^{-3}\mathrm{Vm/N})$; Piezoelectric stiffness constant, h $(10^8 V/\mathrm{m})$					
$\boldsymbol{d_{15}}$	$\boldsymbol{d_{31}}$	$\boldsymbol{d_{33}}$	$\boldsymbol{e_{15}}$	$\boldsymbol{e_{31}}$	$\boldsymbol{e_{33}}$
7.24	-2.43	5.74	13.40	-5.06	21.20
$\boldsymbol{g_{15}}$	$\boldsymbol{g_{31}}$	$\boldsymbol{g_{33}}$	$\boldsymbol{h_{15}}$	$\boldsymbol{h_{31}}$	$\boldsymbol{h_{33}}$
32.10	-9.60	22.60	11.30	-4.68	19.60
Electromechanical coupling coefficients, k; Relative permittivity, ε_r * The permittivity in the vacuum is $\varepsilon_0 = 8.854\ pF/m$					
$\boldsymbol{k_t}$	$\boldsymbol{k_{15}}$	$\boldsymbol{k_{31}}$	$\boldsymbol{k_{33}}$		
0.524	0.671	0.37	0.752		
$\boldsymbol{\varepsilon_{r11}^T}$	$\boldsymbol{\varepsilon_{r33}^T}$	$\boldsymbol{\varepsilon_{r11}^S}$	$\boldsymbol{\varepsilon_{r33}^S}$		
2440	2870	1340	1220		

Appendix E: Passive Material Properties Database

Hard Set (RX771C(NC)/CY1300) (11.015mm) **Medium: Water**			
Frequency (MHz)	0.5	1.0	2.25
V_l (m/s)	2512.7	2535.9	2560
V_s (m/s)	1175	1178.8	1208.7
Density (kg/m^3)	1149	1149	1149
Poisson Ratio	0.3601	0.3622	0.3566
Impedance Z ($MRayl$)	2.86	2.89	2.92
Young's Modulus E_y (N/m^2)	4.2810E+09	4.3157E+09	4.5187E+09
Bulk Modulus B (N/m^2)	5.0990E+09	5.2190E+09	5.2505E+09
Shear Modulus G (N/m^2)	1.5739E+09	1.5841E+09	1.6655E+09
c_{11}	7.1976E+09	7.3311E+09	7.4711E+09
c_{44}	1.5739E+09	1.5841E+09	1.6655E+09
s_{11}	2.3360E-10	2.3170E-10	2.2130E-10
s_{44}	6.3540E-10	6.3130E-10	6.0040E-10
Longitudinal Attenuation (dB/m)	139	287	608
Shear Attenuation (dB/m)	356	738	1980

Medium Set (CY221/HY956EN) (3.103mm) **Medium: Water**			
Frequency (MHz)	0.5	1.0	2.25
V_l (m/s)	2364.1	2451.5	2440.9
V_s (m/s)	1064.6	1109.9	1084.5
Density (kg/m^3)	1134	1134	1134
Poisson Ratio	0.3728	0.3711	0.377
Impedance Z ($MRayl$)	2.68	2.78	2.77
Young's Modulus E_y (N/m^2)	3.5288E+09	3.8307E+09	3.6732E+09
Bulk Modulus B (N/m^2)	4.6242E+09	4.9526E+09	4.9780E+09
Shear Modulus G (N/m^2)	1.2852E+09	1.3969E+09	1.3337E+09
c_{11}	6.3379E+09	6.8152E+09	6.7564E+09
c_{44}	1.2852E+09	1.3969E+09	1.3337E+09
s_{11}	2.8340E-10	2.6110E-10	2.7220E-10
s_{44}	7.7810E-10	7.1580E-10	7.4980E-10
Longitudinal Attenuation (dB/m)	208	895	1711
Shear Attenuation (dB/m)	2319	4108	8147

Calcined Alumina 70% by wgt with Hard Set (RX771C(NC)/CY1300) 13.133mm **Medium: Water**			
Frequency (MHz)	0.5	1.0	2.25
V_l (m/s)	3014.6	2999	2921.7
V_s (m/s)	1684.1	1686.1	1662.6
Density (kg/m^3)	2308	2308	2308
Poisson Ratio	0.2732	0.2689	0.2606
Impedance Z ($MRayl$)	6.96	6.92	6.74
Young's Modulus E_y (N/m^2)	1.6668E+10	1.6652E+10	1.6084E+10
Bulk Modulus B (N/m^2)	1.2247E+10	1.2010E+10	1.1195E+10
Shear Modulus G (N/m^2)	6.5459E+09	6.5615E+09	6.3799E+09
c_{11}	2.0975E+10	2.0758E+10	1.9702E+10
c_{44}	6.5460E+09	6.5610E+09	6.3800E+09
s_{11}	6.0000E-11	6.0100E-11	6.7200E-11
s_{44}	1.5280E-10	1.5240E-10	1.5670E-10
Longitudinal Attenuation (dB/m)	182	321	678
Shear Attenuation (dB/m)	-	556	1364

Calcined Alumina 50% by wgt with Hard Set (RX771C(NC)/CY1300) (9.13mm) **Medium: Water**			
Frequency (MHz)	0.5	1.0	2.25
V_l (m/s)	2695.9	2667.4	2633.5
V_s (m/s)	1362.2	1376.4	1367.1
Density (kg/m^3)	1758	1758	1758
Poisson Ratio	0.3286	0.3186	0.3156
Impedance Z ($MRayl$)	4.74	4.69	4.63
Young's Modulus E_y (N/m^2)	8.6680E+09	8.7829E+09	8.6448E+09
Bulk Modulus B (N/m^2)	8.4274E+09	8.0676E+09	7.8114E+09
Shear Modulus G (N/m^2)	3.2621E+09	3.3305E+09	3.2856E+09
c_{11}	1.2777E+10	1.2508E+10	1.2192E+10
c_{44}	3.2620E+09	3.3300E+09	3.2860E+09
s_{11}	1.1540E-10	1.1390E-10	1.1570E-10
s_{44}	3.0650E-10	3.0030E-10	3.0440E-10
Longitudinal Attenuation (dB/m)	156	330	625
Shear Attenuation (dB/m)	339	773	1720

Tungsten 24% by wgt with Hard Set (RX771C(NC)/CY1300) **Medium: Water**	
Frequency (MHz)	1.0
V_l (m/s)	1579.7
V_s (m/s)	830.9
Density (kg/m^3)	5454
Poisson Ratio	0.3088
Impedance, Z ($MRayl$)	8.62
Young's Modulus, E_y (N/m^2)	9.8560E+09
Bulk Modulus, B (N/m^2)	8.5900E+09
Shear Modulus, G (N/m^2)	3.7650E+09
c_{11}	1.3610E+10
c_{44}	3.7650E+09
s_{11}	1.0150E-10
s_{44}	2.6560E-10
Longitudinal Attenuation (dB/m)	473
Shear Attenuation (dB/m)	938